

# **GEO FEM - Theoretical manual**

written by

**Michal Šejnoha**

*A computer program*

*for nonlinear finite element analysis of geotechnical problems*

FINE Ltd. 1999–2009

February 9, 2009

# Contents

<b>1</b>	<b>Finite Element Equations</b>	<b>1</b>
1.1	Kinematics discretization . . . . .	2
1.2	Governing equations . . . . .	3
1.3	Finite elements used in GEO FEM program . . . . .	4
1.3.1	2-node rod element . . . . .	4
1.3.2	2-node and 3-node beam elements . . . . .	6
1.3.3	Plane 3-node and 6-node triangular elements . . . . .	11
1.3.4	4-node and 6-node interface elements . . . . .	17
<b>2</b>	<b>Basic constitutive models for soils</b>	<b>22</b>
2.1	Elastic constitutive model for soils . . . . .	22
2.2	Modified elastic constitutive model for soils . . . . .	23
2.3	Basic elasto-plastic constitutive models for soils . . . . .	23
2.3.1	Invariants . . . . .	24
2.3.2	Yield surface . . . . .	25
2.3.3	Elasto-plastic stiffness matrix . . . . .	27
2.3.4	Drucker-Prager model . . . . .	30
2.3.5	Modified Mohr-Coulomb model . . . . .	36
2.3.6	Implicit stress point algorithm for DP and MMC models . . . . .	39
2.3.7	Mohr-Coulomb model . . . . .	44
2.3.8	Mohr-Coulomb model with tension cut-off . . . . .	59
2.4	Interface constitutive model . . . . .	61
2.4.1	Yield surface and stress update procedure . . . . .	61
2.4.2	Tangent stiffness matrix . . . . .	63
<b>3</b>	<b>Critical state models for soils</b>	<b>65</b>
3.1	Modified Cam clay model . . . . .	65
3.2	Generalized Cam clay model . . . . .	69
3.3	Numerical integration - stress update procedure . . . . .	70
3.3.1	Modified Cam clay model . . . . .	71
3.3.2	Generalized Cam clay model . . . . .	74
3.3.3	Note on numerical implementation . . . . .	77
3.3.4	Note on determination of parameters $\kappa$ and $\lambda$ . . . . .	78

<b>4</b>	<b>Constitutive models for structural elements</b>	<b>81</b>
4.1	Grout anchors . . . . .	82
4.2	Geo-reinforcements . . . . .	84
4.3	Props . . . . .	84
<b>5</b>	<b>Modeling of ground water flow</b>	<b>86</b>
5.1	One-phase flow in a partially saturated medium . . . . .	87
5.1.1	Constitutive equations . . . . .	88
5.1.2	Transport equation - Darcy's law . . . . .	89
5.1.3	Set of governing equations . . . . .	91
5.2	Fully undrained behavior of saturated soil . . . . .	93
5.3	Steady state seepage . . . . .	97
5.4	Flow through a thin zone - modeling of interfaces . . . . .	101
5.4.1	Thin zone interface element . . . . .	101
5.4.2	Seepage surface . . . . .	105

# Chapter 1

## Finite Element Equations

The present section provides a derivation of the governing finite element equations with respect to a given boundary value problem. Formulation of the set of elements implemented within the GEO FEM program is provided next. Throughout this section, the standard engineering notation is used (see, e.g., [2]).

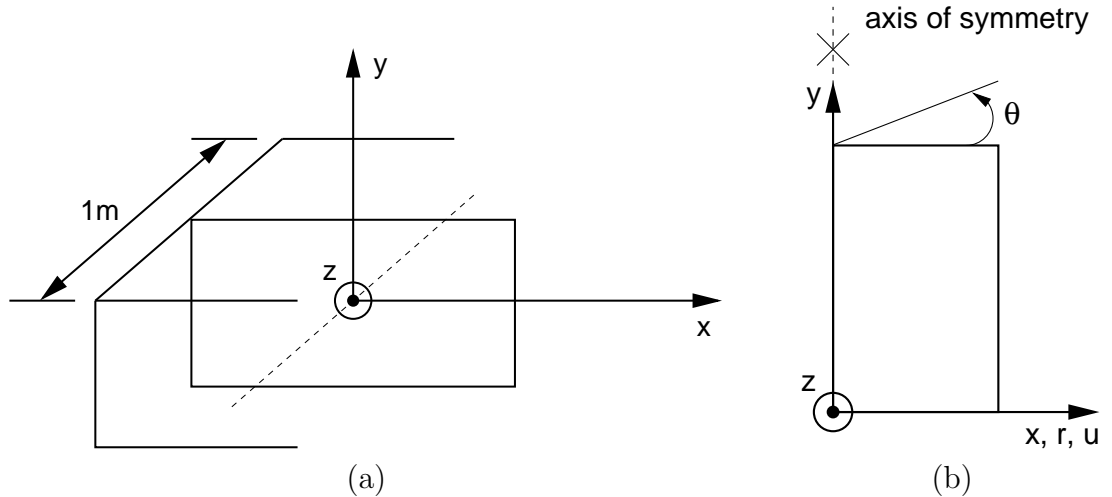


Figure 1.1: a) Plane strain analysis, b) Axisymmetric analysis

Limiting our attention to plane strain or axisymmetric analysis, see Fig. 1.1, the stress and strain tensors written in the vector form are

- Plane strain analysis

$$\boldsymbol{\sigma}^T = \{ \sigma_{xx} \quad \sigma_{yy} \quad \sigma_{xy} \quad \sigma_{zz} \}, \quad \boldsymbol{\epsilon}^T = \{ \epsilon_{xx} \quad \epsilon_{yy} \quad 2\epsilon_{xy} \quad \epsilon_{zz} \}, \quad (1.1)$$

- Axisymmetric analysis

$$\boldsymbol{\sigma}^T = \{ \sigma_{rr} \quad \sigma_{yy} \quad \sigma_{ry} \quad \sigma_{\theta\theta} \}, \quad \boldsymbol{\epsilon}^T = \left\{ \epsilon_{rr} \quad \epsilon_{yy} \quad 2\epsilon_{ry} \quad \epsilon_{\theta\theta} = \frac{u}{r} \right\}, \quad (1.2)$$

where  $\theta$  represents the circumferential (hoop) direction,  $u$  is the radial displacement and  $r$  is the current radius. We further introduce the  $(3 \times 4)$  matrix  $\boldsymbol{\partial}$  defined as

$$\boldsymbol{\partial} = \begin{bmatrix} \frac{\partial}{\partial x} & 0 & \frac{\partial}{\partial y} & 0 \\ 0 & \frac{\partial}{\partial y} & \frac{\partial}{\partial x} & 0 \\ 0 & 0 & 0 & \frac{\partial}{\partial z} \end{bmatrix}, \quad (1.3)$$

and the  $(3 \times 4)$  matrix  $\mathbf{n}$  that stores the components of the unit normal vector,

$$\mathbf{n} = \begin{bmatrix} n_x & 0 & n_y & 0 \\ 0 & n_y & n_x & 0 \\ 0 & 0 & 0 & n_z \end{bmatrix}. \quad (1.4)$$

## 1.1 Kinematics discretization

Consider a body  $\Omega$  bounded by a surface  $\Gamma$ , Fig 1.2.  $\Gamma_u$  represents a portion of  $\Gamma$  with prescribed displacements  $\bar{\mathbf{u}}$  while tractions  $\bar{\mathbf{t}}$  are prescribed on  $\Gamma_t$  ( $\Gamma_u \cap \Gamma_t = \emptyset$ ).

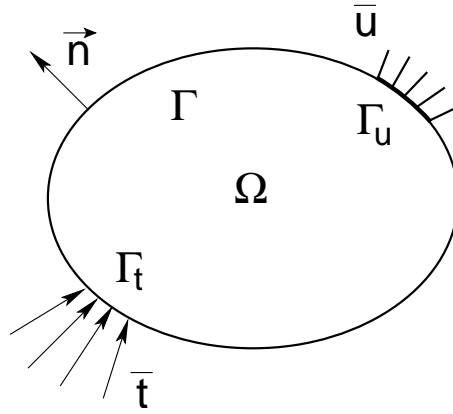


Figure 1.2: Body  $\Omega$  with boundary surface  $\Gamma$

In the standard finite element method the displacement field can be interpolated over the body  $\Omega$  using the nodal shape functions [2] in the form

$$\mathbf{u}(\mathbf{x}) = \mathbf{N}(\mathbf{x})\mathbf{a}, \quad (1.5)$$

where  $\mathbf{N}$  is a matrix of standard nodal shape functions to interpolate the nodal degrees of freedom. The introduction of Eq. (1.5) into Eq. (1.8) expresses the strain field as

$$\boldsymbol{\epsilon}(\mathbf{x}) = \mathbf{B}(\mathbf{x})\mathbf{a}, \quad (1.6)$$

where  $\mathbf{B} = \boldsymbol{\partial}^T \mathbf{N}$  is the familiar strain matrix.

## 1.2 Governing equations

Consider a linear elastic body  $\Omega$ . Assuming small strains, the linear momentum balance equation and the kinematic equations result in

$$\boldsymbol{\partial}\boldsymbol{\sigma} + \mathbf{X} = \mathbf{0}, \quad (1.7)$$

and

$$\boldsymbol{\epsilon} = \boldsymbol{\partial}^\top \mathbf{u}. \quad (1.8)$$

The vector  $\mathbf{X}$  in Eq. (1.7) represents the vector of body forces. The traction and displacement boundary conditions are given by

$$\mathbf{n}\boldsymbol{\sigma} = \bar{\mathbf{t}} \quad \text{on } \Gamma_t, \quad (1.9)$$

and

$$\mathbf{u} = \bar{\mathbf{u}} \quad \text{on } \Gamma_u. \quad (1.10)$$

The system of governing equations is usually derived by invoking the principle of virtual work. In particular, the principle of virtual displacements can be recovered by forcing the equations of equilibrium, Eq. (1.7), to be satisfied in an average sense such that

$$\int_{\Omega} \delta \mathbf{u}^\top (\boldsymbol{\partial}\boldsymbol{\sigma} + \mathbf{X}) \, d\Omega + \int_{\Gamma_t} \delta \mathbf{u}^\top (-\mathbf{n}\boldsymbol{\sigma} + \bar{\mathbf{t}}) \, d\Gamma = 0, \quad (1.11)$$

for all kinematically admissible  $\delta \mathbf{u}$ . Next, applying Green's theorem and taking into account the fact that  $\delta \mathbf{u} = \mathbf{0}$  on  $\Gamma_u$  gives

$$\int_{\Omega} \delta \boldsymbol{\epsilon}^\top \boldsymbol{\sigma} \, d\Omega = \int_{\Omega} \delta \mathbf{u}^\top \mathbf{X} \, d\Omega + \int_{\Gamma_t} \delta \mathbf{u}^\top \bar{\mathbf{t}} \, d\Gamma. \quad (1.12)$$

In the context of quasistatic non-linear finite element analysis Eq. (1.12) is usually presented in its linearized form

$$\int_{\Omega} \delta \Delta \boldsymbol{\epsilon}^\top \Delta \boldsymbol{\sigma} \, d\Omega = \int_{\Omega} \delta \Delta \mathbf{u}^\top \Delta \mathbf{X} \, d\Omega + \int_{\Gamma_t} \delta \Delta \mathbf{u}^\top \Delta \bar{\mathbf{t}} \, d\Gamma, \quad (1.13)$$

where  $\Delta$  represents an increment of a given quantity over a certain increment of time  $\Delta t$ . To proceed, we introduce with the help of Eq. (1.5) an incremental form of constitutive equations as

$$\Delta \boldsymbol{\sigma} = \mathbf{D} \Delta \boldsymbol{\epsilon} + \Delta \boldsymbol{\sigma}_{in} = \mathbf{D} \mathbf{B} \Delta \mathbf{a} + \Delta \boldsymbol{\sigma}_{in}, \quad (1.14)$$

where  $\mathbf{D}$  is the  $(4 \times 4)$  instantaneous (tangent) material stiffness matrix and  $\Delta \boldsymbol{\sigma}_{in}$  is the increment of the initial stress vector. A contribution to  $\Delta \boldsymbol{\sigma}_{in}$  can be attributed to a

number of distinct physical sources (thermal effects, pre-stress of structural elements such as anchors, pore pressure, etc.). Finally, introducing Eq. (1.14) into Eq. (1.13) yields

$$\begin{aligned} \delta \Delta \mathbf{a}^\top \int_{\Omega} \mathbf{B}^\top \mathbf{D} \mathbf{B} \Delta \mathbf{a} \, d\Omega &= \delta \Delta \mathbf{a}^\top \int_{\Omega} \mathbf{N}^\top \Delta \mathbf{X} \, d\Omega \\ &- \delta \Delta \mathbf{a}^\top \int_{\Omega} \mathbf{B}^\top \Delta \boldsymbol{\sigma}_{in} \, d\Omega + \delta \Delta \mathbf{a}^\top \int_{\Gamma_t} \mathbf{N}^\top \Delta \bar{\mathbf{t}} \, d\Gamma, \end{aligned} \quad (1.15)$$

Noting that Eq. (1.15) must be satisfied for all kinematically admissible  $\delta \Delta \mathbf{a}$  we arrive at the traditional form of the discrete system of linear equations

$$\mathbf{K} \Delta \mathbf{u} = \Delta \mathbf{f}, \quad (1.16)$$

where  $\mathbf{K}$  is the instantaneous (tangent) global stiffness matrix and  $\Delta \mathbf{f}$  represents the generalized load vector. Individual symbols in Eq. (1.16) are provided by

$$\mathbf{K} = \int_{\Omega} \mathbf{B}^\top \mathbf{D} \mathbf{B} \, d\Omega, \quad (1.17)$$

$$\Delta \mathbf{f} = \int_{\Omega} \mathbf{N}^\top \Delta \mathbf{X} \, d\Omega - \int_{\Omega} \mathbf{B}^\top \Delta \boldsymbol{\sigma}_{in} \, d\Omega + \int_{\Gamma_t} \mathbf{N}^\top \Delta \bar{\mathbf{t}} \, d\Gamma. \quad (1.18)$$

Following the standard finite element procedure, the stiffness matrix is obtained by the assembly of contributions from individual elements. To that end, the domain  $\Omega$  is decomposed into  $N_e$  non-intersecting elements  $\Omega_e$  such that  $\Omega = \cup_{e=1}^{N_e} \Omega_e$ . Formally, the global stiffness matrix and the global force vector become

$$\mathbf{K} = \mathbf{A}_{e=1}^{N_e} \mathbf{K}_e, \quad (1.19)$$

$$\Delta \mathbf{f} = \mathbf{A}_{e=1}^{N_e} \Delta \mathbf{f}_e. \quad (1.20)$$

## 1.3 Finite elements used in GEO FEM program

The following section provides a brief overview of the individual finite elements used in the GEO FEM finite element code. The available elements can be divided into two groups: two-dimensional plane strain elements (3-node and 6-node triangular elements) and special elements such as the 2-node rod element to model anchors, 2-node and 3-node beam elements to model supporting walls, tunnel linings or foundations and the 4-node and 6-node interface elements to model relative movement of the structure with respect to the soil. All elements implemented in GEO FEM are constructed within the framework of isoparametric formulation, which means that the same interpolation functions are used to approximate geometry as well as the displacement field.

### 1.3.1 2-node rod element

The 2-node rod element with the linear interpolation of the displacement field is shown in Fig. 1.3.

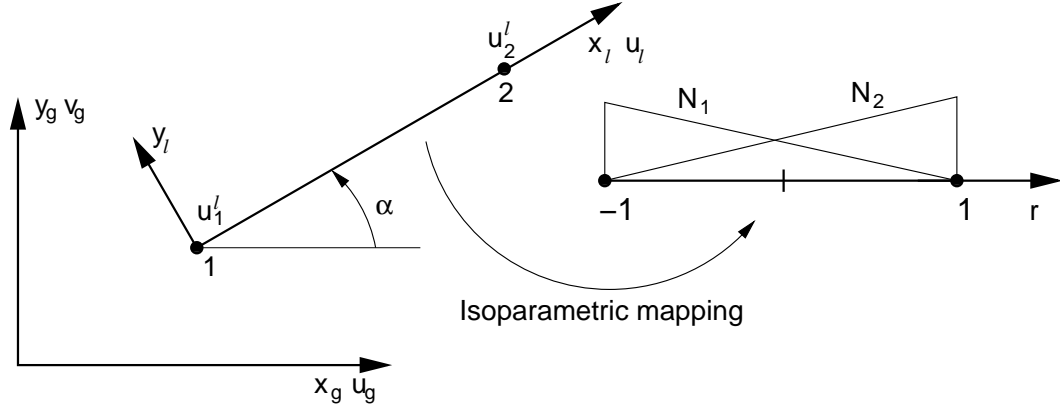


Figure 1.3: 2-node rod element

### Kinematics

The local displacement  $u_l$  written in terms of the global degrees of freedom  $\mathbf{a}_e = \{u_1, v_1, u_2, v_2\}^T$  reads

$$u_l = N_1 \underbrace{(u_1 \cos \alpha + v_1 \sin \alpha)}_{u_1^l} + N_2 \underbrace{(u_2 \cos \alpha + v_2 \sin \alpha)}_{u_2^l}, \quad (1.21)$$

where the isoparametric element shape functions  $N_1, N_2$  are given by

$$\begin{aligned} N_1 &= \frac{1}{2}(1-r), \\ N_2 &= \frac{1}{2}(1+r). \end{aligned}$$

### Element stiffness matrix

Taking the derivative of Eq. (1.21) with respect to  $x_l$  gives the axial strain in the form

$$\epsilon = \mathbf{B}\mathbf{a}, \quad (1.22)$$

where the  $(1 \times 4)$  matrix  $\mathbf{B}$  attains the following form

$$\mathbf{B} = \frac{1}{L} \{-\cos \alpha, -\sin \alpha, \cos \alpha, \sin \alpha\}. \quad (1.23)$$

where  $L$  is the element length. To conclude the derivation of the element stiffness matrix we introduce the constitutive law in the form

$$\sigma = D\epsilon = \frac{EA}{L}\epsilon, \quad (1.24)$$

where  $D = EA/L$  represent the element axial stiffness;  $E, A$  are the Young modulus and the element cross-sectional area respectively. Finally, making use of Eq. (1.17) on the



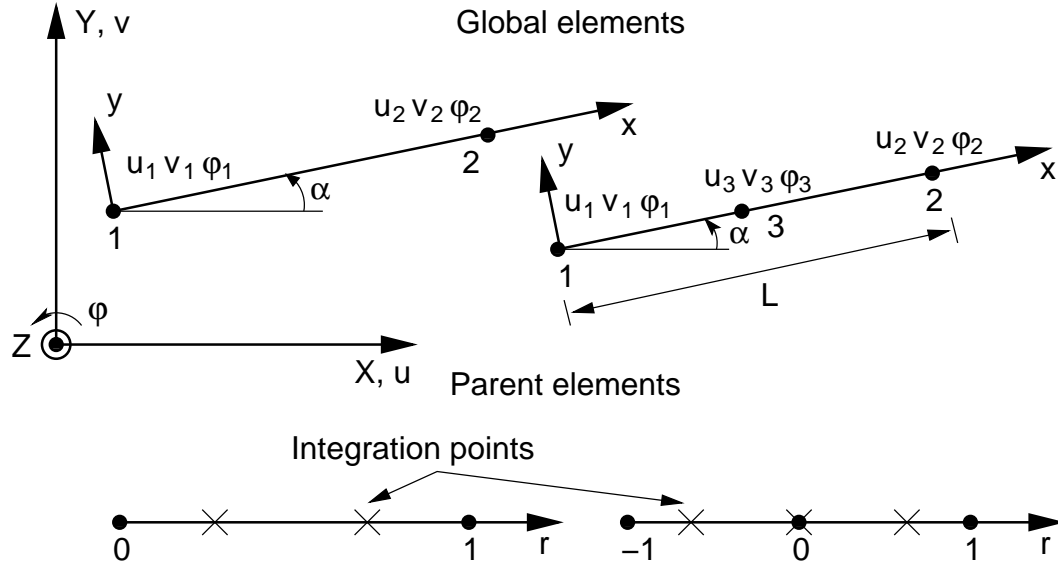


Figure 1.4: 2-node and 3-node beam elements

element level provides the element stiffness matrix  $\mathbf{K}_e$  as

$$\mathbf{K}_e = \frac{EA}{L} \begin{bmatrix} \cos \alpha \cos \alpha & \cos \alpha \sin \alpha & -\cos \alpha \cos \alpha & -\cos \alpha \sin \alpha \\ \cos \alpha \sin \alpha & \sin \alpha \sin \alpha & -\cos \alpha \sin \alpha & -\sin \alpha \sin \alpha \\ -\cos \alpha \cos \alpha & -\cos \alpha \sin \alpha & \cos \alpha \cos \alpha & \cos \alpha \sin \alpha \\ -\cos \alpha \sin \alpha & -\sin \alpha \sin \alpha & \cos \alpha \sin \alpha & \sin \alpha \sin \alpha \end{bmatrix}. \quad (1.25)$$

### 1.3.2 2-node and 3-node beam elements

The 2-node and 3-node beam elements implemented in GEO FEM appear in Fig. 1.4.

#### Kinematics

In plane strain or axisymmetric analysis the beam elements can be introduced to represent, e.g. a retaining wall or circular foundation slab. The generalized stress resultants shown in Fig. 1.5

$$\boldsymbol{\sigma} = \{n_x, m_z, q_y, n_\theta, m_\theta\}^T, \quad (1.26)$$

are then assumed per 1m run. While the first three components appear only in the plane strain analysis, the other two arise when axisymmetric conditions apply. In particular,  $n_x, m_s, q_y$  represent the membrane (normal) force, bending moment and shear force, where as  $n_\theta$  and  $m_\theta$  are the circumferential (hoop) membrane force and circumferential (hoop) bending moment. For an isotropic beam element the above stress resultants are related to the generalized strains, that now involve extension and curvatures of the middle surface,

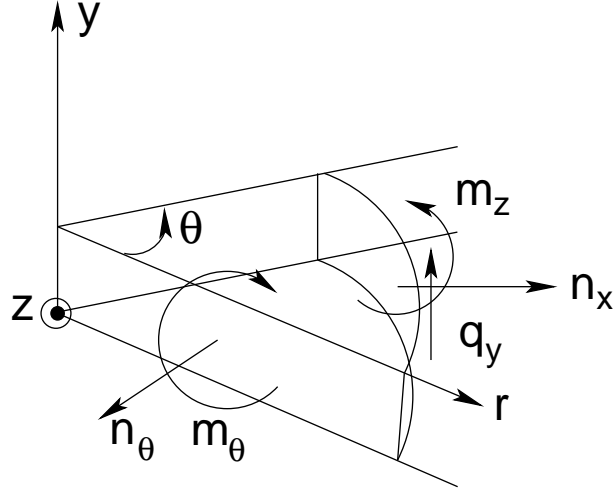


Figure 1.5: Stress resultants

through the material stiffness matrix  $\mathbf{D}$  in the form

$$\begin{Bmatrix} n_x \\ m_z \\ q_y \\ n_\theta \\ m_\theta \end{Bmatrix} = \frac{Eh}{1-\nu^2} \begin{bmatrix} 1 & 0 & 0 & \nu & 0 \\ 0 & \frac{h^2}{12} & 0 & 0 & \frac{\nu h^2}{12} \\ 0 & 0 & kGh & 0 & 0 \\ \nu & 0 & 0 & 1 & 0 \\ 0 & \frac{\nu h^2}{12} & 0 & 0 & \frac{h^2}{12} \end{bmatrix} \begin{Bmatrix} \frac{du}{dx} \\ -\frac{d\varphi_z}{dx} \\ -\varphi_z + \frac{dv}{dx} \\ \frac{v \sin \alpha - u \cos \alpha}{r} \\ -\frac{\theta \cos \alpha}{r} \end{Bmatrix}, \quad (1.27)$$

where  $h$  is the plate thickness and  $r$  is the circumferential radius. The material parameters  $E, \nu$  stand as usual for Young's modulus and Poisson's ratio. Finally, the unknown functions in the displacement field  $\mathbf{u} = \{u, \varphi, v\}^T$  stand for the longitudinal displacement, rotation about the  $z$ -axis and vertical displacement given in the local coordinate system, respectively. For plane strain analysis the last two rows in Eq. 1.27 are not included.

The components of the displacement field follow from the standard finite element approximation using the element shape functions and the nodal degrees of freedom

$$\mathbf{u} = \mathbf{N}\mathbf{a}. \quad (1.28)$$

**2-node beam element:** Detailed derivation of the finite element matrices for the 2-node beam element implemented in GEO FEM is given in [2]. Here we present only the most essential part. In particular, the matrix  $\mathbf{N}$  in Eq. (1.28) assumes the form

$$\mathbf{N} = \begin{bmatrix} N_1 & 0 & 0 & N_2 & 0 & 0 \\ 0 & -N_3 & N_4 & 0 & -N_5 & N_6 \\ 0 & N_7 & -N_8 & 0 & N_9 & -N_{10} \end{bmatrix}, \quad (1.29)$$

Table 1.1: Shape functions for 2-node beam element

Node $i$	Function $N_i$
1	$1 - r$
2	$r$
3	$\frac{1}{L(1 + 2\kappa)} [6r - 6r^2]$
4	$\frac{1}{1 + 2\kappa} [(1 + 2\kappa) - 2(2 + \kappa)r + 3r^2]$
5	$\frac{1}{L(1 + 3\kappa)} [-6r + 6r^2]$
6	$\frac{1}{1 + 2\kappa} [-2(1 - \kappa)r + 3r^2]$
7	$\frac{1}{1 + 2\kappa} [(1 + 2\kappa) - 2\kappa r - 3r^2 + 2r^3]$
8	$\frac{L}{1 + 2\kappa} [-(1 + \kappa)r + (2 + \kappa)r^2 - r^3]$
9	$\frac{1}{1 + 2\kappa} [2\kappa r + 3r^2 - 2r^3]$
10	$\frac{L}{1 + 2\kappa} [\kappa r + (1 - \kappa)r^2 - r^3]$

where individual shape functions are listed in Table 1.1. The variable  $\kappa$  that appears in individual terms of the shape functions is given by

$$\kappa = \frac{6EI_z}{kGAL^2},$$

where  $k$  is the shear correction factor and  $L$  is the length of the beam. The finite element representation of the strain field

$$\boldsymbol{\epsilon}^T = \left\{ \frac{du}{dx}, -\frac{d\varphi_z}{dx}, -\varphi_z + \frac{dv}{dx}, \frac{v \sin \alpha - u \cos \alpha}{r}, -\frac{\theta \cos \alpha}{r} \right\}, \quad (1.30)$$

calls for the introduction of the strain matrix  $\mathbf{B}$ . Using Eq. (1.29) and taking into account the transformation of coordinates from the local to the global coordinate system it is easy

Table 1.2: Shape functions for 3-node beam element

Node $i$	Regular function $N_i$	Substitute function $\bar{N}_i$
1	$\frac{1}{2}r(r-1)$	$\frac{1}{2}(\frac{1}{3}-r)$
2	$\frac{1}{2}r(r-1)$	$\frac{1}{2}(\frac{1}{3}+r)$
3	$(1-r^2)$	$\frac{2}{3}$

to see that

$$\mathbf{B} = \begin{bmatrix} CN'_1 & SN'_1 & 0 & CN'_2 & SN'_2 & 0 \\ -SN'_3 & CN'_3 & -N'_4 & -SN'_5 & CN'_5 & -N'_6 \\ -S(N_3 + N'_7) & C(N_3 + N'_7) & -N_4 - N'_8 & -S(N_5 + N'_9) & C(N_5 + N'_9) & -N_6 - N'_{10} \\ \frac{N_1}{r} & 0 & 0 & \frac{N_2}{r} & 0 & 0 \\ 0 & \frac{CN_3}{r} & -\frac{CN_4}{r} & \frac{CN_2}{r} & -\frac{CN_1}{r} & \end{bmatrix}, \quad (1.31)$$

where

$$\begin{aligned} C &= \cos(\alpha), \\ S &= \sin(\alpha), \\ N'_i &= \frac{1}{J} \frac{dN_i}{dr}. \end{aligned} \quad (1.32)$$

The angle  $\alpha$  in the above equation is defined in Fig. 1.4 and the Jacobian  $J$  follows from Eq. (1.39). The current radius is given by

$$r = \sum_{i=1}^2 N_i x_i. \quad (1.33)$$

**3-node beam element:** Assuming the standard isoparametric shape functions listed in Table 1.2 to approximate the displacement field gives the matrix  $\mathbf{N}$  in the form

$$\mathbf{N} = \begin{bmatrix} N_1 & 0 & 0 & N_2 & 0 & 0 & N_3 & 0 & 0 \\ 0 & N_1 & 0 & 0 & N_2 & 0 & 0 & N_3 & 0 \\ 0 & 0 & N_1 & 0 & 0 & N_2 & 0 & 0 & N_3 \end{bmatrix}, \quad (1.34)$$

Next, recall the representation of the strain field (1.30) and use Eq. (1.34) to arrive at

$$\mathbf{B} = \begin{bmatrix} CN'_1 & SN'_1 & 0 & CN'_2 & SN'_2 & 0 & CN'_3 & SN'_3 & 0 \\ 0 & -N'_1 & 0 & 0 & -N'_2 & 0 & -N'_3 & 0 & 0 \\ -SN'_1 & CN'_1 & \bar{N}_1 & -SN'_2 & CN'_2 & \bar{N}_2 & -SN'_3 & CN'_3 & \bar{N}_3 \\ \frac{\bar{N}_1}{r} & 0 & 0 & \frac{\bar{N}_2}{r} & 0 & 0 & \frac{\bar{N}_3}{r} & 0 & 0 \\ 0 & 0 & -\frac{C\bar{N}_1}{r} & 0 & 0 & -\frac{C\bar{N}_2}{r} & 0 & 0 & -\frac{C\bar{N}_3}{r} \end{bmatrix}. \quad (1.35)$$

The standard  $\mathbf{B}$  matrix was again augmented to account for the transformation of coordinates. Parameters  $C, S, N'_i$  receive the same meaning as in Eq. (1.32) with the Jacobian  $J$  found from Eq. (1.40). For the circumferential strain terms the current radius  $r$  now becomes [29]

$$r = \sum_{i=1}^3 \bar{N}_i x_i. \quad (1.36)$$

In addition, substitute shape functions  $\bar{N}_i$  were used to define the variation of  $\varphi$  in the definition of shear strain  $-\varphi_z + \frac{dv}{dx}$  to avoid shear force locking. Note that the substitute shape functions coincide with the regular shape functions at the reduced Gaussian integration points. Details can be found in [6, 29].

### Element stiffness matrix

Derivation of the stiffness matrix follows Eq. (1.17). The result is

- Plane strain analysis

$$\mathbf{K}_e = \sum_{j=1}^N w_j \mathbf{B}^T(r_j) \mathbf{D} \mathbf{B}(r_j) J, \quad (1.37)$$

- Axisymmetric analysis

$$\mathbf{K}_e = \sum_{j=1}^N w_j \mathbf{B}^T(r_j) \mathbf{D} \mathbf{B}(r_j) J r, \quad (1.38)$$

where the Jacobian  $J$  reads

$$J = L \quad \text{for } 2\text{-node element}, \quad (1.39)$$

$$J = \frac{L}{2} \quad \text{for } 3\text{-node element}. \quad (1.40)$$

Locations of integration points within parent elements are stored in Table 1.3.

Table 1.3: Integration points for 2-node and 3-node beam elements

Integration point	2-node beam		3-node beam	
	coordinate $r$	weight	coordinate $r$	weight
1	0.211324865	1.0	-0.774596669241483	5/9
2	0.788675131	1.0	0.0	8/9
3			0.774596669241483	5/9

### 1.3.3 Plane 3-node and 6-node triangular elements

Plane 3-node and 6-node isoparametric triangular elements are implemented in GEO FEM. Geometry of both elements is evident from Fig. 1.6.

#### Kinematics

The displacement interpolation functions are listed in Table 1.4. The element degrees of freedom are

$$\mathbf{a} = \{u_1, v_1, u_2, v_2, u_3, v_3\}^T \quad 3\text{-node elem}, \quad (1.41)$$

$$\mathbf{a} = \{u_1, v_1, u_2, v_2, u_3, v_3, u_4, v_4, u_5, v_5, u_6, v_6\}^T \quad 6\text{-node elem}. \quad (1.42)$$

The displacement field inside the element is uniquely described by the above nodal parameters

$$u = \sum_{i=1}^n N_i u_i, \quad v = \sum_{i=1}^n N_i v_i, \quad (1.43)$$

where  $n$  is the number of element nodes.

#### Element stiffness matrix

The components of the strain tensor follow from Eq. (1.6). The element stiffness matrix is then defined by Eq. (1.17). Here, the integral is again evaluated by Gaussian quadrature so that

- Plane strain analysis

$$\mathbf{K}_e = \sum_{j=1}^N w_j \mathbf{B}^T(r_j, s_j, \frac{1}{J}) \mathbf{D} \mathbf{B}(r_j, s_j, \frac{1}{J}) J(r_j, s_j), \quad (1.44)$$

Table 1.4: Interpolation functions for 3-node and 6-node triangular elements

Node $i$	Function $N_i$	Included only if node $i$ is defined		
		$i = 4$	$i = 5$	$i = 6$
1	$1 - r - s$	$-\frac{1}{2}N_4$		$-\frac{1}{2}N_6$
2	$r$	$-\frac{1}{2}N_4$	$-\frac{1}{2}N_5$	
3	$s$		$-\frac{1}{2}N_5$	$-\frac{1}{2}N_6$
4	$4r(1 - r - s)$			
5	$4rs$			
6	$4s(1 - r - s)$			

Table 1.5: Integration points for a 3-node triangular element

Integration point	Coordinate $r$	Coordinate $s$	Weight
1	1/3	1/3	1/2

Table 1.6: Integration points for a 6-node triangular element

Integration point	Coordinate $r$	Coordinate $s$	Weight
1	0.1012865073235	0.1012865073235	0.1259391805448
2	0.7974269853531	0.1012865073235	0.1259391805448
3	0.1012865073235	0.7974269853531	0.1259391805448
4	0.4701420641051	0.0597158717898	0.1323941527885
5	0.4701420641051	0.4701420641051	0.1323941527885
6	0.0597158717898	0.4701420641051	0.1323941527885
7	0.3333333333333	0.3333333333333	0.2250000000000



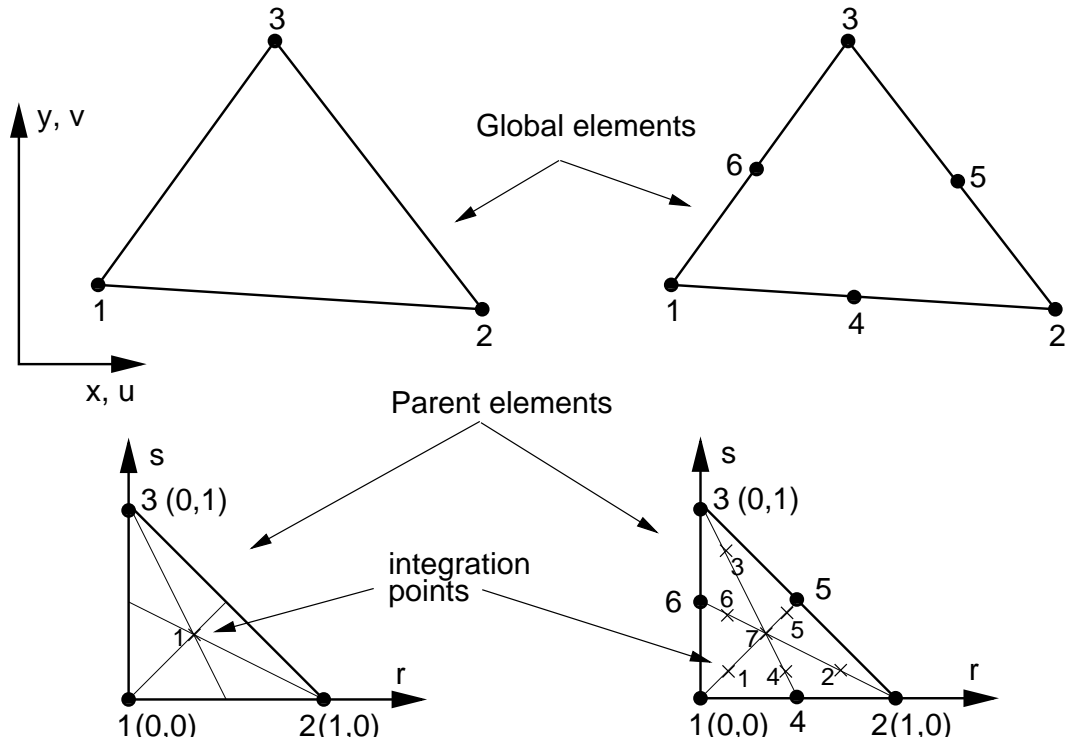


Figure 1.6: 4-node and 6-node interface elements

- Axisymmetric analysis

$$\mathbf{K}_e = \sum_{j=1}^N w_j \mathbf{B}^T(r_j, s_j, \frac{1}{J}) \mathbf{D} \mathbf{B}(r_j, s_j, \frac{1}{J}) J(r_j, s_j) r, \quad (1.45)$$

where  $w_i$  is the weight for a given integration point  $i$ ,  $N$  is the number of integration points and  $J$  is the Jacobian of the transformation given by

$$J(r, s) = \frac{\partial x}{\partial r} \frac{\partial y}{\partial s} - \frac{\partial x}{\partial s} \frac{\partial y}{\partial r}. \quad (1.46)$$

The linear 3-node element is integrated at one integration point, while  $N = 7$  is assumed for the quadratic 6-node element, see Fig. 1.6. Locations of integration points within parent elements are stored in Tables 1.5 and 1.6. Further details on the evaluation of the element stiffness matrix can be found in [2].

### Element load vector

In this section, we turn our attention to the evaluation of element load vector attributed to the gravity loading, pore pressure loading and loading that arise during excavation.

*Gravity loading:* The forces generated by the self weight of the soil follow from the first term on the right hand side of Eq. (1.18) and are given by

$$\mathbf{f}_e^{gr} = \int_{V_e} \mathbf{N}^T \mathbf{X}_e^\gamma dV_e, \quad (1.47)$$

where  $\mathbf{X}_e^\gamma = \{0, \gamma_e\}^T$  and  $\gamma_e$  is the element self-weight per unit volume. The integral in Eq. (1.47) thus redistributes the net vertical force to all element nodes.

*Pore pressure:* To arrive at the element load vector due to the prescribed pore pressure we first recall the concept of effective stresses. The total stress vector then assumes the form

$$\boldsymbol{\sigma} = \mathbf{D}\boldsymbol{\epsilon} - 3m\bar{p}, \quad (1.48)$$

where  $\bar{p} > 0$  represents the prescribed liquid pore pressure in the fully saturated soil. Matrix  $\mathbf{D}$  now stands for the stiffness matrix of the porous skeleton and vector  $\mathbf{m}$  is introduced later in Section 2.3.1 Eq. (2.2). Also note that the matrix of the solid phase of the porous skeleton is taken as rigid (undeformable). Eq. (1.14) now becomes

$$\boldsymbol{\sigma} = \mathbf{B}\mathbf{D}\mathbf{a} - \mathbf{N}\bar{p}, \quad (1.49)$$

where vector  $\bar{p}$  stores the nodal values of the prescribed pore pressure. Introducing Eq. (1.49) into Eq. (1.15) then gives (recall the second term on the right hand side of Eq. (1.18))

$$\mathbf{f}_e^{pp} = - \int_{V_e} \mathbf{B}^T \mathbf{N}_e \bar{p} dV_e. \quad (1.50)$$

*Excavation problem:* When a portion of material is excavated (open excavation, tunneling) forces must be applied along the excavated surface such that the remaining material experiences the correct unloading effect and the new free surface is stress free [34, 4]. The excavation procedure is schematically displayed in Fig. 1.7. Suppose that prior to excavation the material in the original body is loaded to attain the initial stresses  $\sigma_{A_0}$  in zone A and  $\sigma_{B_0}$  in zone B, respectively. This initial stress state can be recovered as a superposition of two loading stages. To that end, suppose that the material from zone A is removed. To maintain the initial stress state  $\sigma_{B_0}$  developed in zone B the new free surface must be loaded by forces  $F_{AB}$  exerted by body A on to body B. Similarly, the forces  $F_{BA}$  having the same magnitude but opposite direction as forces  $F_{AB}$  must be applied to body A to comply with the equilibrium requirements. It now becomes evident that in order to complete the excavation procedure the unwanted layer of forces  $F_{AB}$  must be removed by applying force  $F_{BA}$  to body B thus arriving at the required stress free surface, Fig. 1.7.

In mathematical terms the excavation forces  $F_{BA}$  follow from the principle of virtual work written as

$$\int_{\Omega_A} \delta\boldsymbol{\epsilon}^T \boldsymbol{\sigma}_{A_0} d\Omega = \int_{\Omega_A} \delta\mathbf{u}^T \mathbf{X}^\gamma d\Omega + \int_{\Gamma_A} \delta\mathbf{u}^T \mathbf{t} d\Gamma. \quad (1.51)$$

After discretization Eq. (1.51) becomes

$$\mathbf{A}_{e=1}^{N_{eA}} \left( \delta\mathbf{a}_e^T \int_{V_e} \mathbf{B}^T \boldsymbol{\sigma}_{A_0e} dV_e - \delta\mathbf{a}_e^T \int_{V_e} \mathbf{N}^T \mathbf{X}_e^\gamma dV_e \right) = \delta\mathbf{a}_{AB}^T \mathbf{F}_{BA}. \quad (1.52)$$

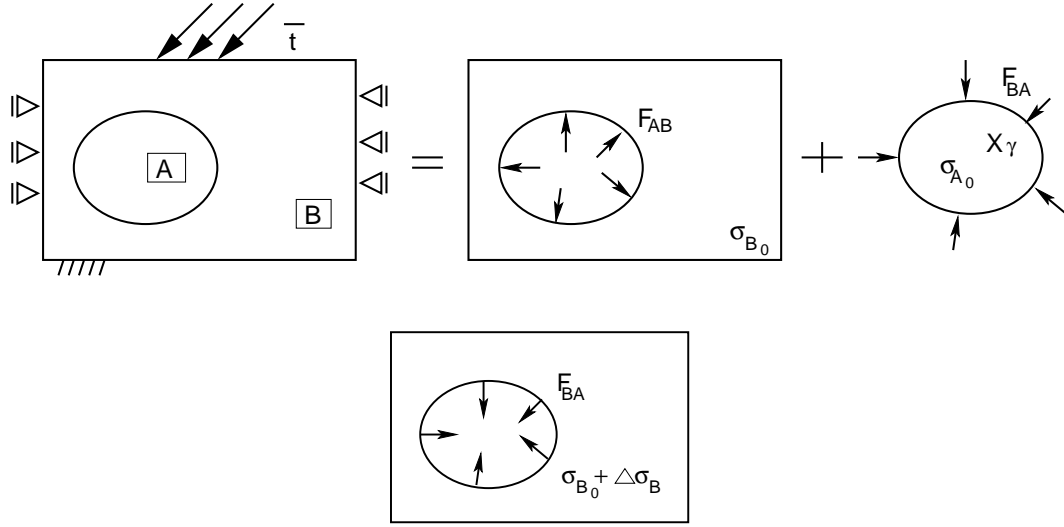


Figure 1.7: Excavation process and excavation forces

The final step requires relating the element nodal degrees of freedom to the degrees of freedom associated with the nodes on the new free surface. This can be done with the help of the localization matrix  $\mathbf{L}$  such that

$$\mathbf{a}_e = \mathbf{L}_e \mathbf{a}_{BA}. \quad (1.53)$$

Substituting Eq. (1.53) into Eq. (1.52) finally gives the vector of excavation forces in the form

$$\mathbf{F}_{BA} = \mathbf{A} \begin{matrix} N_{eA} \\ e=1 \end{matrix} \left( \int_{V_e} \mathbf{L}_e^T \mathbf{B}^T \boldsymbol{\sigma}_{A_0e} dV_e - \int_{V_e} \mathbf{L}_e^T \mathbf{N}^T \mathbf{X}_e^\gamma dV_e \right). \quad (1.54)$$

The localization procedure as shown in Fig. 1.8 essentially corresponds to the selection of elements attached to the excavation surface. Thus the remaining elements present in body A do not have to be taken into account when computing the excavation forces  $\mathbf{F}_{BA}$  in Eq. (1.54).

The theoretical grounds set in the above paragraphs are demonstrated on a simple problem of open excavation. Figs. 1.9-1.11 illustrate a sequence of computational tasks presented in Fig. 1.7. The initial state prior to excavation is represented by Fig. 1.9 showing a variation of the horizontal stress due to pure gravity loading. Fig. 1.10 then corresponds to the state found in body B on Fig. 1.7 after removing the soil from open cut but keeping the original stresses by applying forces  $F_{AB}$  along the new free boundaries. Finally, Fig. 1.11 displays the final deformation and stress state after removing the unwanted forces  $F_{AB}$  with the help of forces  $F_{BA}$  that have the same magnitude but opposite direction, see Fig. 1.7 showing body B after completing the excavation sequence.

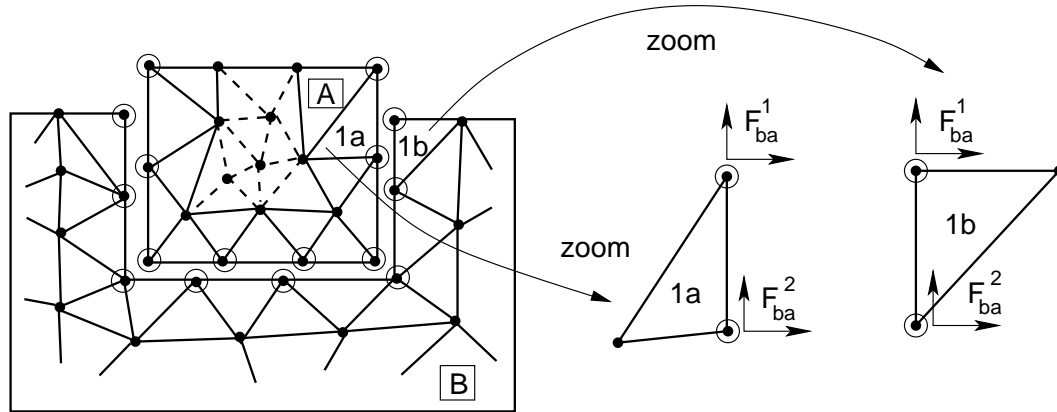


Figure 1.8: Localization

Table 1.7: Interpolation functions for 4-node and 6-node interface elements

Node $i$	Function $N_i$	Included only if node 3 is defined
1	$\frac{1}{2}(1 - r)$	$-\frac{1}{2}N_3$
2	$\frac{1}{2}(1 + r)$	$-\frac{1}{2}N_3$
3	$(1 - r^2)$	

### 1.3.4 4-node and 6-node interface elements

This section presents the derivation of the element stiffness matrix for the 4-node and 6-node interface elements that are compatible with 3-node and 6-node triangular elements, respectively, also implemented within the GEO FEM finite element code. Both elements are displayed in Fig. 1.12.

#### Kinematics

In the finite element framework the global displacements are approximated using the standard element shape functions listed in Table 1.7. Referring to Fig 1.12 the displacement field for the 4-node interface element receives the form

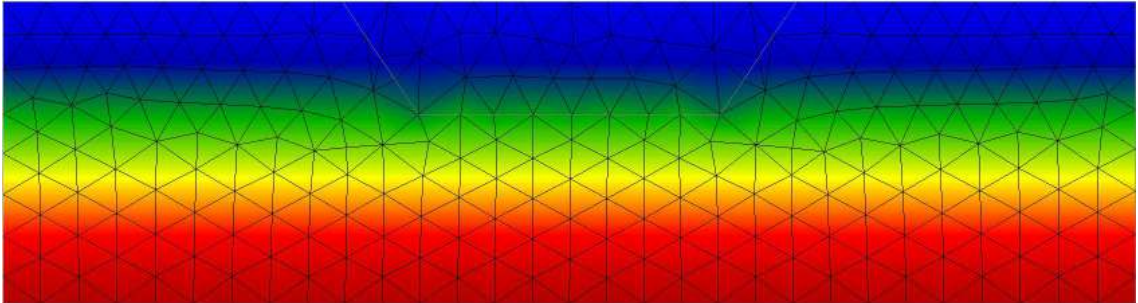


Figure 1.9: Excavation procedure – initial state

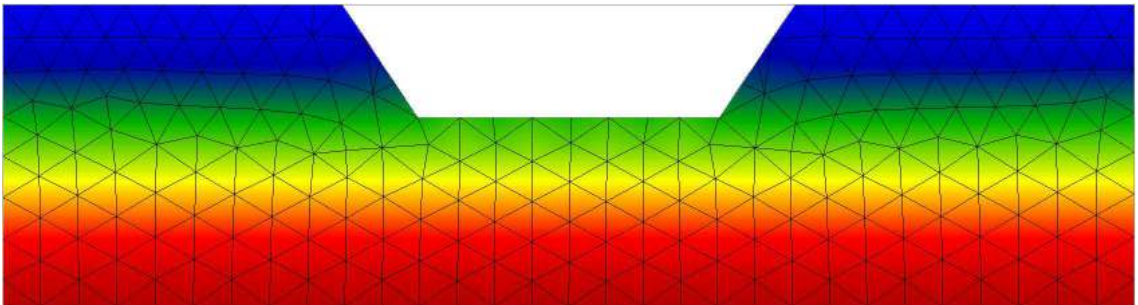


Figure 1.10: Excavation procedure – intermediate state

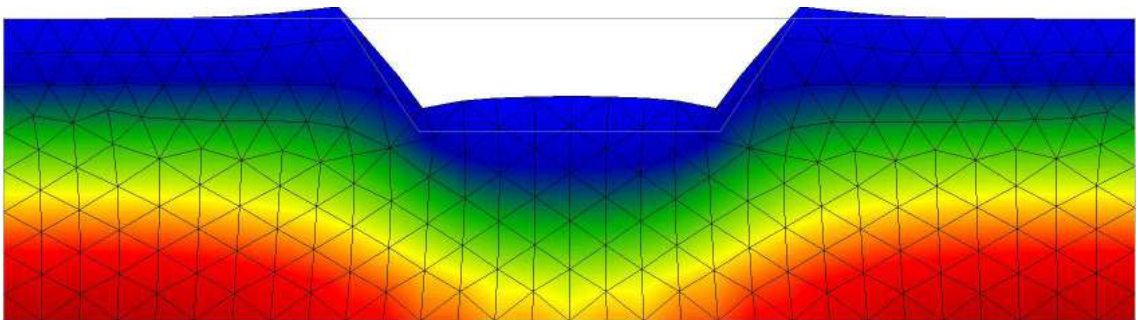


Figure 1.11: Excavation procedure – final state

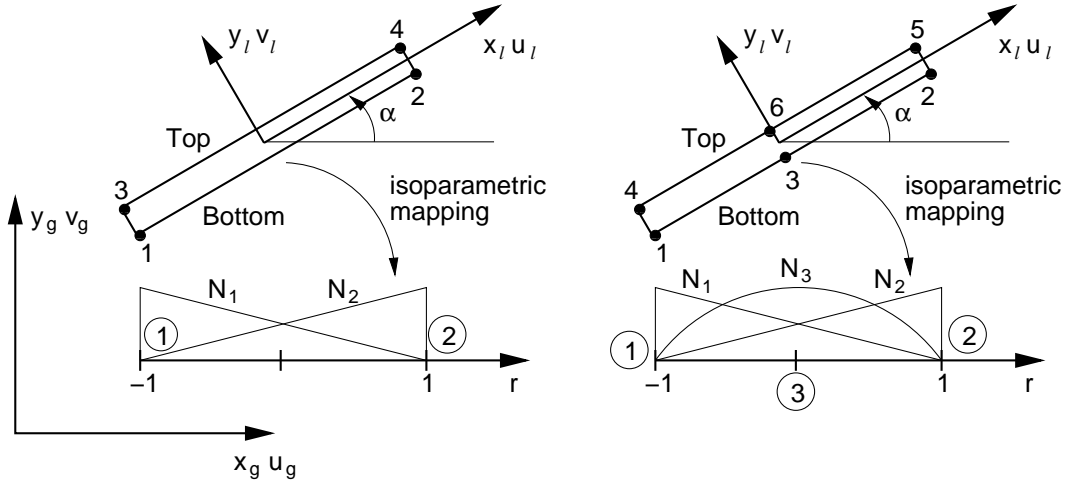


Figure 1.12: 4-node and 6-node interface elements

$$\begin{aligned}
 u^{top} &= N_1 u_3 + N_2 u_4, \\
 u^{bot} &= N_1 u_1 + N_2 u_2, \\
 v^{top} &= N_1 v_3 + N_2 v_4, \\
 v^{bot} &= N_1 v_1 + N_2 v_2,
 \end{aligned} \tag{1.55}$$

In the compact form the global nodal degrees of freedom  $u_i, v_i$  are

$$\mathbf{a}_g = \{u_1, v_1, u_2, v_2, u_3, v_3, u_4, v_4\}^T. \tag{1.56}$$

Similarly for the 6-node interface element we get

$$\begin{aligned}
 u^{top} &= N_1 u_4 + N_2 u_5 + N_3 u_6, \\
 u^{bot} &= N_1 u_1 + N_2 u_2 + N_3 u_3, \\
 v^{top} &= N_1 v_4 + N_2 v_5 + N_3 v_6, \\
 v^{bot} &= N_1 v_1 + N_2 v_2 + N_3 v_3,
 \end{aligned} \tag{1.57}$$

and

$$\mathbf{a}_g = \{u_1, v_1, u_2, v_2, u_3, v_3, u_4, v_4, u_5, v_5, u_6, v_6\}^T. \tag{1.58}$$

### Element stiffness matrix

The stress-displacement relationship of the interface model assumes the form

$$\begin{Bmatrix} \tau \\ \sigma \end{Bmatrix} = \mathbf{D} \begin{Bmatrix} \llbracket u \rrbracket_l \\ \llbracket v \rrbracket_l \end{Bmatrix}, \tag{1.59}$$

where  $\llbracket u \rrbracket_l$  and  $\llbracket v \rrbracket_l$  represent the relative displacements of the top and bottom of the interface element in the local coordinate system, Fig. 1.12. For isotropic linear elastic

behavior the interface material stiffness matrix  $\mathbf{D}$  takes the form

$$\mathbf{D} = \begin{bmatrix} K_s & 0 \\ 0 & K_n \end{bmatrix}, \quad (1.60)$$

where  $K_s$  and  $K_n$  are the elastic shear and normal stiffnesses, respectively. They can be related to the interface shear and Young's moduli  $G_{int}, E_{int}$  as

$$\begin{aligned} K_s &= \frac{G_{int}}{t}, \\ K_n &= \frac{E_{int}}{t}, \end{aligned}$$

where  $t$  represents the interface stiffness. It should be noted here that setting the interface stiffnesses  $K_s, K_n$  to low values may lead to excessively large elastic displacements. However, if the elastic parameters are too large (attempt to model a perfect bond), then the numerical ill-conditioning may occur. This is usually manifested by the oscillation of interface stresses. It has been argued that such unwanted oscillatory behavior can be reduced by using the Newton-Cotes integration scheme (integration points coincide with the element nodes) when computing the element stiffness matrix [8, 13]. This integration scheme is employed in GEO FEM. On the contrary, the results presented in [7] suggest that the use of the Newton-Cotes integration scheme has no benefit over the Gaussian quadrature.

The global degrees of freedom in Eqs. (1.56) and (1.58) are related to local displacements in the form

$$\begin{Bmatrix} \llbracket u \rrbracket_l \\ \llbracket v \rrbracket_l \end{Bmatrix} = \mathbf{B} \mathbf{a}_g, \quad (1.61)$$

where the matrix  $\mathbf{B}$  assumes the form

$$\mathbf{B} = [-\mathbf{T}\mathbf{B}_1 \quad -\mathbf{T}\mathbf{B}_2 \quad \mathbf{T}\mathbf{B}_1 \quad \mathbf{T}\mathbf{B}_2] \quad 4\text{-node elem}, \quad (1.62)$$

$$\mathbf{B} = [-\mathbf{T}\mathbf{B}_1 \quad -\mathbf{T}\mathbf{B}_2 \quad -\mathbf{T}\mathbf{B}_3 \quad \mathbf{T}\mathbf{B}_1 \quad \mathbf{T}\mathbf{B}_2 \quad \mathbf{T}\mathbf{B}_3] \quad 6\text{-node elem}. \quad (1.63)$$

and

$$\mathbf{T} = \begin{bmatrix} \cos \alpha & \sin \alpha \\ -\sin \alpha & \cos \alpha \end{bmatrix} \quad \mathbf{B}_i = \begin{bmatrix} N_i & 0 \\ 0 & N_i \end{bmatrix}. \quad (1.64)$$

The element stiffness matrix  $\mathbf{K}_e$  then follows from

$$\mathbf{K}_e = \frac{L}{2} \int_{-1}^1 \mathbf{B}^T \mathbf{D} \mathbf{B} \, dr, \quad (1.65)$$

where  $L$  is the element length.

### Element load vector

We limit our attention to the element load due to pore pressure. Assuming drained boundary conditions and using the concept of effective stresses gives the vector of total stresses in the form

$$\begin{Bmatrix} \tau \\ \sigma \end{Bmatrix} = [\mathbf{D}] \begin{Bmatrix} \llbracket u \rrbracket_l \\ \llbracket v \rrbracket_l \end{Bmatrix} - \begin{Bmatrix} 0 \\ 1 \end{Bmatrix} \bar{p}, \quad (1.66)$$

where the average value of pore pressure  $\bar{p}$  is given by

$$\bar{p} = \frac{1}{2} [(p_1 + p_3)N_1 + (p_2 + p_4)N_2] \quad 4\text{-node elem}, \quad (1.67)$$

$$\bar{p} = \frac{1}{2} [(p_1 + p_4)N_1 + (p_2 + p_5)N_2 + (p_3 + p_6)N_3] \quad 6\text{-node elem}. \quad (1.68)$$

Finally, recall the second term in Eq. (1.18) to get the element load vector  $\mathbf{f}_e$  due to initial pore pressure as

$$\mathbf{f}_e = \frac{L}{2} \int_{-1}^1 \mathbf{B}^T \begin{Bmatrix} 0 \\ 1 \end{Bmatrix} \bar{p} \, dr. \quad (1.69)$$



# Chapter 2

## Basic constitutive models for soils

### 2.1 Elastic constitutive model for soils

Although not realistic for soils, the program makes it possible to analyze a purely elastic isotropic material. A typical stress-strain curve for a linear elastic material is plotted in Fig. 2.1. Note that such a model assumes that the loading and unloading branch coincide.

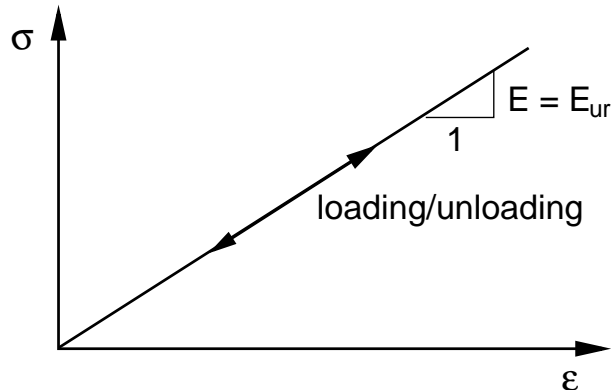


Figure 2.1: Linear elastic constitutive model for soil

The assumption of isotropy (all material constants are independent of the orientation of the coordinate axes) is common for all material models implemented in GEO FEM. In such a case there are only two independent material constants necessary to represent the material behavior, e.g., the Young modulus  $E$  and Poisson ratio  $\nu$ . Limiting our attention to the plane-strain conditions, the incremental constitutive equation for a linear elastic isotropic material reads

$$\begin{Bmatrix} \sigma_{xx} \\ \sigma_{yy} \\ \tau_{xy} \\ \sigma_{zz} \end{Bmatrix} = \frac{E}{(1+\nu)(1-2\nu)} \begin{bmatrix} 1-\nu & \nu & 0 & \nu \\ \nu & 1-\nu & 0 & \nu \\ 0 & 0 & \frac{1-2\nu}{2} & 0 \\ \nu & \nu & 0 & 1-\nu \end{bmatrix} \begin{Bmatrix} \varepsilon_{xx} \\ \varepsilon_{yy} \\ \gamma_{xy} \\ \varepsilon_{zz} \end{Bmatrix}. \quad (2.1)$$

## 2.2 Modified elastic constitutive model for soils

A slightly more realistic prediction of the material behavior can be achieved when assuming a different material response in loading and unloading. Such an approach calls for a third independent material parameter governing the unloading-reloading branch of the stress strain curve as shown in Fig. 2.2. Experimental evidence suggests to set the value of the unloading-reloading Young's modulus  $E_{ur}$  to approximately three times the value of  $E$ . This is the default setting in GEO FEM.

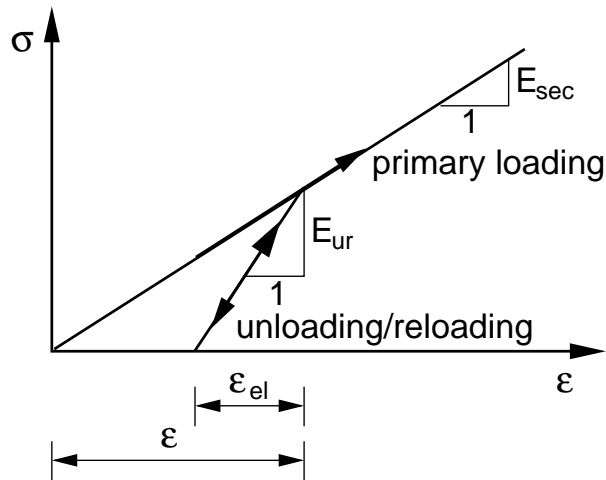


Figure 2.2: Modified linear elastic constitutive model for soil

## 2.3 Basic elasto-plastic constitutive models for soils

One of the key topics in the geomechanical engineering is an assessment of stability and ultimate load bearing capacity of soils. Although a number of simple approaches based on limit equilibrium are available for the solution of this problem such as the Petterson, Bishop or Sarma methods, there is an increasing need for more accurate and reliable approaches that take the actual behavior of soils into account, especially in applications involving soils that show softening behavior, e.g., dense sands or overconsolidated clays, see Fig. 2.3.

The purpose of this chapter is to review several constitutive models commonly known to geotechnical engineers. The chapter starts with the classical von Mises model [2, 29] often used when assuming the *total stress approach*. Although this model is not currently implemented within the GEO FEM software, we take advantage of its simplicity and use it as a stepping stone for more complex constitutive models such as the Drucker-Prager and the modified Mohr-Coulomb models discussed next. Note that unlike the von Mises constitutive model, these models draw on the use of *effective parameters*.

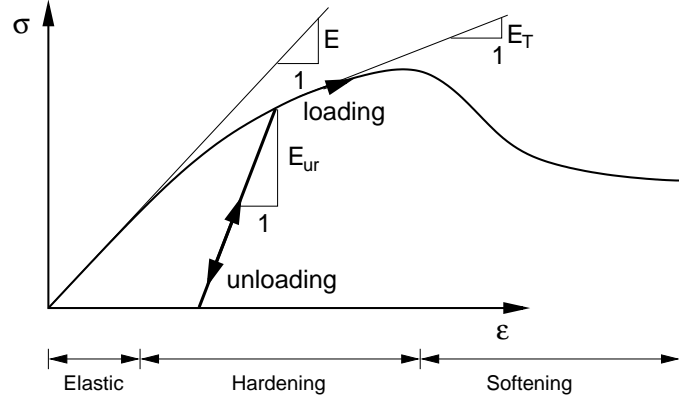


Figure 2.3: Typical soil behavior involving hardening and softening

### 2.3.1 Invariants

Before proceeding with the actual formulation of individual constitutive models we first define the following matrices and vectors extensively used in this chapter:

$$\mathbf{m} = \{1/3, 1/3, 0, 1/3\}^T,$$

$$\mathbf{P} = \begin{bmatrix} 2/3 & -1/3 & 0 & -1/3 \\ -1/3 & 2/3 & 0 & -1/3 \\ 0 & 0 & 2 & 0 \\ -1/3 & -1/3 & 0 & 2/3 \end{bmatrix}, \quad \mathbf{Q} = \begin{bmatrix} 1 & 0 & 0 & 0 \\ 0 & 1 & 0 & 0 \\ 0 & 0 & 1/2 & 0 \\ 0 & 0 & 0 & 1 \end{bmatrix}, \quad (2.2)$$

with the following useful connections

$$\mathbf{m}^T \mathbf{Q} \mathbf{m} = \mathbf{m}^T \mathbf{m} = \frac{1}{3}, \quad \mathbf{P} \mathbf{Q} \mathbf{P} = \mathbf{P}, \quad \mathbf{P} \mathbf{Q} \mathbf{m} = \mathbf{0}. \quad (2.3)$$

In addition, standard engineering representation of stress and strain is used throughout the text. Assuming the Cartesian coordinate system with axes  $x, y$  and  $z$ , Fig. 1.1, and the plain strain state of stress, the symmetric second order Cauchy stress tensor  $\boldsymbol{\sigma}$  is then represented as  $(4 \times 4)$  vector (in the case of axi-symmetric analysis the  $z$ -direction is replaced by the circumferential  $\theta$ -direction with the corresponding notation introduced in Chapter 1)

$$\boldsymbol{\sigma} = \{\sigma_{xx}, \sigma_{yy}, \sigma_{xy}, \sigma_{zz}\}^T. \quad (2.4)$$

Similarly we write the symmetric second-order tensor of small strains  $\boldsymbol{\varepsilon}$  in the form

$$\boldsymbol{\varepsilon} = \{\varepsilon_{xx}, \varepsilon_{yy}, \gamma_{xy}, \varepsilon_{zz}\}^T. \quad (2.5)$$

The deviatoric counterparts of stress  $\boldsymbol{\sigma}$  and strain  $\boldsymbol{\varepsilon}$  are then given by

$$\mathbf{s} = \mathbf{PQ}\boldsymbol{\sigma}, \quad \mathbf{e} = \mathbf{PQ}\boldsymbol{\varepsilon}. \quad (2.6)$$

The state of stress at a given material point provided by Eq. (2.4) can be also written in terms of three basic invariants. Assuming standard elasticity notation (pressure is negative) these invariants can be written with the help of Eq. (2.2) as

$$\sigma_m = \mathbf{m}^\top \boldsymbol{\sigma}, \quad (2.7)$$

$$J = \sqrt{\frac{1}{2} \boldsymbol{\sigma}^\top \mathbf{P} \boldsymbol{\sigma}}, \quad (2.8)$$

$$\theta = -\frac{1}{3} \arcsin \left( \frac{3\sqrt{3} I_{3s}}{2 J^3} \right), \quad (2.9)$$

where  $\sigma_m$  is the effective mean stress,  $J$  is defined as a square root of the second invariant of the deviatoric stress and  $\theta$  is Lode's angle;  $I_{3s}$  in Eq. (2.9) stands for the third invariant of the deviatoric stress. Assuming plane strain conditions the quantity  $I_{3s}$  takes the following form

$$I_{3s} = s_{xx}s_{yy}s_{zz} - s_{zz}s_{xy}s_{xy}, \quad (2.10)$$

where  $s_{ij}$  are the components of the deviatoric stress tensor given by Eq. (2.6). It becomes also advantageous, later in this chapter, to define certain equivalent measures of strain vectors  $\boldsymbol{\varepsilon}$  and  $\mathbf{e}$  as

$$\varepsilon_{eq} = \sqrt{\frac{2}{3} \boldsymbol{\varepsilon}^\top \mathbf{Q} \boldsymbol{\varepsilon}}, \quad (2.11)$$

$$E_d = \sqrt{2 \boldsymbol{\varepsilon}^\top \mathbf{QPQ} \boldsymbol{\varepsilon}}. \quad (2.12)$$

### 2.3.2 Yield surface

It is the well known fact that the plastic behavior of solids in general is characterized by a non-unique stress-strain relationship. Evidence of such a behavior is the presence of irrecoverable (plastic) strains ( $\boldsymbol{\varepsilon}$ ) upon unloading. Fig. 2.4 provides an illustrative example of uniaxial behavior of a material loaded beyond the elastic limit. The plastic strains attributed to yielding, however, can occur only if the stresses  $\boldsymbol{\sigma}$  satisfy a certain yield criterion

$$F(\boldsymbol{\sigma}, \boldsymbol{\kappa}) = 0, \quad (2.13)$$

where the components of vector  $\boldsymbol{\kappa} = \{\kappa_1, \kappa_2, \dots\}^\top$  are called the hardening/softening parameters. If the material exhibits hardening/softening, the surface described by Eq. (2.13) expands/contracts depending on the loading history and the hardening/softening parameters  $\boldsymbol{\kappa} = \boldsymbol{\kappa}(t)$ . The condition  $F(\boldsymbol{\sigma}, \boldsymbol{\kappa}) < 0$  then corresponds either to initial elastic loading, or elastic unloading from a previously reached plastic state. In a time interval during which the material remains in a plastic state, the yield condition Eq. (2.13) is satisfied (recall that  $F(\boldsymbol{\sigma}, \boldsymbol{\kappa}) > 0$  is not admissible). After differentiating the yield condition

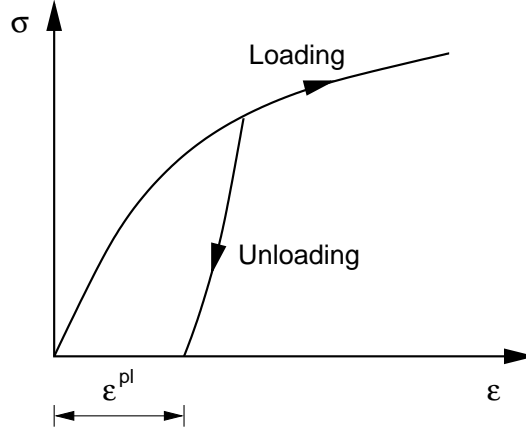


Figure 2.4: Uniaxial plastic behavior

we arrive at the so called *consistency condition* [2]

$$dF = \left( \frac{\partial F}{\partial \boldsymbol{\sigma}} \right)^\top d\boldsymbol{\sigma} + \left( \frac{\partial F}{\partial \boldsymbol{\kappa}} \right)^\top d\boldsymbol{\kappa} = 0, \quad (\text{valid for plastic yielding}) \quad (2.14)$$

where, under plane strain state of stress,

$$\begin{aligned} \frac{\partial F}{\partial \boldsymbol{\sigma}} &= \left\{ \frac{\partial F}{\partial \sigma_{xx}}, \frac{\partial F}{\partial \sigma_{yy}}, \frac{\partial F}{\partial \sigma_{xy}}, \frac{\partial F}{\partial \sigma_{zz}} \right\}^\top, \\ \frac{\partial F}{\partial \boldsymbol{\kappa}} &= \left\{ \frac{\partial F}{\partial \kappa_1}, \frac{\partial F}{\partial \kappa_2}, \dots, \frac{\partial F}{\partial \kappa_k} \right\}^\top. \end{aligned} \quad (2.15)$$

Apart from the yield condition, Eq. (2.13), the description of the plastic deformation requires a certain assumption about the direction of the plastic flow. Such an hypothesis is called the flow rule. It is postulated that the plastic flow will occur in the direction normal to a *plastic potential surface*

$$G = G(\boldsymbol{\sigma}, \boldsymbol{\kappa}). \quad (2.16)$$

The plastic strain increment can be then defined as

$$d\boldsymbol{\varepsilon}^{pl} = d\lambda \frac{\partial G}{\partial \boldsymbol{\sigma}}, \quad (2.17)$$

where  $d\lambda$  is a proportionality constant, as yet undetermined. Since  $d\lambda$  determines the magnitude of the plastic flow it is clear that  $d\lambda > 0$  for plastic yielding and is equal to zero when the stress point is found inside the yield surface. The special case of  $G = F$  is known as associated plasticity and the flow rule Eq. (2.16) is termed the normality rule. In the general case, however, when  $G \neq F$  the plasticity is non-associated. The parameter  $d\lambda$  can be eliminated using the consistency condition Eq. (2.14) written in Melan's form as

$$dF = \left( \frac{\partial F}{\partial \boldsymbol{\sigma}} \right)^\top d\boldsymbol{\sigma} - Hd\lambda = 0, \quad (\text{valid for plastic yielding}) \quad (2.18)$$

where

$$H = -\left(\frac{\partial F}{\partial \boldsymbol{\kappa}}\right)^\top \frac{\partial \boldsymbol{\kappa}}{\partial \lambda}, \quad (2.19)$$

is the modulus of plastic hardening/softening. To account also for the case when the material is either loaded in the elastic regime or elastically unloaded preceded by plastic yielding the consistency condition may receive a more general form

$$d\lambda dF = 0. \quad (2.20)$$

Eq. (2.20) is equivalent to the *loading-unloading conditions*

$$d\lambda \geq 0, \quad F(\boldsymbol{\sigma}, \boldsymbol{\kappa}) \leq 0, \quad d\lambda F(\boldsymbol{\sigma}, \boldsymbol{\kappa}) = 0. \quad (2.21)$$

These conditions are often referred to as the *Karush-Kuhn-Tucker conditions* [17](Chapter 15.2.2). Clearly, for elastic unloading  $dF < 0$  and for plastic loading  $d\lambda > 0$  and thus  $F(\boldsymbol{\sigma}, \boldsymbol{\kappa}) = 0$  (stress must remain on the yield surface) and  $dF = 0$  from consistency condition.

### 2.3.3 Elasto-plastic stiffness matrix

This section completes the summary of the general theoretical grounds needed for the description of plastic behavior of solids by formulating the elasto-plastic material stiffness matrix. Two approaches are examined to arrive at the desired result. The first approach draws on the standard incremental form of constitutive equations combined with the consistency condition given by Eq. (2.14), while the second approach confirms with the actual algorithmic procedure for the stress update. The interested reader may also consult an excellent paper on this subject by Simo and Taylor [33].

#### Standard tangent stiffness matrix

Assuming additive decomposition of small strains the total strain vector admits the following representation

$$d\boldsymbol{\varepsilon} = d\boldsymbol{\varepsilon}^{el} + d\boldsymbol{\varepsilon}^{pl}. \quad (2.22)$$

Relating the increment of stress  $d\boldsymbol{\sigma}$  during plastic loading to the elastic part of the total strain  $d\boldsymbol{\varepsilon}^{el}$  we get

$$d\boldsymbol{\sigma} = \mathbf{D}^{el}(d\boldsymbol{\varepsilon} - d\boldsymbol{\varepsilon}^{pl}). \quad (2.23)$$

where  $\mathbf{D}^{el}$  represents, keeping up with the plane strain conditions, the  $(4 \times 4)$  elastic stiffness matrix. Substituting for  $d\boldsymbol{\varepsilon}^{pl}$  from Eq. (2.17) into Eq. (2.23) gives

$$d\boldsymbol{\sigma} = \mathbf{D}^{el} \left( d\boldsymbol{\varepsilon} - d\lambda \frac{\partial G}{\partial \boldsymbol{\sigma}} \right). \quad (2.24)$$

After substituting for  $d\boldsymbol{\sigma}$  from Eq. (2.24) into the consistency condition Eq. (2.18) we get

$$\left(\frac{\partial F}{\partial \boldsymbol{\sigma}}\right)^\top \mathbf{D}^{el} \left( d\boldsymbol{\varepsilon} - d\lambda \frac{\partial G}{\partial \boldsymbol{\sigma}} \right) - Hd\lambda = 0. \quad (2.25)$$

Note that for elastic unloading ( $d\lambda = 0$ ,  $dF < 0$ ) the above equation reduces to

$$\left(\frac{\partial F}{\partial \boldsymbol{\sigma}}\right)^{\top} \mathbf{D}^{el} d\boldsymbol{\varepsilon} < 0. \quad (2.26)$$

Solving for  $d\lambda$  from Eq. (2.25) yields for plastic yielding

$$d\lambda = \frac{\left(\frac{\partial F}{\partial \boldsymbol{\sigma}}\right)^{\top} \mathbf{D}^{el} d\boldsymbol{\varepsilon}}{H + \left(\frac{\partial F}{\partial \boldsymbol{\sigma}}\right)^{\top} \mathbf{D}^{el} \left(\frac{\partial G}{\partial \boldsymbol{\sigma}}\right)} \geq 0. \quad (2.27)$$

Suppose for simplicity that  $F = G$  (associated flow rule) and  $H = 0$  (perfect plasticity). Since in such a case  $\left(\frac{\partial F}{\partial \boldsymbol{\sigma}}\right)^{\top} \mathbf{D}^{el} \left(\frac{\partial F}{\partial \boldsymbol{\sigma}}\right) > 0$  ( $\mathbf{D}^{el}$  is positive definite), Eq. (2.27) implies

$$\left(\frac{\partial F}{\partial \boldsymbol{\sigma}}\right)^{\top} \mathbf{D}^{el} d\boldsymbol{\varepsilon} \geq 0. \quad (2.28)$$

In view of Eqs. (2.26) and (2.28) we may now postulate the following *loading criterion*:

$$\left(\frac{\partial F}{\partial \boldsymbol{\sigma}}\right)^{\top} \mathbf{D}^{el} d\boldsymbol{\varepsilon} \begin{cases} > 0 & \text{plastic loading } (d\lambda > 0), \\ = 0 & \text{neutral loading } (d\lambda = 0), \\ < 0 & \text{elastic unloading } (d\lambda < 0). \end{cases} \quad (2.29)$$

When deriving Eq. (2.28) we essentially assumed that the denominator is positive. However, if it is negative then conditions (2.26) and (2.27), if satisfied, suggest two different solutions for the same strain increment  $d\boldsymbol{\varepsilon}$ . It can be concluded that the plastic multiplier is uniquely determined from the consistency condition (2.25) provided, see also [17](Chapter 20) for more details,

$$H + \left(\frac{\partial F}{\partial \boldsymbol{\sigma}}\right)^{\top} \mathbf{D}^{el} \left(\frac{\partial G}{\partial \boldsymbol{\sigma}}\right) \geq 0. \quad (2.30)$$

To complete the derivation of the tangent stiffness matrix we substitute for  $d\lambda$  from Eq. (2.27) back into Eq. (2.23) to get

$$d\boldsymbol{\sigma} = \mathbf{D}^{el} \left[ \mathbf{I} - \frac{\left(\frac{\partial G}{\partial \boldsymbol{\sigma}}\right) \left(\frac{\partial F}{\partial \boldsymbol{\sigma}}\right)^{\top} \mathbf{D}^{el}}{H + \left(\frac{\partial F}{\partial \boldsymbol{\sigma}}\right)^{\top} \mathbf{D}^{el} \left(\frac{\partial G}{\partial \boldsymbol{\sigma}}\right)} \right] d\boldsymbol{\varepsilon}. \quad (2.31)$$

Eq. (2.31) represents an explicit expansion which determines the stress change in terms of strain change with the instantaneous (elasto-plastic) tangent stiffness matrix  $\mathbf{D}^{ep}$  written

as

$$d\boldsymbol{\sigma} = \mathbf{D}^{ep} d\boldsymbol{\varepsilon} \quad (2.32)$$

$$\mathbf{D}^{ep} = \mathbf{D}^{el} - \frac{\mathbf{D}^{el} \left( \frac{\partial G}{\partial \boldsymbol{\sigma}} \right) \left( \frac{\partial F}{\partial \boldsymbol{\sigma}} \right)^\top \mathbf{D}^{el}}{H + \left( \frac{\partial F}{\partial \boldsymbol{\sigma}} \right)^\top \mathbf{D}^{el} \left( \frac{\partial G}{\partial \boldsymbol{\sigma}} \right)} = \mathbf{D}^{el} - \frac{\mathbf{D}^{el} \mathbf{n}_g \mathbf{n}^\top \mathbf{D}^{el}}{H + \mathbf{n}^\top \mathbf{D}^{el} \mathbf{n}_g}, \quad (2.33)$$

where

$$\mathbf{n} = \frac{\partial F}{\partial \boldsymbol{\sigma}}, \quad \mathbf{n}_g = \frac{\partial G}{\partial \boldsymbol{\sigma}}, \quad (2.34)$$

represent normals to the yield and potential surfaces in the stress space, respectively.

### Algorithmic tangent stiffness matrix

It has been confirmed that the use of the elasto-plastic stiffness matrix given by Eq. (2.33) spoils the quadratic convergence of the Newton-Raphson iterative solver. Simo and Taylor [33] showed that in order to cure this, the elasto-plastic stiffness matrix must be consistent with the algorithmic procedure used for the stress update. Thus, following the standard predictor-corrector stress update procedure [33, 27, 37, 38, to cite a few] we write the incremental form of the constitutive equation follows

$$\boldsymbol{\sigma}^{i+1} - \boldsymbol{\sigma}^i = \mathbf{D}^{el} (\boldsymbol{\varepsilon}^{i+1} - \boldsymbol{\varepsilon}^i) - \mathbf{D}^{el} (\lambda^{i+1} - \lambda^i) \mathbf{n}_g^{i+1}, \quad (2.35)$$

Taking the time derivative of Eq. (2.35) yields

$$d\boldsymbol{\sigma} = \mathbf{D}^{el} d\boldsymbol{\varepsilon} - d\lambda \mathbf{D}^{el} \mathbf{n}_g - \Delta \lambda \mathbf{D}^{el} d\mathbf{n}_g, \quad (2.36)$$

with

$$d\mathbf{n}_g = \frac{\partial \mathbf{n}_g}{\partial \boldsymbol{\sigma}} d\boldsymbol{\sigma}. \quad (2.37)$$

Introducing Eq. (2.37) into Eq. (2.36) after some manipulation gives

$$(\mathbf{D}^{el})^{-1} d\boldsymbol{\sigma} = d\boldsymbol{\varepsilon} - d\lambda \mathbf{n}_g - \Delta \lambda \frac{\partial \mathbf{n}_g}{\partial \boldsymbol{\sigma}} d\boldsymbol{\sigma}, \quad (2.38)$$

$$\left[ (\mathbf{D}^{el})^{-1} + \Delta \lambda \frac{\partial \mathbf{n}_g}{\partial \boldsymbol{\sigma}} \right] d\boldsymbol{\sigma} = d\boldsymbol{\varepsilon} - d\lambda \mathbf{n}_g, \quad (2.39)$$

$$d\boldsymbol{\sigma} = \underbrace{\left[ (\mathbf{D}^{el})^{-1} + \Delta \lambda \frac{\partial \mathbf{n}_g}{\partial \boldsymbol{\sigma}} \right]^{-1}}_{\mathcal{D}} (d\boldsymbol{\varepsilon} - d\lambda \mathbf{n}_g), \quad (2.40)$$

$$\mathcal{D} = \left[ (\mathbf{D}^{el})^{-1} + \Delta \lambda \frac{\partial \mathbf{n}_g}{\partial \boldsymbol{\sigma}} \right]^{-1}. \quad (2.41)$$



Writing the consistency condition Eq. (2.14) in the rate form

$$dF = \left( \frac{\partial F}{\partial \boldsymbol{\sigma}} \right)^\top d\boldsymbol{\sigma} - H d\lambda = 0, \quad (2.42)$$

provides

$$d\lambda = \frac{1}{H} \underbrace{\left( \frac{\partial F}{\partial \boldsymbol{\sigma}} \right)^\top}_{\mathbf{n}^\top} d\boldsymbol{\sigma} = \frac{\mathbf{n}^\top d\boldsymbol{\sigma}}{H}, \quad (2.43)$$

With the help of Eq. (2.43) Eq. (2.40) can be inverted to get

$$d\boldsymbol{\varepsilon} = \left[ \mathcal{D}^{-1} + \frac{\mathbf{n}_g \mathbf{n}^\top}{H} \right] d\boldsymbol{\sigma}. \quad (2.44)$$

Finally, applying the Sherman-Morrison formula written in its general form as

$$\mathbf{B} = \mathbf{I} + \mathbf{r} \mathbf{N}^\top, \quad (2.45)$$

$$\mathbf{B}^{-1} = \mathbf{I} - \frac{\mathbf{r} \mathbf{N}^\top}{1 + \mathbf{r}^\top \mathbf{N}}, \quad (2.46)$$

to Eq. (2.44) results in the desired algorithmic tangent stiffness matrix

$$d\boldsymbol{\sigma} = \underbrace{\left[ \mathcal{D} - \frac{\mathcal{D} \mathbf{n}_g \mathbf{n}^\top \mathcal{D}}{H + \mathbf{n}^\top \mathcal{D} \mathbf{n}_g} \right]}_{\mathcal{D}^{cons}} d\boldsymbol{\varepsilon}, \quad (2.47)$$

$$\mathcal{D}^{cons} = \mathcal{D} - \frac{\mathcal{D} \mathbf{n}_g \mathbf{n}^\top \mathcal{D}}{H + \mathbf{n}^\top \mathcal{D} \mathbf{n}_g}. \quad (2.48)$$

Note that using the above form of the instantaneous elasto-plastic stiffness matrix ( $\mathcal{D}^{cons}$ ) instead of  $\mathbf{D}^{ep}$  in the iterative solver maintains the theoretically proved quadratic convergence of the Newton-Raphson method.

### 2.3.4 Drucker-Prager model

If the results of laboratory tests are plotted in terms effective rather than total stress the failure criterion becomes dependent on the hydrostatic or mean stress. Such dependence can be accounted for by using the Drucker-Prager plasticity model.

#### Yield surface

The Drucker-Prager model can be thought of as an extension of the von Mises model by including the first invariant of the stress tensor (mean stress) into the formulation of the yield surface. The Drucker-Prager yield surface then plots as a cylindrical cone in the principal stress space. Corresponding projections into deviatoric and meridian planes

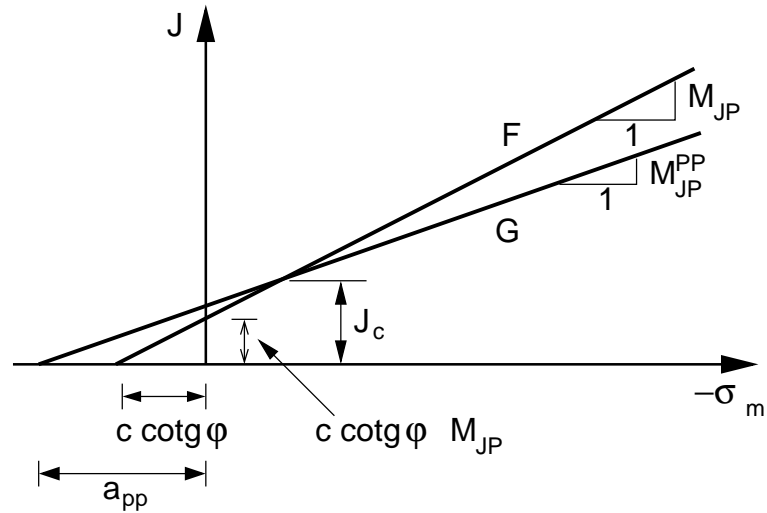


Figure 2.5: Projections of the yield function and plastic potential functions of Drucker-Prager model into meridian plane.

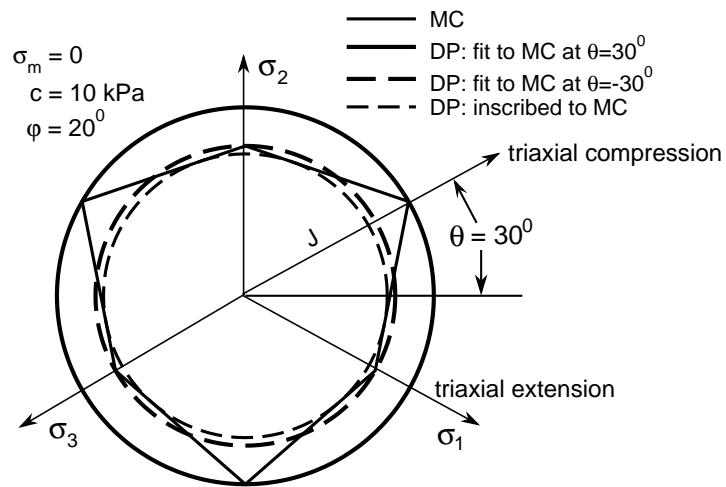


Figure 2.6: Drucker-Prager and Mohr Coulomb yield surfaces in the deviatoric plane.

appear in Figs 2.5 and 2.6. Following [29] the Drucker-Prager yield criterion then assumes the form

$$F(\sigma, \kappa) = J + (\sigma_m - c(\kappa_1) \cot \varphi(\kappa_2)) M_{JP}(\varphi(\kappa_2)) = 0, \quad (2.49)$$

where  $J$  and  $\sigma_m$  are given by Eqs. (2.8) and (2.7), respectively. Recall that vector  $\kappa = (\kappa_1, \kappa_2)^\top$  stores the hardening/softening parameters.

As with the von Mises and Tresca models the radius of the Drucker-Prager circle in the deviatoric plane can be defined by matching the Drucker-Prager and Mohr-Coulomb models at a particular value of Lode's angle  $\theta$ . This is illustrated in Fig 2.6 where the irregular hexagon of the Mohr-Coulomb surfaces is compared with the circular shape of the Drucker-Prager surface in the deviatoric plane. Three alternative Drucker-Prager circles are shown. Assuming that both surfaces match at  $\theta = 30^\circ$  (triaxial compression) we arrive at the Drucker-Prager circle circumscribed to the Mohr-Coulomb function (green circle). The corresponding value of  $M_{JP}$  reads

$$M_{JP}^{\theta=+30^\circ} = \frac{2\sqrt{3} \sin \varphi}{3 - \sin \varphi}. \quad (2.50)$$

If we desire that the Drucker-Prager circle touches the Mohr-Coulomb hexagon at  $\theta = -30^\circ$  (triaxial extension - blue circle) we set the value of  $M_{JP}$  to

$$M_{JP}^{\theta=-30^\circ} = \frac{2\sqrt{3} \sin \varphi}{3 + \sin \varphi}. \quad (2.51)$$

Finally, the inscribed circle is found, see [29] for more details, when setting

$$M_{JP}^{ins} = \frac{\sin \varphi}{\cos \theta^{ins} - \frac{\sin \theta^{ins} \sin \varphi}{\sqrt{3}}}, \quad (2.52)$$

with

$$\theta^{ins} = \arctan \frac{\sin \varphi}{\sqrt{3}}. \quad (2.53)$$

The model is completed by adopting a plastic potential function of the form

$$G = J + [\sigma_m - a_{pp}] M_{JP}^{PP} = 0, \quad (2.54)$$

where  $a_{pp}$  follows from Fig. 2.5 when matching  $F$  and  $G$  for the current value of stress  $\sigma$ . This gives

$$a_{pp} = -\sigma_m + (\sigma_m^c - c \cot \varphi) \frac{M_{JP}}{M_{JP}^{PP}}.$$

After substituting  $a_{pp}$  into Eq. (2.16) the plastic potential can be written in the form

$$G = J + \left[ \sigma_m - \sigma_m^c + (\sigma_m^c - c \cot \varphi) \frac{M_{JP}}{M_{JP}^{PP}} \right] M_{JP}^{PP} = 0, \quad (2.55)$$

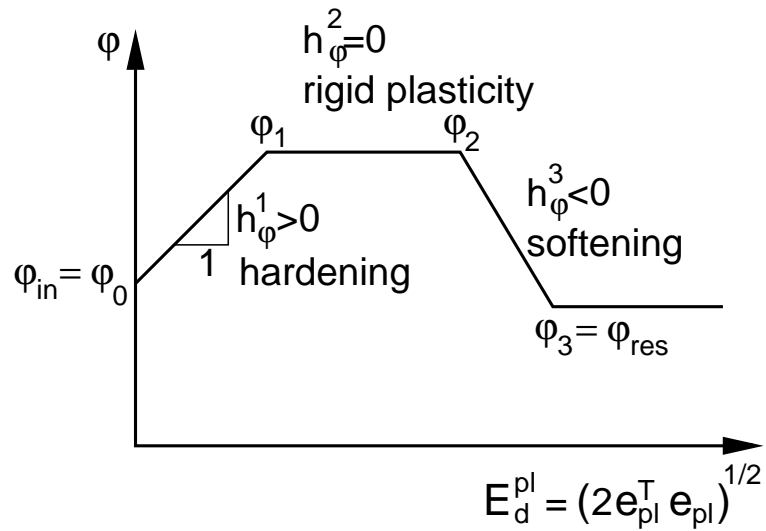
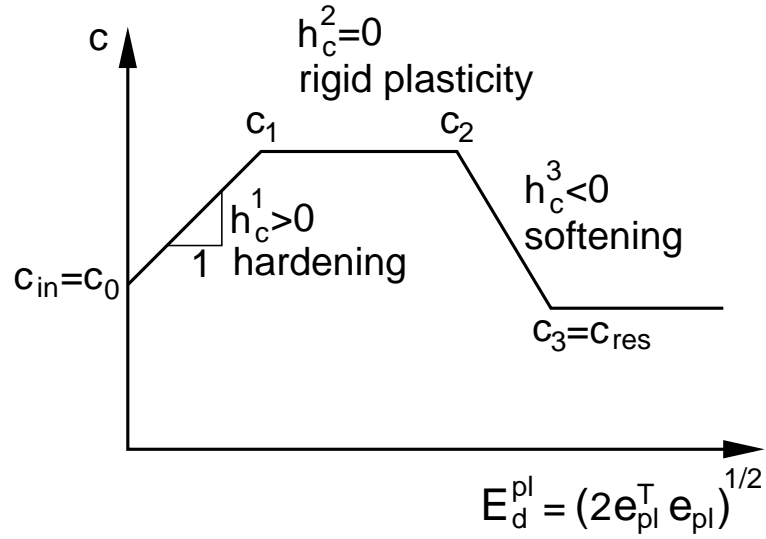


Figure 2.7: Multi-linear hardening/softening law.

where  $M_{JP}^{PP}$  is the gradient of the plastic potential function in  $J - \sigma_m$  space (see Fig 2.5). If  $M_{JP}^{PP} = M_{JP}$  the yield and plastic potential functions are the same and the model becomes associated.  $M_{JP}^{PP}$  can be related to the angle of dilation  $\psi$ , by substituting  $\psi$  for  $\varphi$  in Eqs. (2.50)-(2.52). As with the von Mises plasticity model we now proceed with the derivation of the hardening/softening modulus  $H$ . To that end, consider the multi-linear form of the hardening/softening law for the cohesion  $c$  and the angle of internal friction  $\varphi$  plotted in Fig. 2.7. In Fig. 2.7  $c_{in}, \varphi_{in}$  and  $c_{res}, \varphi_{res}$  represent the initial and residual values of  $c$  and  $\varphi$ , respectively. Although the components of vector  $\kappa$  may differ for each of the two strength parameters, a single hardening parameter  $\kappa = \kappa_1 = \kappa_2 = E_d$  is assumed in the present formulation. See also Fig. 2.7 suggesting a multi-linear variation of  $c, \varphi$  as a function of deviatoric strain  $E_d$ . For further discussion, suppose that an  $n^{th}$  interval in Fig. 2.7 is active. The current strength parameters are then provided by

$$c = c^{n-1} + h_c^n \left( E_d^{pl} - (E_d^{pl})^{n-1} \right), \quad (2.56)$$

$$\varphi = \varphi^{n-1} + h_\varphi^n \left( E_d^{pl} - (E_d^{pl})^{n-1} \right), \quad (2.57)$$

where the current hardening/softening moduli  $h_c^n, h_\varphi^n$  follow from

$$h_c^n = \frac{c^n - c^{n-1}}{(E_d^{pl})^n - (E_d^{pl})^{n-1}}, \quad (2.58)$$

$$h_\varphi^n = \frac{\varphi^n - \varphi^{n-1}}{(E_d^{pl})^n - (E_d^{pl})^{n-1}}. \quad (2.59)$$

Referring to Fig. 2.7 and using Eq. (2.19) the hardening/softening modulus  $H$  assumes the form

$$H = -\frac{\partial F}{\partial c} \frac{dc}{dE_d^{pl}} \frac{dE_d^{pl}}{d\lambda} - \frac{\partial F}{\partial \varphi} \frac{d\varphi}{dE_d^{pl}} \frac{dE_d^{pl}}{d\lambda}, \quad (2.60)$$

where

$$\frac{\partial F}{\partial \varphi} = \frac{c}{\sin^2 \varphi} M_{JP} + (\sigma_m - c \cot \varphi) \frac{dM_{JP}}{d\varphi}, \quad (2.61)$$

$$\frac{dF}{dc} = -\cot \varphi M_{JP}, \quad (2.62)$$

$$\frac{dc}{d\kappa} = \frac{dc}{dE_d^{pl}} = h_c, \quad (2.63)$$

$$\frac{d\varphi}{d\kappa} = \frac{d\varphi}{dE_d^{pl}} = h_\varphi. \quad (2.64)$$

Derivatives of  $M_{JP}$  with respect to  $\varphi$  for selected values of  $\theta$  are

$$\frac{dM_{JP}^{ins}}{d\varphi} = \frac{3\sqrt{3}\cos\varphi}{(3 + \sin^2\varphi)^{\frac{3}{2}}}, \quad (2.65)$$

$$\frac{dM_{JP}^{\theta=-30^\circ}}{d\varphi} = \frac{6\sqrt{3}\cos\varphi}{(1 - \sin\varphi)^2}, \quad (2.66)$$

$$\frac{dM_{JP}^{\theta=+30^\circ}}{d\varphi} = \frac{6\sqrt{3}\cos\varphi}{(1 + \sin\varphi)^2}. \quad (2.67)$$

As in the previous section we accept the strain hardening approach and write

$$d\boldsymbol{\varepsilon}^{pl} = d\lambda \frac{\partial G}{\partial \boldsymbol{\sigma}} = d\lambda \frac{1}{2J} \mathbf{P}\boldsymbol{\sigma}, \quad (2.68)$$

$$d\kappa = dE_d^{pl} = \sqrt{2(\boldsymbol{\varepsilon}^{pl})^\top \mathbf{Q}\mathbf{P}\mathbf{Q}\boldsymbol{\varepsilon}^{pl}} = d\lambda \Rightarrow \frac{dE_d^{pl}}{d\lambda} = 1. \quad (2.69)$$

Finally, substitution of Eq. (2.61) - (2.69) back into Eq. (2.60) readily provides the searched form of the hardening/softening modulus as

$$H = h_c \cot\varphi M_{JP} - h_\varphi \left[ \frac{c}{\sin^2\varphi} M_{JP} + (\sigma_m - c \cot\varphi) \frac{dM_{JP}}{d\varphi} \right]. \quad (2.70)$$

### Tangent stiffness matrix

The instantaneous tangent stiffness matrix follows from Eqs. (2.33) or (2.48). The partial derivatives of the yield function and plastic potential function with respect to stress can be found using the chain rule

$$\mathbf{n} = \frac{\partial F}{\partial \boldsymbol{\sigma}} = \frac{\partial F}{\partial \sigma_m} \frac{\partial \sigma_m}{\partial \boldsymbol{\sigma}} + \frac{\partial F}{\partial J} \frac{\partial J}{\partial \boldsymbol{\sigma}}, \quad (2.71)$$

$$\mathbf{n}_g = \frac{\partial G}{\partial \boldsymbol{\sigma}} = \frac{\partial G}{\partial \sigma_m} \frac{\partial \sigma_m}{\partial \boldsymbol{\sigma}} + \frac{\partial G}{\partial J} \frac{\partial J}{\partial \boldsymbol{\sigma}}. \quad (2.72)$$

Recall that vectors  $\mathbf{n}$  and  $\mathbf{n}_g$  represent normals to the yield and plastic potential functions in the stress space, respectively. From Eq. (2.49) and (2.55) it is easy to show that

$$\frac{\partial F}{\partial \sigma_m} = M_{JP}, \quad \frac{\partial G}{\partial \sigma_m} = M_{JP}^{PP}, \quad \frac{\partial F}{\partial J} = \frac{\partial G}{\partial J} = 1.$$

The values of  $\partial \sigma_m / \partial \boldsymbol{\sigma}$  and  $\partial J / \partial \boldsymbol{\sigma}$  are model independent and are given by

$$\frac{\partial \sigma_m}{\partial \boldsymbol{\sigma}} = \mathbf{m}, \quad (2.73)$$

$$\frac{\partial J}{\partial \boldsymbol{\sigma}} = \frac{\partial (\frac{1}{2} \boldsymbol{\sigma}^\top \mathbf{P}\boldsymbol{\sigma})^{\frac{1}{2}}}{\partial \boldsymbol{\sigma}} = \frac{1}{2J} \mathbf{P}\boldsymbol{\sigma}. \quad (2.74)$$

With the above expressions we finally get

$$\frac{\partial F}{\partial \boldsymbol{\sigma}} = \frac{1}{2J} \mathbf{P} \boldsymbol{\sigma} + M_{JP} \mathbf{m}, \quad (2.75)$$

$$\frac{\partial G}{\partial \boldsymbol{\sigma}} = \frac{1}{2J} \mathbf{P} \boldsymbol{\sigma} + M_{JP}^{PP} \mathbf{m}. \quad (2.76)$$

In addition, the second derivative of  $\mathbf{n}_g$  needed to determine the algorithmic tangent matrix  $\mathcal{D}^{cons}$  is provided by

$$\frac{\partial \mathbf{n}_g}{\partial \boldsymbol{\sigma}} = \left(\frac{3}{2}\right)^{1/2} \frac{\boldsymbol{\sigma}^T \mathbf{P} \boldsymbol{\sigma} \mathbf{P} - \mathbf{P} \boldsymbol{\sigma} \boldsymbol{\sigma}^T \mathbf{P}}{(\boldsymbol{\sigma}^T \mathbf{P} \boldsymbol{\sigma})^{3/2}}. \quad (2.77)$$

### 2.3.5 Modified Mohr-Coulomb model

As shown in the previous section the Drucker-Prager model plots as a circle in the deviatoric plane, thus it is invariant with respect to Lode's angle  $\theta$ . Although the assumption about a smoothed yield surface in the deviatoric plane has been confirmed experimentally, the shape of the yield surface shows variation with respect to the third invariant. The well known Mohr-Coulomb model is probably the most widely accepted model that shows variation with  $\theta$  in the deviatoric plane. Recall that in the principal stress space the Mohr-Coulomb model plots as a hexagonal cone. However, as evident from Fig. 2.6, it suffers from the same drawback as the Tresca model as it experiences corners. To bring the modeling of plastic behavior of soils closer to conventional soil mechanics and yet avoid corners of the yield and potential surfaces we introduce a "Modified" Mohr-Coulomb model having a smoothed surface with a shape somewhere between that of the hexagons and circles. Such a surface is also promoted in the literature as it agrees better experimental results.

#### Yield surface

The yield function is constructed in such a way that it allows the present yield surface and the one that corresponds to the Mohr-Coulomb law to be matched at all corners of the yield surface in the deviatoric plane. Several examples are plotted in Fig. 2.8. The yield function that corresponds to smooth surfaces plotted in Fig. 2.8 is defined as follows

$$F = J + (\sigma_m - c(\kappa_1) \cot \varphi(\kappa_2))g(\theta, \varphi(\kappa_2)) = 0, \quad (2.78)$$

where the rounded triangular shape of the yield surface in the deviatoric plane is described by (see also van Eekelen [9] for similar formulation)

$$g(\theta) = X (Y_1 + Y_2 \sin 3\theta)^{-Z}, \quad (2.79)$$

where  $\theta$  is Lode's angle, Eq. (2.9). Parameters  $X, Y_1, Y_2, Z$  are selected such to give a perfect fit to all corners of the Mohr-Coulomb hexagon. These are

$$X = 2^{Z+1} \sqrt{3} \sin \varphi, \quad (2.80)$$

$$Y_1 = (3 + \sin \varphi)^{\frac{1}{Z}} + (3 - \sin \varphi)^{\frac{1}{Z}}, \quad (2.81)$$

$$Y_2 = (3 - \sin \varphi)^{\frac{1}{Z}} - (3 + \sin \varphi)^{\frac{1}{Z}}. \quad (2.82)$$

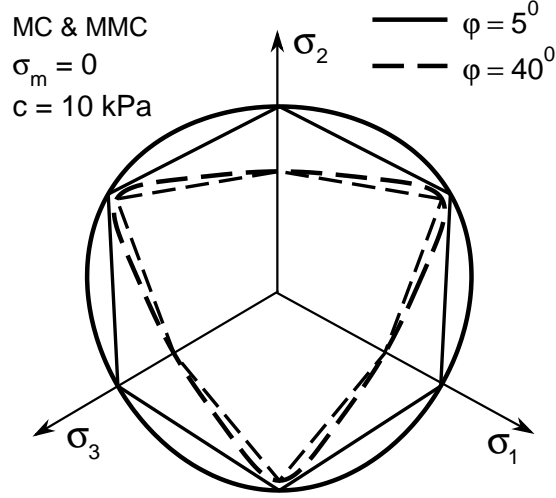


Figure 2.8: Standard and Modified Mohr Coulomb yield surfaces in the deviatoric plane.

Some restrictions have to be applied on exponent  $Z$  to ensure convexity of the yield surface.

The plastic potential of the Modified Mohr-Coulomb model is proposed the same as for the Drucker-Prager model (see Fig. 2.9). It reads

$$G = J + \left[ \sigma_m - \sigma_m^c + (\sigma_m^c - c \cot \varphi) \frac{g(\theta, \varphi)}{M_{JP}^{PP}} \right] M_{JP}^{PP} = 0, \quad (2.83)$$

with  $M_{JP}^{PP}$  being a constant. Therefore, the non-associated plasticity is assumed a priori. The use of a circular shape for the plastic potential in the deviatoric plane is motivated by experimental results presented by Kim&Lade [18] that suggest the plastic potential is close to a Drucker-Prager contour, at least at low stress levels. The use of a shape of plastic potential different from that of the yield surface is also advocated in [29] to guarantee realistic values of Lode's angle at failure  $\theta_f$  for problems involving plane strain deformation.

### Tangent stiffness matrix

The instantaneous tangent stiffness matrix can again be obtained by Eqs. (2.33) or (2.48). The required normals to the yield and potential surfaces now become

$$\mathbf{n} = \frac{\partial F}{\partial \boldsymbol{\sigma}} = \frac{\partial F}{\partial \sigma_m} \frac{\partial \sigma_m}{\partial \boldsymbol{\sigma}} + \frac{\partial F}{\partial J} \frac{\partial J}{\partial \boldsymbol{\sigma}} + \frac{\partial F}{\partial \theta} \frac{\partial \theta}{\partial \boldsymbol{\sigma}}, \quad (2.84)$$

$$\mathbf{n}_g = \frac{\partial G}{\partial \boldsymbol{\sigma}} = \frac{\partial G}{\partial \sigma_m} \frac{\partial \sigma_m}{\partial \boldsymbol{\sigma}} + \frac{\partial G}{\partial J} \frac{\partial J}{\partial \boldsymbol{\sigma}}. \quad (2.85)$$



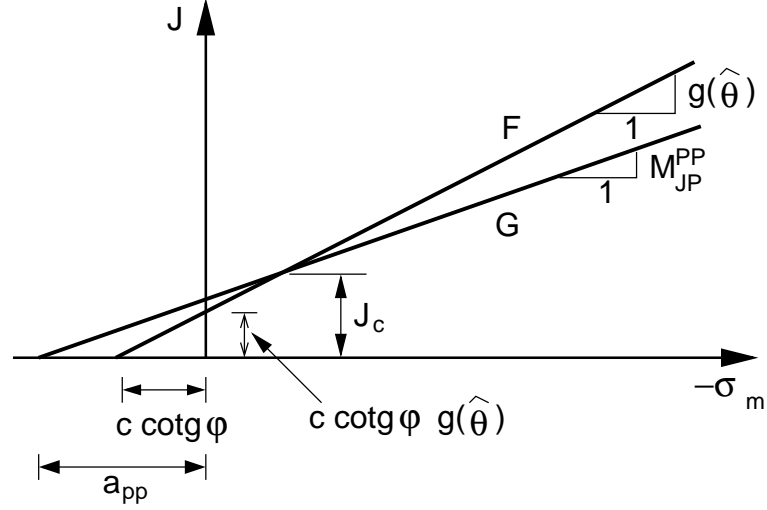


Figure 2.9: Relationship between the yield function and plastic potential in the modified Mohr-Coulomb model.

Referring to Section 2.3.4 we immediately see that

$$\frac{\partial F}{\partial J} \frac{\partial J}{\partial \boldsymbol{\sigma}} = \frac{\partial G}{\partial J} \frac{\partial J}{\partial \boldsymbol{\sigma}} = \frac{1}{2J} \mathbf{P} \boldsymbol{\sigma}, \quad \frac{\partial F}{\partial \sigma_m} \frac{\partial \sigma_m}{\partial \boldsymbol{\sigma}} = g(\theta) \mathbf{m}, \quad \frac{\partial G}{\partial \sigma_m} \frac{\partial \sigma_m}{\partial \boldsymbol{\sigma}} = M_{JP}^{PP} \mathbf{m}.$$

To complete the formulation it remains to determine values of  $\partial F/\partial \theta$  and  $\partial \theta/\partial \boldsymbol{\sigma}$  in Eq. (2.84). In doing so, we first differentiate the yield Eq. (2.78) with respect to  $\theta$  to get

$$\begin{aligned} \frac{\partial F}{\partial \theta} &= (\sigma_m - c \cot \varphi) \frac{\partial g(\theta)}{\partial \theta}, \\ \frac{\partial g(\theta)}{\partial \theta} &= -XZ(Y_1 + Y_2 \sin 3\theta)^{-Z-1} 3Y_2 \cos 3\theta. \end{aligned} \quad (2.86)$$

The term  $\partial \theta/\partial \boldsymbol{\sigma}$  is again model independent and it receives the form

$$\begin{aligned} \frac{\partial \theta}{\partial \boldsymbol{\sigma}} &= \frac{1}{3 \cos(3\theta)} \frac{\partial \sin(3\theta)}{\partial \boldsymbol{\sigma}} = -\frac{\sqrt{3}}{2 \cos 3\theta} \frac{\partial}{\partial \boldsymbol{\sigma}} \left( \frac{I_{3s}}{J^3} \right), \\ &= \frac{\sqrt{3}}{2J^3 \cos 3\theta} \left( \frac{3I_{3s}}{J} \frac{\partial J}{\partial \boldsymbol{\sigma}} - \frac{\partial I_{3s}}{\partial \boldsymbol{\sigma}} \right). \end{aligned} \quad (2.87)$$

Assuming again the plane strain conditions the term  $\partial I_{3s}/\partial \boldsymbol{\sigma}$  attains, with the help of Eq. (2.10), the following form

$$\frac{\partial I_{3s}}{\partial \boldsymbol{\sigma}} = \hat{\mathbf{s}} = \left\{ \begin{array}{c} \frac{1}{3} [\sigma_{xy}^2 + 2s_{yy}s_{zz} - s_{xx}(s_{yy} + s_{zz})] \\ \frac{1}{3} [\sigma_{xy}^2 + 2s_{xx}s_{zz} - s_{yy}(s_{xx} + s_{zz})] \\ -2\sigma_{xy}s_{zz} \\ \frac{1}{3} [-2\sigma_{xy}^2 + 2s_{xx}s_{yy} - s_{zz}(s_{xx} + s_{yy})] \end{array} \right\}.$$

Employing the above expressions then allows the two vectors  $\mathbf{n}, \mathbf{n}_g$  in Eqs. (2.84) - (2.85) to be written as

$$\begin{aligned} \mathbf{n} &= \frac{1}{2J} \mathbf{P}\boldsymbol{\sigma} + g(\theta) \mathbf{m} - (\sigma_m - c \cot \varphi) XZ(Y_1 + Y_2 \sin 3\theta)^{-Z-1} Y_2 \times \\ &\quad \times \frac{3\sqrt{3}}{2J^3} \left( \frac{3I_{3s}}{2J^2} \mathbf{P}\boldsymbol{\sigma} - \hat{\mathbf{s}} \right), \end{aligned} \quad (2.88)$$

$$\mathbf{n}_g = \frac{1}{2J} \mathbf{P}\boldsymbol{\sigma} + M_{JP}^{PP} \mathbf{m}. \quad (2.89)$$

Finally, the hardening/softening modulus follows from Eq. (2.60). Individual terms are

$$\frac{\partial F}{\partial c} = -\frac{g(\theta, \varphi)}{\tan \varphi}, \quad (2.90)$$

$$\frac{\partial F}{\partial \varphi} = \frac{c}{\sin^2 \varphi} g(\theta, \varphi) + (\sigma_m - c \cot \varphi) \frac{\partial g(\theta, \varphi)}{\partial \varphi}. \quad (2.91)$$

The last term in Eq. (2.91) is provided by

$$\frac{\partial g(\theta, \varphi)}{\partial \varphi} = (Y_1 + Y_2 \sin 3\theta)^{-Z} \frac{dX}{d\varphi} - ZX(Y_1 + Y_2 \sin 3\theta)^{-Z-1} \left( \frac{dY_1}{d\varphi} + \frac{dY_1}{d\varphi} \sin 3\theta \right),$$

where

$$\begin{aligned} \frac{dX}{d\varphi} &= 2^{Z+1} \sqrt{3} \cos \varphi, \\ \frac{dY_1}{d\varphi} &= \frac{\cos \varphi}{Z} \left[ (3 + \sin \varphi)^{\frac{1-Z}{Z}} - (3 - \sin \varphi)^{\frac{1-Z}{Z}} \right], \\ \frac{dY_2}{d\varphi} &= -\frac{\cos \varphi}{Z} \left[ (3 - \sin \varphi)^{\frac{1-Z}{Z}} + (3 + \sin \varphi)^{\frac{1-Z}{Z}} \right]. \end{aligned}$$

Combining Eqs. (2.60), (2.90)-(2.91) gives the desired hardening/softening modulus  $H$  in the form

$$H = h_c \cot \varphi g(\theta, \varphi) - h_\varphi \left[ \frac{c}{\sin^2 \varphi} g(\theta, \varphi) + (\sigma_m - c \cot \varphi) \frac{\partial g(\theta, \varphi)}{\partial \varphi} \right]. \quad (2.92)$$

### 2.3.6 Implicit stress point algorithm for Drucker-Prager and Modified Mohr-Coulomb models

The robust fully implicit return mapping in the form implemented in program GEO FEM is presented here for the Drucker-Prager and modified Mohr-Coulomb constitutive models to transfer the initial trial stresses from an illegal space back to the yield surface.

### Drucker-Prager

For the assumed  $J_2$  class of plasticity models it becomes convenient to split the general stress and strain vectors into their volumetric and deviatoric parts. Accepting the plastic flow rule provided by Eq. (2.17) then yields the respective increments of plastic strain in the form

$$\Delta \varepsilon_v^{pl} = \Delta \lambda \frac{\partial G}{\partial \sigma_m} = \Delta \lambda M_{PP}(\sin \psi), \quad (2.93)$$

$$\Delta \mathbf{e}^{pl} = \Delta \lambda \frac{\partial G}{\partial \mathbf{s}} = \Delta \lambda \frac{\mathbf{Q}^{-1} \mathbf{s}}{2J}, \quad (2.94)$$

$$\Delta E_d^{pl} = \Delta \lambda \frac{\partial G}{\partial J} = \Delta \lambda, \quad (2.95)$$

which further allows writing the corresponding stresses at the end of the  $i + 1$  load increment as

$$\sigma_m^{i+1} = \sigma_m^{tr} - K M_{PP}(\sin \psi^{i+1}) \Delta \lambda, \quad (2.96)$$

$$\mathbf{s}^{i+1} = \mathbf{s}^{tr} - 2\mu \Delta \lambda \frac{\mathbf{s}^{i+1}}{2J^{i+1}} = \frac{\mathbf{s}^{tr}}{1 + \frac{\mu \Delta \lambda}{J^{i+1}}} = \mathbf{s}^{tr} \left( 1 - \frac{\mu \Delta \lambda}{J^{tr}} \right), \quad (2.97)$$

$$J^{i+1} = J^{tr} - \mu \Delta \lambda, \quad (2.98)$$

where  $\mu$  represents the elastic shear modulus to avoid confusion with the definition of the plastic potential function. The trial stresses are again found through a predictor step assuming an initially elastic response, recall Eqs. (3.44) and (3.45).

A detailed description of the integration algorithm leading to “correct” stress field for a given increment of the total strain  $\Delta \boldsymbol{\varepsilon}$  is outlined in Section 3.3. A rather concise form of this algorithm will be reviewed henceforth giving only the essential steps pertinent to the Drucker-Prager hardening/softening plasticity.

- Primary variables

$$\{\mathbf{a}\}^T = \{\Delta \lambda, c^{i+1}, \sin \varphi^{i+1}, \sin \psi^{i+1}\}. \quad (2.99)$$

- Residuals

$$\{\mathbf{r}\}^T = \{\mathcal{F}, \mathcal{C}, \Phi, \Psi\}, \quad (2.100)$$

where

$$\mathcal{F} = \overbrace{(J^{tr} - \mu \Delta \lambda)}^{J^{i+1}} + \overbrace{[(\sigma_m^{tr} - K M_{PP}(\sin \psi^{i+1}) \Delta \lambda) - c^{i+1} \cot \varphi^{i+1}] M_{JP}(\sin \varphi^{i+1})}^{\sigma_m^{i+1}}, \quad (2.101)$$

$$\mathcal{C} = c^{i+1} - \hat{c} = 0, \quad (2.102)$$

$$\Phi = \sin \varphi^{i+1} - \sin \hat{\varphi} = 0, \quad (2.102)$$

$$\Psi = \sin \psi^{i+1} - \sin \hat{\psi} = 0. \quad (2.103)$$

Variables  $\widehat{c}$ ,  $\widehat{\varphi}$  follow from Eqs. (2.56) and (2.57). The current value of the dilation angle  $\widehat{\psi}$  is found with the help of Rowe's dilation theory in triaxial compression

$$\sin \widehat{\psi} = \frac{\sin \varphi^{i+1} - \sin \varphi_{cv}}{1 - \sin \varphi^{i+1} \sin \varphi_{cv}}. \quad (2.104)$$

- Local Newton-Raphson method

$$\{\mathbf{a}^{i+1}\}_{k+1} = \{\mathbf{a}^{i+1}\}_k - [\mathbf{H}]^{-1} \{\mathbf{r}\}_k. \quad (2.105)$$

- Jacobian matrix  $[\mathbf{H}]$

$$[\mathbf{H}] = \begin{bmatrix} \frac{\partial J}{\partial \Delta \lambda} + \frac{\partial F}{\partial \sigma_m} \frac{\partial \sigma_m}{\partial \Delta \lambda} & \frac{\partial F}{\partial c} & \frac{\partial F}{\partial \sin \varphi} + \frac{\partial F}{\partial M_{JP}} \frac{\partial M_{JP}}{\partial \sin \varphi} & \frac{\partial F}{\partial M_{PP}} \frac{\partial M_{PP}}{\partial \sin \psi} \\ \frac{\partial C}{\partial \widehat{c}} \frac{\partial \widehat{c}}{\partial \Delta \lambda} & \frac{\partial C}{\partial c} & 0 & 0 \\ \frac{\partial \Phi}{\partial \sin \widehat{\varphi}} \frac{\partial \sin \widehat{\varphi}}{\partial \Delta \lambda} & 0 & \frac{\partial \Phi}{\partial \sin \varphi} & 0 \\ 0 & 0 & \frac{\partial \Psi}{\partial \sin \widehat{\psi}} \frac{\partial \sin \widehat{\psi}}{\partial \sin \varphi} & \frac{\partial \Psi}{\partial \sin \psi} \end{bmatrix}. \quad (2.106)$$

- Initial conditions

$$\{\mathbf{a}_0\}^T = \{0, c^i, \sin \varphi^i, \sin \psi^i\}, \quad (2.107)$$

$$\{\mathbf{r}_0\}^T = \{\mathbf{J}^{\text{tr}} + (\sigma_m^{\text{tr}} - c^i \cot \varphi^i) M_{JP}(\sin \varphi^i), 0, 0, 0\}. \quad (2.108)$$

### Apex problem

The above algorithm is applicable providing the trial stress when brought back to the yield surface in the direction of the plastic strain rate vector (following inclination of the boundary of  $K_\varepsilon$  cone) is found on the boundary of cone  $K_\sigma$  representing the admissible stress domain, Fig. 2.10(a). Such a condition is met for point 1 in Fig. 2.10(b) but violated when referring to point 2. In the latter case the standard stress point return algorithm locates the stress point on the boundary of dual cone (point 2' in Fig. 2.10(b)) thus violating the yield condition. Such a situation can be referred to as an "apex problem", since in this particular case the stress update is simply a return mapping to the apex (point 2' in Fig. 2.10(b)) so that

$$\boldsymbol{\sigma}^{i+1} = 3c^{i+1} \cot \varphi^{i+1} \mathbf{m}. \quad (2.109)$$

Note that the non-associated flow rule restricts the plastic strain increment to belong to the cone  $K_\varepsilon$ , see also [12]. The admissibility condition for plastic strain rates is therefore given by, recall Fig. 2.10(a),

$$\dot{\varepsilon}_v \geq M_{JP}^{PP} \dot{E}_d^{pl}. \quad (2.110)$$

In [12] the authors introduced a variational form of the flow rule to show through the concept of bi-potentials that the vector of plastic strain increments for the apex problem is indeed provided by

$$\Delta \boldsymbol{\varepsilon}^{pl} = (\mathbf{D}^{el})^{-1} (\boldsymbol{\sigma}^{tr} - 3c^{i+1} \cot \varphi^{i+1} \mathbf{m}), \quad (2.111)$$

under the condition

$$\frac{1}{G} M_{JP}^{PP} J^{tr} - \frac{1}{K} (\sigma_m^{tr} - c^n \cot \varphi^n) < 0, \quad (2.112)$$

where  $G, K$  are the elastic shear and bulk moduli. Note that Eq. (2.112) is essentially a linearized form of Eq. (2.110).

Assuming hardening/softening material models it remains to update the hardening/softening parameters  $c, \varphi$ . To that end, a fully implicit procedure similar to that applied for the regular part of the yield surface is proposed. Before proceeding, we recall that the strain hardening hypotheses is adopted with a single hardening/softening parameter  $\kappa$  such that

$$\dot{\kappa} = \dot{E}_d^{pl}. \quad (2.113)$$

Rewriting Eq. (2.113) in the incremental form yields the following nonlinear equation

$$\mathcal{E} = \Delta E_d^{pl} - \overbrace{[2(\Delta \boldsymbol{\varepsilon}^{pl})^\top \mathbf{QPQ} \Delta \boldsymbol{\varepsilon}^{pl}]^{1/2}}^{\Delta \widehat{E}_d^{pl}} = 0, \quad (2.114)$$

to be solved simultaneously with Eqs. 2.101 and (2.102). Note that the plastic strain increment given by Eq. (2.111) is a function of the current strength parameters

$$\Delta \boldsymbol{\varepsilon}^{pl} = \Delta \boldsymbol{\varepsilon}^{pl}(c^{i+1}, \varphi^{i+1}).$$

In analogy with the return mapping proposed for the regular part of the yield surface the present nonlinear system of equations is solved again with the help of the generalized Newton-Raphson method, Eq. (2.105). To that end we define:

- Primary variables

$$\{\mathbf{a}\}^\top = \{\Delta E_d^{pl}, c^{i+1}, \sin \varphi^{i+1}\}. \quad (2.115)$$

- Residuals

$$\{\mathbf{r}\}^\top = \{\mathcal{E}, \mathcal{C}, \Phi\}. \quad (2.116)$$

- Jacobian matrix  $[\mathbf{H}]$

$$[\mathbf{H}] = \begin{bmatrix} \frac{\partial E}{\partial \Delta E_d^{pl}} & \left\{ \frac{\partial E}{\partial \Delta \boldsymbol{\varepsilon}^{pl}} \right\}^\top \left\{ \frac{\partial \Delta \boldsymbol{\varepsilon}^{pl}}{\partial c} \right\} & \left\{ \frac{\partial E}{\partial \Delta \boldsymbol{\varepsilon}^{pl}} \right\}^\top \left\{ \frac{\partial \Delta \boldsymbol{\varepsilon}^{pl}}{\partial \sin \varphi} \right\} \\ \frac{\partial \mathcal{C}}{\partial \Delta E_d^{pl}} = \frac{\partial \mathcal{C}}{\partial \Delta \lambda} & \frac{\partial \mathcal{C}}{\partial c} & 0 \\ \frac{\partial \Phi}{\partial \Delta E_d^{pl}} = \frac{\partial \Phi}{\partial \Delta \lambda} & 0 & \frac{\partial \Phi}{\partial \sin \varphi} \end{bmatrix}. \quad (2.117)$$

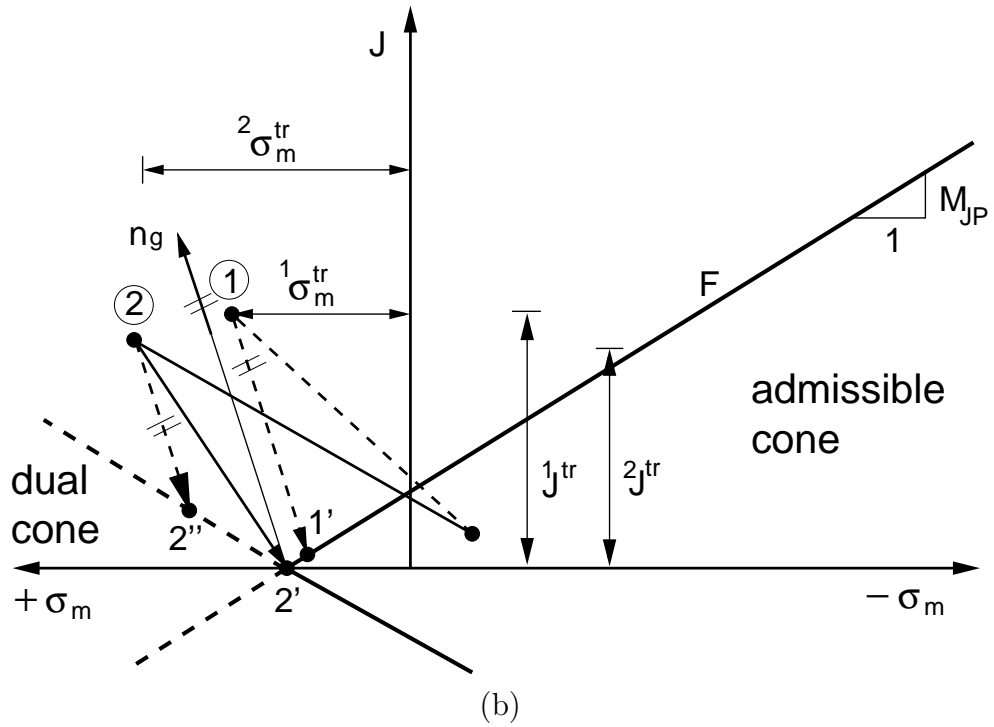
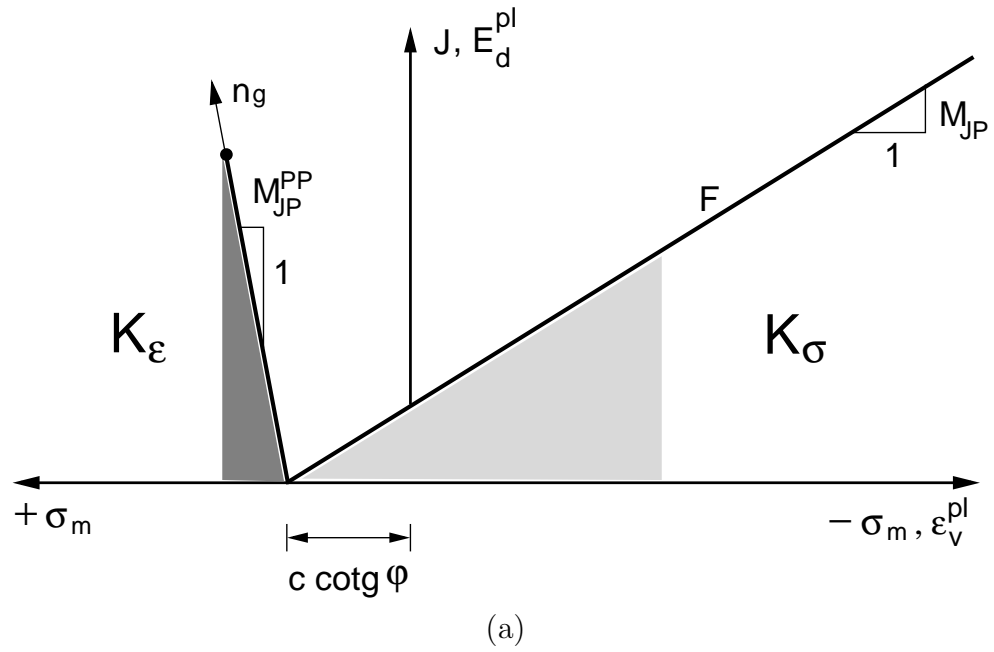


Figure 2.10: Apex problem: (a) Admissible regions for stresses and plastic strain rates, (b) Regular and singular return.

- Initial conditions

$$\{\mathbf{a}_0\}^T = \{0, c^i, \sin \varphi^i\}, \quad (2.118)$$

$$\{\mathbf{r}_0\}^T = \{[2(\Delta \boldsymbol{\varepsilon}^{pl})^T(c^i, \varphi^i) \mathbf{Q} \mathbf{P} \mathbf{Q} \Delta \boldsymbol{\varepsilon}^{pl}(c^i, \varphi^i)]^{1/2}, 0, 0\}. \quad (2.119)$$

### Modified Mohr-Coulomb

The integration algorithm for the Modified Mohr-Coulomb model follows the same steps as outlined in the previous section. The only difference is related to the definition of function  $F$  introduced in Eq. (2.78), so that only the derivatives filling the matrix  $[\mathbf{H}]$  in Eq. (2.107) need to be modified. In particular, the matrix element  $H_{11}$  receives in general the form

$$H_{11} = \frac{\partial J}{\partial \Delta \lambda} + \frac{\partial F}{\partial \sigma_m} \frac{\partial \sigma_m}{\partial \Delta \lambda} + \frac{\partial F}{\partial g} \frac{\partial g}{\partial \sin 3\theta} \frac{\partial \sin 3\theta}{\partial \Delta \lambda}, \quad (2.120)$$

where the term  $\frac{\partial \sin 3\theta}{\partial \Delta \lambda}$  is given by

$$\frac{\partial \sin 3\theta}{\partial \Delta \lambda} = \frac{\partial \sin 3\theta}{\partial J} \frac{\partial J}{\partial \Delta \lambda} + \frac{\partial \sin 3\theta}{\partial I_{3s}} \left\{ \frac{\partial I_{3s}}{\partial \mathbf{s}} \right\}^T \left\{ \frac{\partial \mathbf{s}}{\partial \Delta \lambda} \right\}. \quad (2.121)$$

However, it can be shown that the last equation vanishes owing to the assumption of a circular shape of plastic potential in the deviatoric plane so that no modification to Eq. (2.107) is needed. The same applies to the apex problem rendering the indicator condition the same as given by Eq. (2.112)

### 2.3.7 Mohr-Coulomb model

The Mohr-Coulomb failure criterion is perhaps the most well-known and understood soil failure model in geotechnical engineering, being the main model taught in undergraduate courses. The model is very simple and unites three elementary concepts. These are the ideas of plane strain transformation equations (including the definition of principal stresses), Mohr's circle and Coulomb's failure criterion. These three concepts are developed below and then united to derive the Mohr-Coulomb failure criterion.

#### Plane strain, principal stresses and the transformation equations

Consider a small three dimensional square element that lies inside a stressed body. The stresses acting on the element could be represented by those shown in Fig. 2.3.7. The stresses comprise of ones normal to and ones parallel to the faces of the element. These are known as *normal* and *shear stresses* respectively. The element has three spacial dimensions with stresses acting on all six faces but under certain conditions one of the principal stresses acting on two of the faces is much smaller than the others. This situation can arise when a stress element is located on the surface of a stressed body such as a shaft placed under torque loading or on the surface of a thin walled structure such as a balloon. In this case the small principal stress can be neglected and hence the problem becomes one in

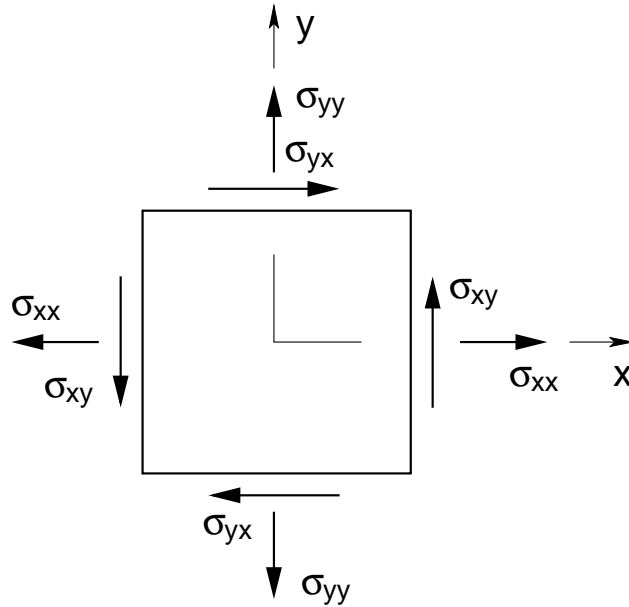


Figure 2.11: Small element under plane strain conditions

2-D. Hence the element as shown in Fig. 2.3.7 can be considered to have stresses acting on only the four surfaces shown. It should however be remembered that the element remains a three dimensional entity but that the out-of-plane stresses are neglected, Fig. 2.3.7. These types of conditions, already introduced in Section 1, are known as plane strain conditions and are used again as an assumption throughout this section to simplify the calculations. Thus, for the remainder of this discussion, the depth of the element (into the page) is assumed to be unity. Now consider a plane through the element at an angle of  $\alpha$  with the vertical. This plane cuts the element into two segments, the left hand of which is shown in Fig. 2.12. The stresses on the diagonal face are now considered to be resolved into a normal stress  $\sigma_\alpha$  and a shear stress  $\tau_\alpha$  as shown in Fig. 2.12. If the length of the diagonal side is assumed to be  $A$ , then the lengths of the other two sides of the element are  $A \cos \alpha$  and  $A \sin \alpha$  as shown. Note that because the depth of the element is unity, these are also the areas of the element faces. By writing the basic force equilibrium equations in the  $x$  and  $y$  directions and simultaneously solving for  $\sigma_\alpha$  and  $\tau_\alpha$  one obtains the transformation equations for plane stress

$$\sigma_\alpha = \frac{\sigma_{xx} + \sigma_{yy}}{2} + \frac{\sigma_{xx} - \sigma_{yy}}{2} \cos 2\alpha + \sigma_{xy} \sin 2\alpha, \quad (2.122)$$

$$\tau_\alpha = -\frac{\sigma_{xx} - \sigma_{yy}}{2} \sin 2\alpha + \sigma_{xy} \cos 2\alpha. \quad (2.123)$$

Equations (2.122) and (2.123) allow the calculation of the stresses on the inclined diagonal plane on the stress element. Now for any original stress state in the element in Fig. 2.3.7 two values of  $\alpha$  can be chosen such that the shear stress  $\tau_\alpha$  is equal to zero. In this orientation the normal stresses  $\sigma_\alpha$  are at their respective maxima and minima. These stresses are defined as the major  $\sigma_1$  and minor  $\sigma_3$  principal stresses respectively. An



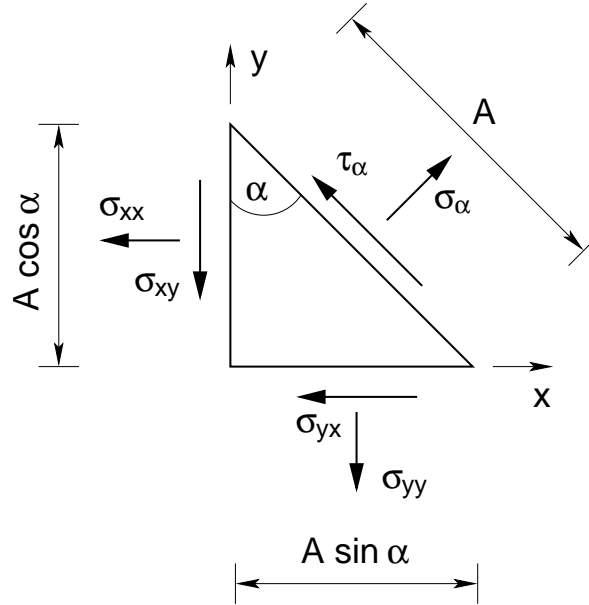


Figure 2.12: Sector of element

implicit characteristic of Eqs. (2.122) and (2.123) is that the principal stresses will always lie orthogonally to each other. The principal stresses are therefore nothing more than the maximum and minimum normal stresses inside a stressed body. The orientation of the principal stresses can be related to the angle  $\alpha$  by Eq. (2.122). If one differentiates this equation with respect to  $\alpha$  and sets it equal to zero in the normal fashion the orientation of the principal stresses can easily be found.

### Mohr's circle for plane stress

In 1882 Otto Mohr devised a useful graphical technique for showing how the normal and shear stresses vary in a body with respect to the angle  $\alpha$ . The technique has become known as Mohr's circle and is an elementary concept that all mechanical and civil engineers should understand. Using the trigonometric identity  $\sin^2 2\alpha + \cos^2 2\alpha = 1$ , one can combine the transformation equations, Eqs. (2.122) and (2.123) to give

$$(\sigma_\alpha - \sigma_m)^2 + \tau_\alpha^2 = R^2, \quad (2.124)$$

where

$$\sigma_m = \frac{\sigma_{xx} + \sigma_{yy}}{2}, \quad (2.125)$$

$$R = \sqrt{\left(\frac{\sigma_{xx} - \sigma_{yy}}{2}\right)^2 + \sigma_{xy}^2}. \quad (2.126)$$

Equation (2.124) is the standard equation for a circle that can be plotted as shown in Fig. 2.13. For any orientation of plane  $\alpha$  in a stressed element the normal  $\sigma_\alpha$  and the

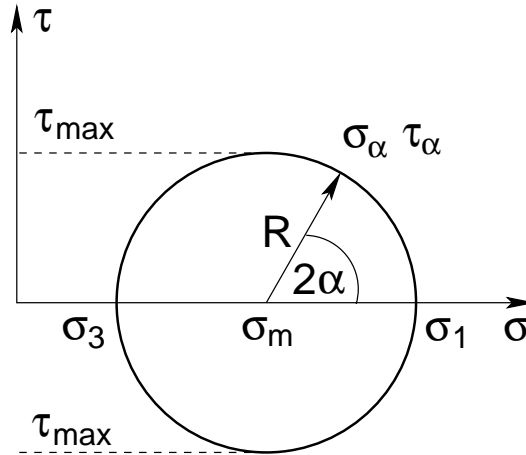


Figure 2.13: Mohr's circle for plane stress

shear  $\tau_\alpha$  stress on the plane can be read from the Mohr's circle. They could equally be calculated using the transformation equations, Eqs. (2.122) and (2.123), but Mohr's circle allows an engineer to visualize the stress state in the body much more easily. The diagram presents a lot of information. Firstly the major and minor principal stresses are shown corresponding to the places where the shear stress is equal to zero. In the center between these is the average normal stress  $\sigma_m$ . From Fig. 2.13 one can also see another characteristic of the transformation equations. The maximum shear stress occurs at angle 45 degrees to the direction of the major principal stress. In this orientation the normal stress is equal to the average normal stress.

### Coulomb's failure criterion

Coulomb proposed a model to describe the failure of soil that requires two material parameters; the angle of friction  $\varphi$  and the cohesion intercept  $c$ . Coulomb stated that the shear stress in a soil at failure  $\tau_f$  is proportionally related to the normal stress at failure  $\sigma_{nf}$ . The cohesion intercept increases the shear strength of the soil by a fixed amount. If there were no normal stresses in the soil then the shear strength would be equal to the cohesion intercept. Numerically Coulomb's failure criterion can be stated as

$$|\tau_f| = c - \sigma_{nf} \tan \varphi. \quad (2.127)$$

When plotted in  $\tau$ - $\sigma_n$  space, Eq. (2.127) defines a 'failure envelope' that is essentially a yield function, see Fig 2.14. It has exactly the same properties and characteristics as a yield function. Below the envelope stresses lie in the elastic regime. On the envelope surface plastic failure occurs. A stress state in the soil above the yield surface is not possible. Essentially the shear strength of a soil is related to the magnitude of the normal force acting upon it. This explains why we place our foundations for buildings at a depth below the ground. The deeper below the ground you move, the greater the normal stresses in the soil due to the self weight of the soil above and the lateral forces from the soil beside

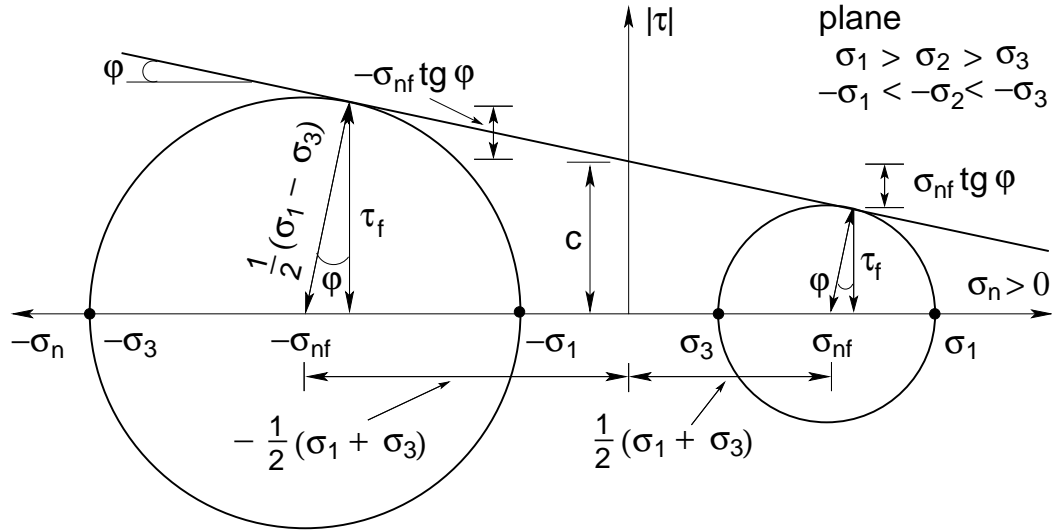


Figure 2.14: Coulomb's failure criterion

any arbitrary point. Therefore, since the normal stresses are larger the deeper one gets, the shear strength of the soil is also larger. Hence, (neglecting water table effects etc), the deeper foundations are placed, the greater the load they can support. This observation is a direct result of Coulomb's failure criterion.

### The Mohr-Coulomb failure criterion

The Mohr-Coulomb failure criterion unites the ideas of transformation equations, Mohr's circles and Coulomb's failure criterion. The necessary parameters that need to be obtained to use Coulomb's failure criterion are the angle of friction  $\varphi$  and the cohesion intercept  $c$ . These are commonly found by the use of a triaxial compression test procedure. A cylindrical sample of soil is placed under triaxial loading such that all three principal stresses can be controlled. Two of the principal stresses are held constant whilst the third (major) one is increased in a controlled gradual fashion. The loading increases until the sample fails at which point the loads are recorded and the principal stresses calculated. These can be plotted as a Mohr's circle and, if required, the normal and shear stresses at failure can be calculated for any orientation of plane in the test sample. The procedure is now repeated but with a different cell pressure. The cell pressure places the loads on the sample that cause the minor and intermediate principal stresses. Now the sample is sheared again by increasing the major principal stress. Note that if a larger cell pressure is used the value of the major principal stress at failure will also be larger as predicted by Coulomb's failure criterion. The results from each sample are plotted as Mohr's circles which typically take the form as in Fig. 2.15. A line is then drawn that is tangential to all the Mohr's circles. This is an experimental method for obtaining Coulomb's failure envelope. As all Mohr's circles are touching the failure envelope they all have stress states inside the soil which represent a failure condition. A very important point to note from

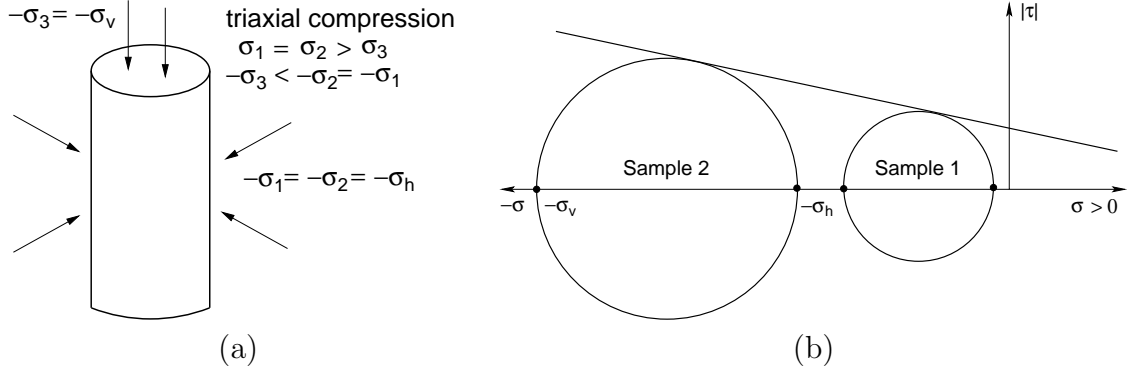


Figure 2.15: a) Triaxial test setup, b) typical Mohr's circles from triaxial tests

this formulation is that the failure shear stress does not correspond to the maximum shear stress in the soil. The shear stress where the circle touches the failure envelope is the failure shear stress. From the plotted results the angle of friction and the cohesion intercept are easily obtained.

Once a triaxial test had been performed and the values of  $\varphi$  and  $c$  obtained, one can use the Mohr-Coulomb failure criterion to estimate failure stress values in the soil under any combinations of loading. The Mohr-Coulomb failure criterion is derived as follows. Consider the results of a triaxial test being plotted as Mohr's circles and the failure envelope drawn as shown in Fig. 2.14. Using the elementary trigonometric identity one can state that

$$\tau_f = \frac{1}{2}(\sigma_1 - \sigma_3) \cos \varphi \quad (2.128)$$

$$\sigma_{nf} = \frac{1}{2}(\sigma_1 + \sigma_3) + \frac{1}{2}(\sigma_1 - \sigma_3) \sin \varphi, \quad (2.129)$$

which upon substitution into Eq. (2.127) gives the Mohr-Coulomb failure criterion, which in the present model is adopted as the yield function

$$F(\sigma_1, \sigma_3) = \frac{1}{2}(\sigma_1 - \sigma_3) + \frac{1}{2}(\sigma_1 + \sigma_3) \sin \varphi - c \cos \varphi = 0. \quad (2.130)$$

Plotting Mohr's circles essentially gives us a graphical way to obtain the shear strength parameters for the soil. They could equally be obtained from the numerical results of two triaxial tests. The stress values for each test could be placed into Eq. (2.130) setting up two simultaneous equations which would be solved for the shear strength parameters. Alternatively if one knows the shear strength parameters and either the major or minor principal stress in the soil the other principal stress at the failure condition can be calculated.

A limitation to using the Mohr-Coulomb failure criterion is that it is independent of the intermediate principal stress. The same failure stress values are predicted for all values of intermediate principal stress. In triaxial testing the intermediate principal stress is always equal to the minor principal stress and the shear strength parameters are obtained

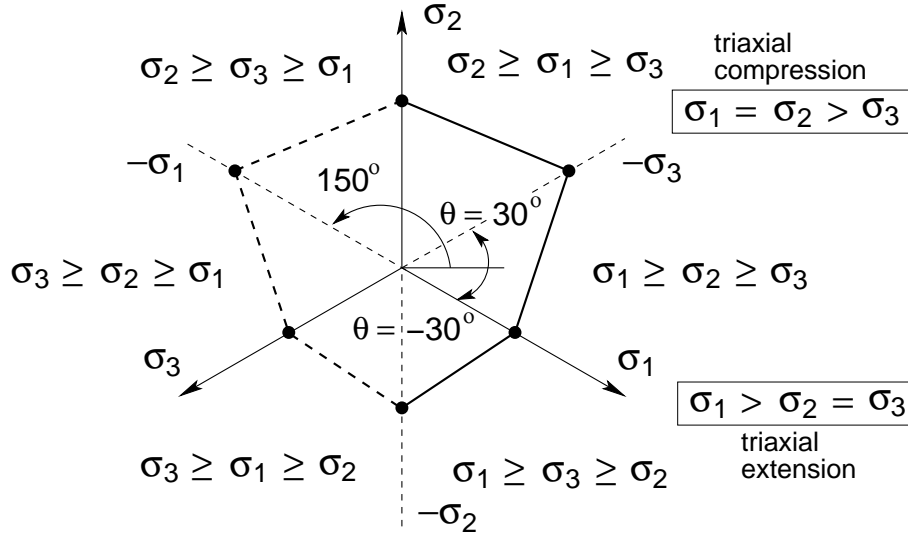


Figure 2.16: Projection of Mohr-Coulomb's failure criterion into deviatoric plane

for these values. In real world geotechnical problems the magnitudes of the intermediate and the minor principal stresses may be different. Some experimental evidence has shown that intermediate stress values can influence the failure condition for soils and this should be appreciated every time an engineer uses any Mohr-Coulomb based models.

In principal stress space the yield function Eq. (2.130) plots as an irregular hexagon in the deviatoric plane as shown in Fig. 2.16. It is evident that the six-fold symmetry arises from possible permutations of principal stresses. It may therefore appear more convenient, if confining our attention to plane  $\sigma_1 > \sigma_2 > \sigma_3$ , to rewrite Eq. (2.130) in terms of stress invariants  $\sigma_m, J, \theta$ . Recall that in terms of stress invariants the principal stresses read

$$\sigma_I = \sigma_m + \frac{2}{\sqrt{3}}J \sin \left[ \theta - (I - 2)\frac{2\pi}{3} \right], \quad I = 1, 2, 3. \quad (2.131)$$

Note that the maximum shear stress  $\tau_{max}$  and the center of Mohr-Coulomb's circle, Fig. 2.14, are then provided by

$$\frac{1}{2}(\sigma_1 - \sigma_3) = \tau_{max} = J \cos \theta, \quad (2.132)$$

$$\frac{1}{2}(\sigma_1 + \sigma_3) = \sigma_m - \frac{J}{\sqrt{3}} \sin \theta. \quad (2.133)$$

Introducing these equations into Eq. (2.130) then yields

$$F(J, \sigma_m, \theta) = J \left( \cos \theta - \frac{1}{\sqrt{3}} \sin \theta \sin \varphi \right) + \sigma_m \sin \varphi - c \cos \varphi = 0. \quad (2.134)$$

Next define

$$g(\theta) = \frac{\sin \theta}{\cos \theta - \frac{1}{\sqrt{3}} \sin \theta \sin \varphi}, \quad (2.135)$$

to finally get upon introducing Eq. (2.135) into (2.134) and rearranging

$$F(J\sigma_m\theta) = J + (\sigma_m - c \cot \varphi)g(\theta) = 0. \quad (2.136)$$

Observe that Eq. (2.136) is formally identical with Eq. (2.78). Unfortunately, Eq. (2.136) may no longer be applicable when moving along the triaxial compression or triaxial extension lines as shown in Fig. 2.16. In either case, at least two segments of the Mohr-Coulomb hexagon then become active. Writing out the respective yield surfaces in terms of principal stresses then becomes more convenient. In particular, the following three segments of the yield surface might be needed when returning the stress point violating the yield criterion back to the yield surface

$$F_1(\sigma_1, \sigma_3, c, \varphi) = \frac{1}{2}(\sigma_1 - \sigma_3) + \frac{1}{2}(\sigma_1 + \sigma_3) \sin \varphi - c \cos \varphi = 0, \quad \sigma_1 \geq \sigma_2 \geq \sigma_3, \quad (2.137)$$

$$F_2(\sigma_2, \sigma_3, c, \varphi) = \frac{1}{2}(\sigma_2 - \sigma_3) + \frac{1}{2}(\sigma_2 + \sigma_3) \sin \varphi - c \cos \varphi = 0, \quad \sigma_2 \geq \sigma_1 \geq \sigma_3, \quad (2.138)$$

$$F_3(\sigma_1, \sigma_2, c, \varphi) = \frac{1}{2}(\sigma_1 - \sigma_2) + \frac{1}{2}(\sigma_1 + \sigma_2) \sin \varphi - c \cos \varphi = 0, \quad \sigma_1 \geq \sigma_2 \geq \sigma_3, \quad (2.139)$$

with corresponding plastic potential surfaces

$$G_1(\sigma_1, \sigma_3, \psi) = \frac{1}{2}(\sigma_1 - \sigma_3) + \frac{1}{2}(\sigma_1 + \sigma_3) \sin \psi, \quad (2.140)$$

$$G_2(\sigma_2, \sigma_3, \psi) = \frac{1}{2}(\sigma_2 - \sigma_3) + \frac{1}{2}(\sigma_2 + \sigma_3) \sin \psi, \quad (2.141)$$

$$G_3(\sigma_1, \sigma_2, \psi) = \frac{1}{2}(\sigma_1 - \sigma_2) + \frac{1}{2}(\sigma_1 + \sigma_2) \sin \psi, \quad (2.142)$$

where  $\psi$  is the familiar dilation angle. Individual components of vectors normal to the yield and plastic potential surfaces are then constant independent of stresses given by

- segment  $\sigma_1 \geq \sigma_2 \geq \sigma_3$  ( $F_1, G_1$ )

$$\{\mathbf{n}^1\} = \left\{ \frac{\partial F_1}{\partial \sigma} \right\} = \frac{1}{2} \{1 + \sin \varphi, 0, -1 + \sin \varphi\}^T, \quad (2.143)$$

$$\{\mathbf{n}_g^1\} = \left\{ \frac{\partial G_1}{\partial \sigma} \right\} = \frac{1}{2} \{1 + \sin \psi, 0, -1 + \sin \psi\}^T. \quad (2.144)$$

- segment  $\sigma_2 \geq \sigma_1 \geq \sigma_3$  ( $F_2, G_2$ )

$$\{\mathbf{n}^2\} = \left\{ \frac{\partial F_2}{\partial \sigma} \right\} = \frac{1}{2} \{0, 1 + \sin \varphi, -1 + \sin \varphi\}^T, \quad (2.145)$$

$$\{\mathbf{n}_g^2\} = \left\{ \frac{\partial G_2}{\partial \sigma} \right\} = \frac{1}{2} \{0, 1 + \sin \psi, -1 + \sin \psi\}^T. \quad (2.146)$$

- segment  $\sigma_1 \geq \sigma_3 \geq \sigma_2$  ( $F_3, G_3$ )

$$\{\mathbf{n}^3\} = \left\{ \frac{\partial F_3}{\partial \sigma} \right\} = \frac{1}{2} \{1 + \sin \varphi, -1 + \sin \varphi, 0\}^T, \quad (2.147)$$

$$\{\mathbf{n}_g^3\} = \left\{ \frac{\partial G_3}{\partial \sigma} \right\} = \frac{1}{2} \{1 + \sin \psi, -1 + \sin \psi, 0\}^T. \quad (2.148)$$

### Stress return algorithm and multi-surface plasticity

To simplify the matter we limit our attention to rigid plasticity with no hardening  $H = 0$ . Such an assumption is also adopted in the program GEO FEM. The reader interested in applications that include isotropic hardening/softening plasticity can consult the work by Pankaj and Bićanić [28]

To proceed, consider first a “working sector” defined by a domain such that  $\sigma_1 \geq \sigma_2 \geq \sigma_3$ , Fig. 2.16. A brief comment on the concept of the working sector is appropriate as the implementation of the entire model is centered around the idea. The loading that is applied to the soil is increased in increments from the initial conditions. An “elastic prediction” is used to estimate the stress state in the material at the end of each loading increment. However when the material is no longer elastic the actual magnitude of stress in the material after this plastic flow would be lower than that forecast by the elastic prediction. As a result the elastic prediction corresponds to a stress point that violates the yield surface. The stress return scheme is then implemented and the stress state gets returned back to the yield surface. The idea of the working sector originates from the order in which the model calculates the relevant values. If plasticity is detected, the model makes the elastic prediction in terms of the six components of the stress vector. After this the model then calculates the magnitude and orientation of the principal stresses based on the elastic prediction stress values. The elastic guess can then be plotted in principal stress space. The model calculates the principal stresses such that  $\sigma_1 \geq \sigma_2 \geq \sigma_3$  and because the conversion from six dimensional stress space to three dimensional principal stress space is based on the elastic prediction stress values, the elastic prediction itself must lie in the sector where  $\sigma_1 \geq \sigma_2 \geq \sigma_3$ . This is defined as the working sector and the elastic prediction stress will always lie in this domain due to the orientation of the principal stress axes being based on the values of the elastic prediction stress.

Upon bringing the elastic guess back to the yield surface the following two scenarios as plotted in Fig. 2.17 may occur. First refer to Figs. 2.17(a),(b) demonstrating a successful return back to the “working sector” thus employing only a single yield function  $F_1$ . The return algorithm, however, failed in the example plotted in Fig. 2.17(c). Although bringing the initial elastic guess back to the assumed active yield function  $F_1$ , blue line, the resulting stress state violates the yield function  $F_2$ . It is interesting to note that if reordering the principal stresses in the definition of Lode’s angle such that  $\sigma_2 \geq \sigma_1 \geq \sigma_3$ , the algorithm returns the stress back to function  $F_2$ , green line. This particular situation suggests that more than one yield function may be active at the same time.

To provide some explanation observe that where arbitrary two planes of the Mohr-Coulomb hexagon intersect, the yield functions are not smoothly defined and a set of edges are formed. If the stress state of the material is such that it lies on one of these vertices, two yield functions are simultaneously active and have values equal to zero. The problem arises of determining the direction and magnitude of the incremental plastic strains in this situation. As both yield functions are simultaneously active, the incremental plastic strains must be related to both the plastic potential functions of the violated yield functions. Koiter [39] showed that for associated plasticity the incremental plastic strains

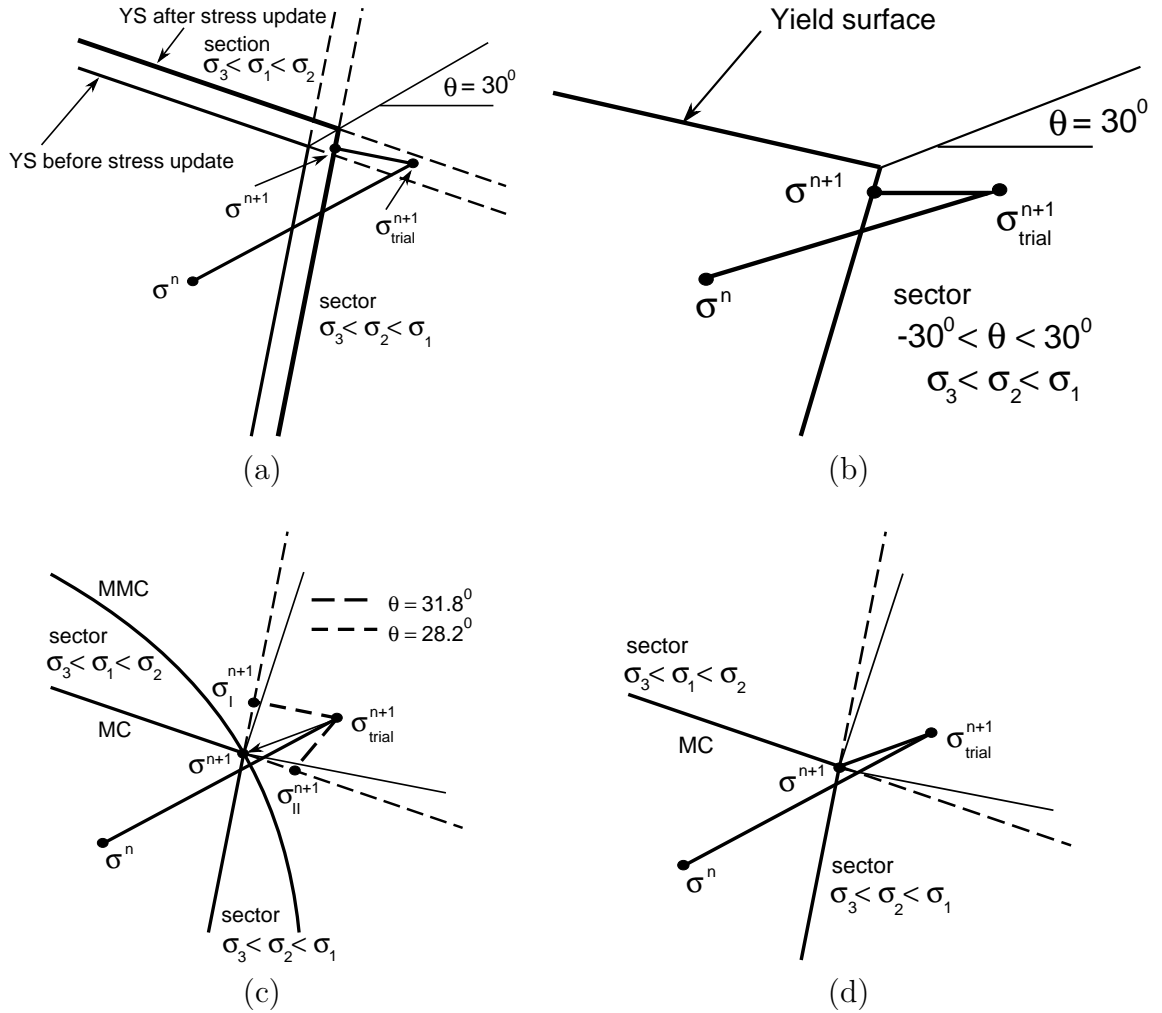


Figure 2.17: a) Successful return to working sector  $\psi = \varphi$ , b) successful return to working sector  $\psi = 0$ , c) failure to return to working sector  $\psi = 0$ , d) successful return to triaxial compression cone  $\psi = 0$

can be determined from

$$\{\Delta\varepsilon^{pl}\} = \sum_{j=1}^m \Delta\lambda_j \left\{ \frac{\partial F_j}{\partial \sigma} \right\}. \quad (2.149)$$

For  $m$  active yield functions  $F_j$ ,  $\lambda_j$  are the plastic multipliers and  $\{\Delta\varepsilon^p\}$  and  $\{\sigma\}$  are the incremental plastic strain and accumulated stress vectors respectively. Hence the total incremental plastic strains are the summed contributions of the incremental plastic strains related to each of the active yield surfaces.

Using the concept of multi-surface plasticity the plastic corrector algorithm then returns the stress to the common intersection of the two active surfaces as plotted in Fig. 2.17(d). It should be noted, however, that violating both yield functions at the elastic predictor stage does not necessarily imply that both yield conditions are active as



evident from Fig. 2.17(a). To determine whether a single or multiple yield surfaces are active one may appreciate a set of singularity indicators developed, e.g. in [28]. Here, a rather simplistic approach for identification of multi-surface plasticity return based on the Lode angle stress invariant is employed. The Lode angle  $\theta$  specifies the orientation of any stress state on the deviatoric plane and can be stated in principal stresses as

$$\theta = \arctan \left( \frac{1}{\sqrt{3}} \left( 2 \frac{(\sigma_2 - \sigma_3)}{(\sigma_1 - \sigma_3)} - 1 \right) \right). \quad (2.150)$$

The procedure starts from performing a single surface plasticity stress return from the elastic prediction stress. The Lode angle is then calculated for the returned stress. If the value lies within the limits  $-30^\circ \leq \theta \leq 30^\circ$ , then the stress return is successful. This situation is indicated in Fig. 2.17(b). If another stress return is considered, this time when the element is placed under triaxial compression, Fig. 2.17(c), upon calculating the Lode angle one will find that it lies outside the limits  $-30^\circ \leq \theta \leq 30^\circ$ . In this situation one can see that one yield function remains violated after the stress return consequently indicating that a multi-surface plasticity stress return is required from the elastic prediction stress. This is then performed and the stress path is that indicated by Fig. 2.17(d) returning the stress state to the apex of the two yield functions as shown.

A special situation arises, see also [28], when returning the stress to the apex of the combined Mohr-Coulomb yield surface. In such a case all six planes are active. Nevertheless, as discussed in [28], the set of six equations corresponding to six yield functions Fig. 2.16 are linearly dependent and rank deficient by three. Therefore, only three arbitrary yield functions, say  $F_1, F_2, F_3$  in Eqs. (2.137) - (2.139), are needed in the plastic corrector stage. A word of caution is required, however, when applying the procedure with non-associated plasticity with the dilation angle  $\psi$  equal to zero. The resulting system of equations is then singular. Fortunately, to avoid such a situation we may always set  $\psi = \varphi$  to perform the apex return.

The single yield surface and multi-surface plasticity concepts will be now discussed separately.

**Single yield surface plasticity** Consider again the “working sector”  $\sigma_1 \geq \sigma_2 \geq \sigma_3$  with the corresponding yield and plastic potential functions  $F_1$  and  $G_1$  and normal vectors  $\{\mathbf{n}^1\}, \{\mathbf{n}_g^1\}$  represented by Eqs. (2.137), (2.140), (2.143), (2.144). Assuming rigid plasticity,  $H = 0$ , the consistency condition Eq. (2.14) becomes

$$\Delta F_1 = \left\{ \frac{\partial F_1}{\partial \sigma} \right\}^T \{\Delta \sigma\} = 0, \quad (2.151)$$

$$\{\Delta \sigma\} = [\mathbf{D}^{\text{el}}] \{\Delta \varepsilon\} - \Delta \lambda [\mathbf{D}^{\text{el}}] \{\mathbf{n}_g^1\}, \quad (2.152)$$

where  $[\mathbf{D}^{\text{el}}]$  is the elastic  $3 \times 3$  material stiffness matrix. Combining Eqs. (2.151) - (2.152) yields the desired plastic multiplier in the form

$$\Delta \lambda = \frac{\{\mathbf{n}^1\}^T [\mathbf{D}^{\text{el}}] \{\Delta \varepsilon\}}{\{\mathbf{n}^1\}^T [\mathbf{D}^{\text{el}}] \{\mathbf{n}_g^1\}} = \frac{\{\mathbf{n}^1\}^T \{\Delta \sigma^{\text{tr}}\}}{\{\mathbf{n}^1\}^T [\mathbf{D}^{\text{el}}] \{\mathbf{n}_g^1\}}, \quad (2.153)$$

where  $\{\Delta\sigma^{tr}\}$  is the elastic trial stress increment. Note that condition (2.151) is identical to

$$F_1^{n+1}(\boldsymbol{\sigma}^{n+1}) = 0 = \underbrace{F_1^n}_{=0} + \overbrace{\frac{1}{2}(\Delta\sigma_1^{tr} - \Delta\sigma_3^{tr}) + \frac{1}{2}(\Delta\sigma_1^{tr} + \Delta\sigma_3^{tr})\sin\varphi}^{\{\mathbf{n}\}^T\{\Delta\sigma^{tr}\}} \quad (2.154)$$

$$- \underbrace{\Delta\lambda \left[ \frac{1}{2}(D_{11}n_{g1}^1 - D_{33}n_{g3}^1) + \frac{1}{2}(D_{11}n_{g1}^1 + D_{33}n_{g3}^1)\sin\varphi \right]}_{\{\mathbf{n}^1\}^T[\mathbf{D}^{el}]\{\mathbf{n}_g^1\}},$$

which allows for evaluation of  $\Delta\lambda$ . In Eq. (2.155)  $F_1^{n+1}$  and  $F_1^n$  refer to the values of  $F_1$  at the  $n$ -th and  $(n+1)$ -th load increments, respectively. Also note that a diagonal material stiffness matrix was assumed for simplicity. Also note that

$$\{\mathbf{n}\}^T\{\Delta\sigma^{tr}\} = F_1^{n+1}(\boldsymbol{\sigma}^{tr}),$$

offers the plastic strain increment  $\Delta\lambda$  in the form

$$\Delta\lambda = \frac{F_1^{n+1}(\boldsymbol{\sigma}^{tr})}{\{\mathbf{n}^1\}^T[\mathbf{D}^{el}]\{\mathbf{n}_g^1\}}. \quad (2.155)$$

Therefore, either of the three Eqs. (2.153) - (2.155) can be used in the plastic corrector stage. The algorithmic tangent stiffness matrix in principal stress space then directly follows from Eq. (2.33) since matrices  $\mathbf{D}^{el}$  and  $\mathcal{D}$ , recall Eq. (2.48), are identical.

**Multi-yield surface plasticity** Although the procedure discussed henceforth can be generalized to any number of active yield surface, the attention will be limited for the sake of clarity to only two arbitrary yield functions simultaneously active with the notation adopted from [29], Section 8.4.

As an example consider the case of triaxial compression already examined in Figs. 2.17. One can then show how the plastic multipliers are calculated to enable the determination of the incremental plastic strains. The derivation is very similar to obtaining the plastic multipliers for single surface plasticity except that in this case, to obtain both plastic multipliers, a pair of simultaneous equations need to be solved. Initially separate the incremental strains into their elastic  $\{\Delta\varepsilon^{el}\}$  and plastic  $\{\Delta\varepsilon^{pl}\}$  components. The plastic strains are then sub-divided into the contributions from each violated yield surface  $\{\Delta\varepsilon^{p1}\}$ ,  $\{\Delta\varepsilon^{p2}\}$  such that the total incremental plastic strain  $\{\Delta\varepsilon\}$  is

$$\{\Delta\varepsilon\} = \{\Delta\varepsilon^{el}\} + \{\Delta\varepsilon^{p1}\} + \{\Delta\varepsilon^{p2}\}. \quad (2.156)$$

The incremental stresses  $\{\Delta\sigma\}$  are again related to the incremental elastic strains by the elastic constitutive matrix  $[\mathbf{D}^{el}]$  in the following way

$$\{\Delta\sigma^{tr}\} = [\mathbf{D}^{el}]\{\Delta\varepsilon^{el}\}. \quad (2.157)$$

Combining Eqs. (2.156) and (2.157) gives

$$\{\Delta\sigma\} = [D^{el}] (\{\Delta\varepsilon\} - \{\Delta\varepsilon^{p1}\} - \{\Delta\varepsilon^{p2}\}). \quad (2.158)$$

The flow rule is now written for each of the plastic potential functions

$$\{\Delta\varepsilon^{p1}\} = \Delta\lambda_1 \left\{ \frac{\partial G_1}{\partial \sigma} \right\}, \quad (2.159)$$

$$\{\Delta\varepsilon^{p2}\} = \Delta\lambda_2 \left\{ \frac{\partial G_2}{\partial \sigma} \right\}. \quad (2.160)$$

Upon substitution of Eqs. (2.159) and (2.160) into Eq. (2.158) gives

$$\{\Delta\sigma\} = [D^{el}] \{\Delta\varepsilon\} - \Delta\lambda_1 [D^{el}] \left\{ \frac{\partial G_1}{\partial \sigma} \right\} - \Delta\lambda_2 [D^{el}] \left\{ \frac{\partial G_2}{\partial \sigma} \right\}. \quad (2.161)$$

Before we proceed any further with the development of this derivation look at the structure of Eq (2.161). If one were to multiply through by  $[D^{el}]^{-1}$  and then rearrange you would obtain the following

$$\{\Delta\varepsilon\} - \{\Delta\varepsilon^{el}\} = \{\Delta\varepsilon^{pl}\} = \Delta\lambda_1 \left\{ \frac{\partial G_1}{\partial \sigma} \right\} + \Delta\lambda_2 \left\{ \frac{\partial G_2}{\partial \sigma} \right\}. \quad (2.162)$$

Observing Eq. (2.162) one can clearly see that Koiter's generalization [39] can be extended for non-associated plasticity behavior by replacing the yield functions with their respective plastic potential functions. Thus Eq. (2.162) verifies

$$\{\Delta\varepsilon^{pl}\} = \sum_{j=1}^m \Delta\lambda_j \left\{ \frac{\partial G_j}{\partial \sigma} \right\} = \sum_{j=1}^m \Delta\lambda_j \{n_g^j\}. \quad (2.163)$$

Hence one can use the flow rule to obtain the total incremental plastic strains when using multi-surface plasticity if the contribution of each plastic potential function is summed. One still needs to calculate the plastic multipliers. This is done by acknowledging that when both yield surfaces are active, the values of both of them is zero, and the consistency condition is satisfied. Using the chain rule on this observation gives ( $H = 0$ )

$$\Delta F_1 = \left\{ \frac{\partial F_1}{\partial \sigma} \right\}^T \{\Delta\sigma\} = \{n^1\}^T \{\Delta\sigma\} = 0, \quad (2.164)$$

$$\Delta F_2 = \left\{ \frac{\partial F_2}{\partial \sigma} \right\}^T \{\Delta\sigma\} = \{n^2\}^T \{\Delta\sigma\} = 0. \quad (2.165)$$

Substitution of Eq. (2.161) into (2.164) and (2.165) yields

$$\Delta F_1 = \{n^1\}^T [D^{el}] \{\Delta\varepsilon\} - \Delta\lambda_1 \{n^1\}^T [D^{el}] \{h_g^1\} - \Delta\lambda_2 \{n^1\}^T [D^{el}] \{n_g^2\} = 0, \quad (2.166)$$

$$\Delta F_2 = \{n^2\}^T [D^{el}] \{\Delta\varepsilon\} - \Delta\lambda_1 \{n^2\}^T [D^{el}] \{n_g^1\} - \Delta\lambda_2 \{n^2\}^T [D^{el}] \{n_g^2\} = 0. \quad (2.167)$$

A set of simultaneous equations are now set in place and are solved for the plastic multipliers. Equations (2.166) and (2.167) can now be written in a simplified form as

$$\Delta\lambda_1 L_{11} + \Delta\lambda_2 L_{12} = T_1, \quad (2.168)$$

$$\Delta\lambda_1 L_{21} + \Delta\lambda_2 L_{22} = T_2, \quad (2.169)$$

where

$$L_{11} = \{\mathbf{n}^1\}^T [\mathbf{D}^{\text{el}}] \{\mathbf{n}_g^1\}, \quad (2.170)$$

$$L_{22} = \{\mathbf{n}^2\}^T [\mathbf{D}^{\text{el}}] \{\mathbf{n}_g^2\}, \quad (2.171)$$

$$L_{12} = \{\mathbf{n}^1\}^T [\mathbf{D}^{\text{el}}] \{\mathbf{n}_g^2\}, \quad (2.172)$$

$$L_{21} = \{\mathbf{n}^2\}^T [\mathbf{D}^{\text{el}}] \{\mathbf{n}_g^1\}, \quad (2.173)$$

$$T_1 = \{\mathbf{n}^1\}^T [\mathbf{D}^{\text{el}}] \{\Delta\boldsymbol{\varepsilon}\}, \quad (2.174)$$

$$T_2 = \{\mathbf{n}^2\}^T [\mathbf{D}^{\text{el}}] \{\Delta\boldsymbol{\varepsilon}\}. \quad (2.175)$$

Thus the plastic multipliers are calculated as

$$\Delta\lambda_1 = (L_{22}T_1 - L_{12}T_2) / (L_{11}L_{22} - L_{12}L_{21}), \quad (2.176)$$

$$\Delta\lambda_2 = (L_{11}T_2 - L_{21}T_1) / (L_{11}L_{22} - L_{12}L_{21}). \quad (2.177)$$

These are then used in Eq. (2.162) or (2.163) to calculate the incremental plastic strains. This process can be easily extended using the same concepts when one has more than two surface multi-surface plasticity such as the apex problem or the Mohr-Coulomb yield surface combined with a tension cut off problem. This concept is outlined in Section 2.3.8.

As for the tangent stiffness matrix  $\mathbf{D}^{\text{ep}}$  its derivation may proceed along the same lines as discussed in Section 2.3.3. To that end we substitute from Eqs. (2.176) - (2.177) into Eq. (2.161) to get after rearranging, see also [29],

$$[\mathbf{D}^{\text{ep}}] = [\mathbf{D}^{\text{el}}] - \frac{[\mathbf{D}^{\text{el}}]}{\Omega} [\{\mathbf{n}_g^1\}\{\mathbf{b}_1\}^T + \{\mathbf{n}_g^2\}\{\mathbf{b}_2\}^T] [\mathbf{D}^{\text{el}}], \quad (2.178)$$

$$\Omega = L_{11}L_{22} - L_{12}L_{21},$$

$$\{\mathbf{b}_1\} = L_{22}\{\mathbf{n}^1\} - L_{12}\{\mathbf{n}^2\},$$

$$\{\mathbf{b}_2\} = L_{11}\{\mathbf{n}^2\} - L_{21}\{\mathbf{n}^1\}.$$

A similar procedure can be applied when more than two yield surfaces are active. Recall, e.g. the apex problem, where all three surfaces  $F_1, F_2, F_3$  are simultaneous active. In fact, all six surfaces shown in Fig. 2.16 are active, but only three are needed to bring the stress to their common point of intersection [28]. Such a situation will also arise in Section 2.3.8 that outlines tension cut-off extension of the original mohr-coulomb formulation. While it is shown that four yield surfaces may become active at the same, again only three of them can be chosen in the multi-surface plasticity stress update procedure if limiting attention to isotropic material.

In every case, assuming rigid plasticity, the following generalization of Eqs. (2.164) - (2.178) applies. Suppose that  $N$  yield surfaces are active. The increments of plastic multipliers then follow from

$$\{\Delta\lambda\} = [\mathbf{L}] \{\mathbf{T}\}, \quad (2.179)$$

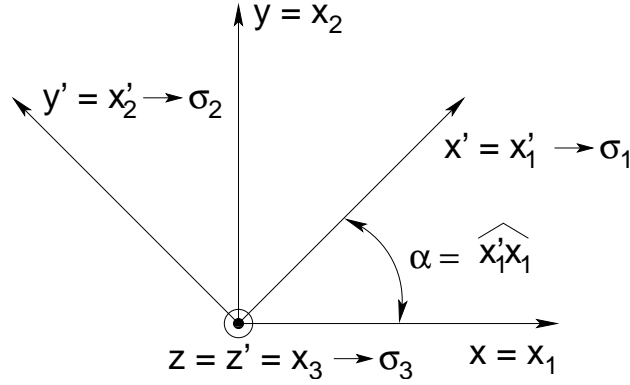


Figure 2.18: Transformation of coordinates for plane strain and axisymmetric problems

where the components of  $N \times N$  matrix  $[L]$  and  $N \times 1$  vector  $\{T\}$  are provided by

$$L_{ij} = \{n^i\}^T [D^{el}] \{n_g^j\}, \quad (2.180)$$

$$T_i = \{n^i\}^T [D^{el}] \{\Delta \varepsilon\}. \quad (2.181)$$

The tangent stiffness matrix then becomes

$$[D^{ep}] = [D^{el}] - [D^{el}] \left( \sum_{i=1}^N \{n_g^i\} \{b_i\}^T \right) [D^{el}], \quad (2.182)$$

$$\{b_i\} = \sum_{j=1}^N L_{ij}^{-1} \{n^j\}.$$

**Tangent stiffness matrix in the cartesian coordinate system** The principal stress space was adopted throughout this section to develop the general framework for the implementation of the Mohr-Coulomb constitutive model. On the other hand, the derivation of the finite element stiffness matrices presented in Section 1 assumes a material point to be placed in a certain global cartesian coordinate system. The instantaneous  $3 \times 3$  material tangent stiffness matrices that appear in Eqs. (2.178) and (2.182) thus require some transformation as demonstrated in Fig. 2.3.7 For further reference these matrices will be provided with subscript  $I$  while their cartesian counterparts will be denoted by subscript  $g$ . The same notation is reserved also for respective stress and strain vectors.

The transformation law is usually found through equality of increments of work in both coordinate spaces written as

$$\{\Delta \varepsilon_g\}^T [D_g^{ep}] \{\Delta \varepsilon_g\} = \{\Delta \varepsilon_I\}^T [D_I^{ep}] \{\Delta \varepsilon_I\}. \quad (2.183)$$

To continue, introduce a certain  $3 \times 6$  transformation matrix  $[T_I^e]$  (note that the general six-dimensional cartesian stress space is temporarily assumed)

$$[T_I^e] = \begin{bmatrix} n_{11}n_{11} & n_{12}n_{12} & n_{13}n_{13} & n_{12}n_{13} & n_{11}n_{13} & n_{11}n_{12} \\ n_{21}n_{21} & n_{22}n_{22} & n_{23}n_{23} & n_{22}n_{23} & n_{21}n_{23} & n_{21}n_{22} \\ n_{31}n_{31} & n_{32}n_{32} & n_{33}n_{33} & n_{32}n_{33} & n_{31}n_{33} & n_{31}n_{32} \end{bmatrix}, \quad (2.184)$$

where  $n_{ij}$  represent components of  $3 \times 3$  orthogonal rotation matrix  $[\mathbf{T}]$  giving the relation between coordinates in individual spaces, see Fig. 2.3.7, in the form

$$\{\mathbf{x}_i\} = [\mathbf{T}] \{\mathbf{x}_g\}. \quad (2.185)$$

With reference to Fig. 2.3.7 the matrix  $[\mathbf{T}]$  then attains a simple form (assuming  $\sigma_1 > \sigma_2 > \sigma_3$ )

$$[\mathbf{T}] = \begin{bmatrix} \cos \alpha & \sin \alpha & 0 \\ -\sin \alpha & \cos \alpha & 0 \\ 0 & 0 & 1 \end{bmatrix}, \quad (2.186)$$

In general, individual columns in  $[\mathbf{T}]$  correspond to principal directions of stresses  $\sigma_1, \sigma_2, \sigma_3$ . The matrix  $[\mathbf{T}_i^\varepsilon]$  then rotates the cartesian strain components into the principal stress space such that

$$\{\Delta \varepsilon_i\} = [\mathbf{T}_i^\varepsilon] \{\Delta \varepsilon_g\}. \quad (2.187)$$

Substitution of Eq. (2.187) into Eq. (2.183) yields

$$[\mathbf{D}_g^{\text{ep}}] = [\mathbf{T}_i^\varepsilon]^\top [\mathbf{D}_i^{\text{ep}}] [\mathbf{T}_i^\varepsilon] \quad (2.188)$$

Note that for plane strain and axisymmetric problems the general  $6 \times 6$  material stiffness matrix  $[\mathbf{D}_g^{\text{ep}}]$  in Eq. (2.188) must be reduced into  $4 \times 4$  matrix and suitably augmented to comply with the notation introduced in Section 1. Finally, it is perhaps interesting to point out the relation between stress vectors

$$\{\Delta \sigma_g\} = [\mathbf{T}_g^\sigma] \{\Delta \sigma_i\}, \quad (2.189)$$

where

$$[\mathbf{T}_g^\sigma] = [\mathbf{T}_i^\varepsilon]^\top. \quad (2.190)$$

### 2.3.8 Mohr-Coulomb model with tension cut-off

The standard Mohr-Coulomb model allows for certain amount of tension that is in general proportional to the soil strength parameters  $c, \varphi$  such that its maximum value cannot exceed  $\sqrt{3} c \cot \varphi$ , see Fig. 2.19(a). In reality, however, the soil can sustain almost none or very small values of these stresses. Also, the tension carrying capacity of soils is not commonly relied upon as it is typically extremely variable and unpredictable in real soils. It is therefore desirable to either avoid tension completely or to limit its magnitude by a specific value of the ultimate tensile stress  $\sigma_t$  the material can sustain before plastic failure. This can be achieved by introducing three additional tension cut-off yield surfaces of the Rankine type, Figs. 2.19(b)(c), in the form

$$T_1(\sigma_1, \sigma_t) = \sigma_1 - \sigma_t = 0, \quad (2.191)$$

$$T_2(\sigma_2, \sigma_t) = \sigma_2 - \sigma_t = 0, \quad (2.192)$$

$$T_3(\sigma_3, \sigma_t) = \sigma_3 - \sigma_t = 0. \quad (2.193)$$

The model assumes the material to have isotropic properties and hence the ultimate tensile strength  $\sigma_t$  is the same in all orientations. Furthermore, an associated plastic flow

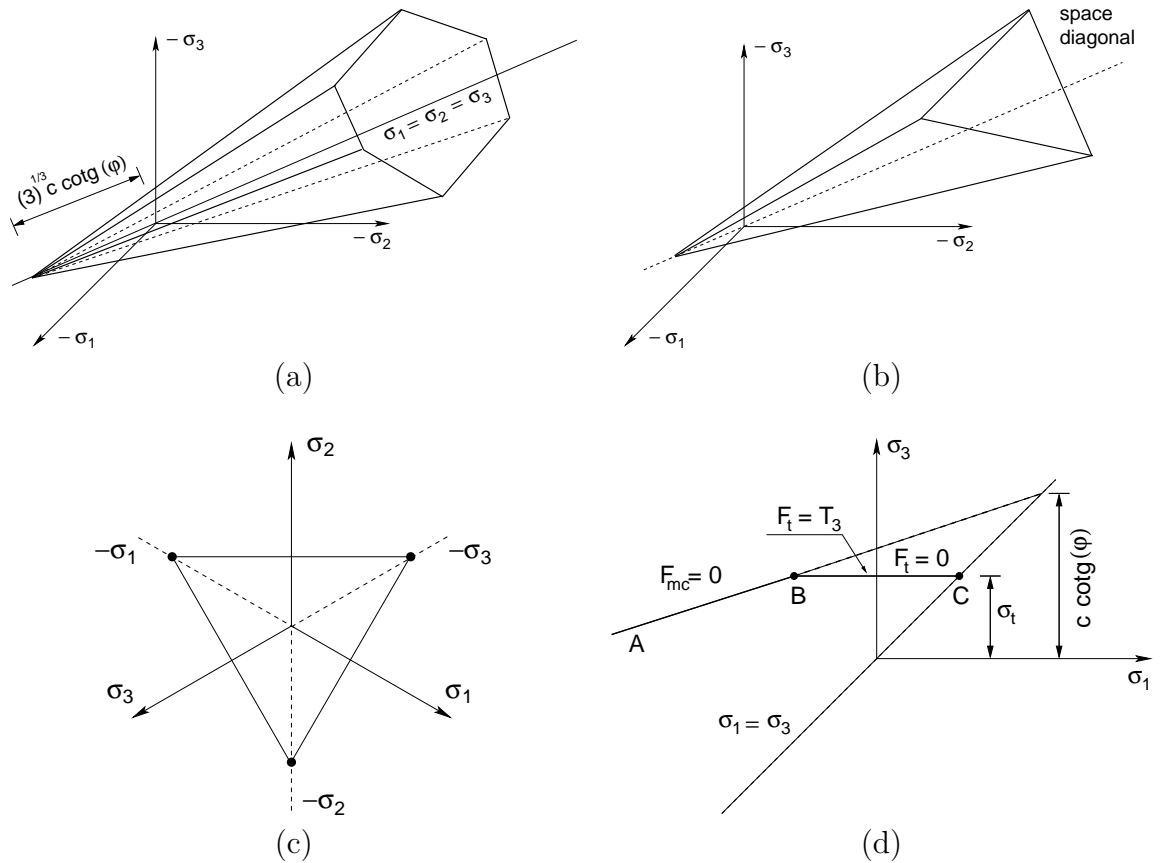


Figure 2.19: Mohr-Coulomb model extended by tension cut-off: a) 3D plot of Mohr-Coulomb model in principal stress space, b) 3D plot of tension cut-off yield surface in principal stress space, c) projection of tension cut-off surface into deviatoric plane, d) projection of the combined Mohr-Coulomb and tension cut-off yield surfaces into  $\sigma_1 - \sigma_3$  stress space

rule is adopted in conjunction with tension cut-off. The tensile yield surfaces plot as a regular triangular pyramid in principal stress space, see Fig. 2.19(b).

The shear and tension yield surfaces intersect in the tensile domain of the principal stress space. As a result, the tension yield surfaces “cut-off” the shear yield surfaces leading to the effect of the material being able to ultimately sustain lower tensile stresses than those predicted as being possible by the Mohr-Coulomb model alone, Fig. 2.19(d). Note that point B in Fig. 2.19(d) corresponds to a point of intersection of the Mohr-Coulomb  $F_{mc}$  and the tension cut-off  $F_t$  yield surfaces. Should the line A-C represent an edge of two planes of the Mohr-Coulomb yield surfaces, then there would be at least three simultaneously active yield surfaces.

If the material element were placed under triaxial tension then the stress path during the increase in loading would follow the space diagonal towards the apex of the tension cut-off pyramid. As the failure criterion would now map out as a regular triangular pyramid rather than an irregular hexagonal pyramid the number of surfaces violated when the

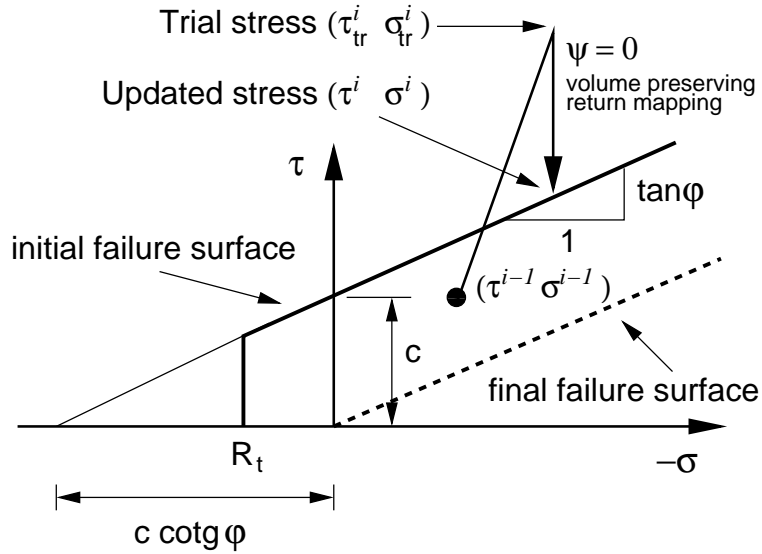


Figure 2.20: Failure surface for interface model

element reached the plastic state would be three as in the case of the pure Mohr-Coulomb failure criterion.

## 2.4 Interface constitutive model

A proper modeling of soil–structure interaction requires a suitable treatment of relative movement of the structure with respect to the soil that usually occurs. In the framework of continuum mechanics, the most appealing way of treating interfaces is the use of interface elements discussed in Section 1.3.4. The formulation of interface elements presented therein will be completed in this section by introducing an interface material model that can be used to simulate contact between two materials, e.g. a concrete pile and soil.

In GEO FEM the interface material is based on the Mohr-Coulomb failure criterion with tension cut off, Fig. 2.20. An elastic – rigid plastic response of the interface material in shear is assumed. Such a behavior is schematically illustrated in Fig. 2.21(a) showing a variation of the shear stress as a function of the relative tangential displacement. In tension or compression a purely elastic response of the interface material is considered. When the tensile stress  $\sigma$  exceeds a certain allowable strength limit  $R_t$ , the initial yield surfaces collapses to a residual surface which corresponds to dry friction, see Figs. 2.20 and 2.21(b).

### 2.4.1 Yield surface and stress update procedure

The mathematical representation of the initial yield surface displayed in Fig. 2.20 is given by

$$F = |\tau| + \sigma \tan \varphi - c, \quad (2.194)$$



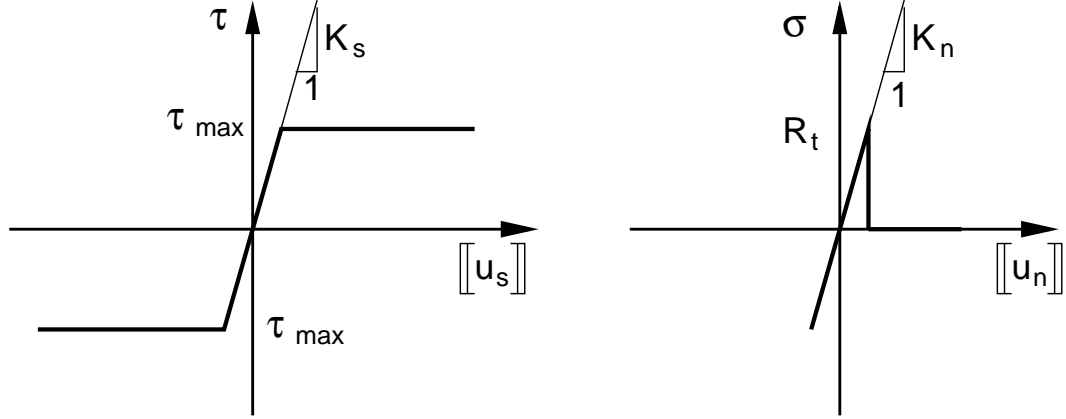


Figure 2.21: Constitutive model for interface

where  $\varphi$  and  $c$  are the angle of internal friction and cohesion of the interface material, respectively. The direction of the plastic flow depends on the shape of the plastic potential surface. Here, a non-associated plastic flow rule is assumed with the plastic potential function written as

$$G = |\tau| + \sigma \tan \psi, \quad (2.195)$$

where  $\psi$  is the angle of dilation. The angle of dilation controls the magnitude of the irreversible (plastic) volume expansion. As stated in the previous paragraph, the plastic response is limited to shear only which corresponds to the value of the dilation angle  $\psi$  equal to zero (volume preserving return mapping), see Fig. 2.20. Thus, setting  $\psi = 0$  gives the normals to the yield and potential surfaces, Eq. (2.34), in the form

$$\mathbf{n} = \frac{\partial F}{\partial \boldsymbol{\sigma}} = \left\{ \begin{array}{c} \tau/|\tau| \\ \tan \varphi \end{array} \right\}, \quad \mathbf{n}_g = \frac{\partial G}{\partial \boldsymbol{\sigma}} = \left\{ \begin{array}{c} \tau/|\tau| \\ 0 \end{array} \right\}, \quad (2.196)$$

where the stress vector  $\boldsymbol{\sigma}$  follows from Eq. (1.59)

$$\boldsymbol{\sigma} = \{\tau, \sigma\}^T.$$

The normal to the plastic potential function  $\mathbf{n}_g$  then provides the direction of the plastic flow governing the return mapping algorithm. This algorithm is schematically depicted in Fig. 2.20. In particular, when solving a plasticity problem the analysis is carried out in several load increments. To that end, suppose that stresses at state  $i - 1$  are known and we wish to proceed to a new stress state  $i$  by applying a new load increment. This step results into an increment of the vector of relative displacements  $\Delta [\mathbf{u}] = \{\Delta [u], \Delta [v]\}^T$ . The elastic “trial” stresses then follows from

$$\tau_{tr}^i = \tau^{i-1} + K_s \Delta [u]^i, \quad (2.197)$$

$$\sigma_{tr}^i = \sigma^{i-1} + K_n \Delta [v]^i. \quad (2.198)$$

The particular form of  $\mathbf{n}_g$  just confirms the elastic response in the normal direction so that

$$\sigma^i = \sigma_{tr}^i,$$

as evident from Figs. 2.20 and 2.21. The shear stress then follows from the yield condition (2.194). Note that during plastic flow the stresses must remain on the yield surface. Therefore

$$F^i = |\tau^i| + \sigma^i \tan \varphi - c = 0. \quad (2.199)$$

Next, multiplying both sides of Eq. (2.199) by the first component of  $\mathbf{n}_g$ , noting that  $\tau^i/|\tau^i| = \tau_{tr}^i/|\tau_{tr}^i|$  and then solving for  $\tau^i$  gives

$$\tau^i = (-\sigma_{tr}^i \tan \varphi + c) \frac{\tau_{tr}^i}{|\tau_{tr}^i|}.$$

Thus, in the absence of pore pressure the stresses at the end of the  $i^{th}$  load increment are given by

$$\begin{Bmatrix} \tau \\ \sigma \end{Bmatrix}^i = K_n \llbracket v \rrbracket^i \begin{Bmatrix} 0 \\ 1 \end{Bmatrix} + (-\sigma_{tr}^i \tan \varphi + c) \begin{Bmatrix} \tau_{tr}^i/|\tau_{tr}^i| \\ 0 \end{Bmatrix}. \quad (2.200)$$

### 2.4.2 Tangent stiffness matrix

Following [33] the algorithmic tangent stiffness matrix Eq. (2.48) can be found from the expression

$$\mathcal{D}^{cons} = \frac{\partial \sigma^i}{\partial \llbracket \mathbf{u} \rrbracket^i}. \quad (2.201)$$

Referring to Eq. (2.200) it becomes evident that

$$\frac{\partial \left( K_n \llbracket v \rrbracket^i \begin{Bmatrix} 0 \\ 1 \end{Bmatrix} \right)^\top}{\partial \begin{Bmatrix} \llbracket u \rrbracket^i \\ \llbracket v \rrbracket^i \end{Bmatrix}} = K_n \begin{bmatrix} 0 & 0 \\ 0 & 1 \end{bmatrix}, \quad (2.202)$$

$$\frac{\partial \left( (-\sigma_{tr}^i \tan \varphi + c) \begin{Bmatrix} \tau_{tr}^i/|\tau_{tr}^i| \\ 0 \end{Bmatrix} \right)^\top}{\partial \begin{Bmatrix} \llbracket u \rrbracket^i \\ \llbracket v \rrbracket^i \end{Bmatrix}} = \begin{bmatrix} a_{11} & a_{12} \\ 0 & 0 \end{bmatrix}, \quad (2.203)$$

where

$$\begin{aligned} a_{11} &= (-\sigma_{tr}^i \tan \varphi + c) \frac{\partial}{\partial \tau_{tr}^i} \left( \frac{\tau_{tr}^i}{|\tau_{tr}^i|} \right) \frac{\partial \tau_{tr}^i}{\partial \llbracket u \rrbracket^i} \\ a_{12} &= \frac{\partial (-\sigma_{tr}^i \tan \varphi + c)}{\partial \sigma^i} \frac{\partial \sigma^i}{\partial \llbracket v \rrbracket^i} \frac{\tau_{tr}^i}{|\tau_{tr}^i|}. \end{aligned}$$

After expanding individual derivatives in the above expressions we get

$$\begin{aligned} \frac{\partial}{\partial \tau_{tr}^i} \left( \frac{\tau_{tr}^i}{|\tau_{tr}^i|} \right) &= \frac{1}{|\tau_{tr}^i|} - \frac{\tau_{tr}^i (\partial |\tau_{tr}^i| / \tau_{tr}^i)}{|\tau_{tr}^i|^2} = \frac{1}{|\tau_{tr}^i|} \left( 1 - \frac{\tau_{tr}^i \tau_{tr}^i}{|\tau_{tr}^i|^2} \right) = 0, \\ \frac{\partial(-\sigma_{tr}^i \tan \varphi + c)}{\partial \sigma^i} &= -\tan \varphi, \\ \frac{\partial \tau_{tr}^i}{\partial [u]^i} &= K_s, \\ \frac{\partial \sigma^i}{\partial [v]^i} &= K_n. \end{aligned}$$

Finally, introducing the above expressions back into Eq. (2.203) and then adding to Eq. (2.202) provides the desired tangent stiffness matrix in the form

$$\mathcal{D}^{cons} = \begin{bmatrix} 0 & -K_n \tan \varphi (\tau_{tr}^i / |\tau_{tr}^i|) \\ 0 & K_n \end{bmatrix}. \quad (2.204)$$

It is interesting to note that the same result will be recovered if starting from Eq. (2.33) and setting  $H = 0$ . In other words, there is no difference between the standard and algorithmic tangent stiffness matrices for the selected flow rule ( $\psi = 0$ ).

# Chapter 3

## Critical state models for soils

### 3.1 Modified Cam clay model

Roscoe and his co-workers [32], in an attempt of confirming the original findings of Hvorslev [14], introduced the concept of a critical void ratio state at which an unlimited deformation can take place without altering the current stress and void ratio state. Within this behavioral framework a strain-dependent yield surface controlling the progressive yielding of a material sample can be defined. Regardless of their point of departure all material points moving along a certain stress path with a progressively evolving yield surface eventually end at a unique critical void ratio line that belongs to a certain unique state boundary surface when plotted in  $J, \sigma_m, e$  space [32], where  $J$  is defined as the square root of the second invariant of deviatoric stress,  $\sigma_m$  is the mean effective stress and  $e = V_p/V_g$  stands for the void ratio given as the ratio of the volume of pores with respect to the volume of grains.

*Yield surface in  $e - \ln(-\sigma_m)$*

Assuming isotropic loading conditions,  $J = 0$ , allows schematic projection of all points on this surface into a domain bounded by the  $\sigma_m - e$  axis and the virgin or normal consolidation line plotted in Fig. 3.1(a). As suggested in [32] this line represents a loosest packing or greatest void ratio for any given value of  $\sigma_m$  stress. Although theoretically acceptable ( $e = 0$ ) a minimum value  $e_{min} \neq 0$  of void ratio that the soil can experience is usually assumed. From the mathematical formulation the maximum value of void ratio  $e_0$  will be hereafter associated with a stress level  $\|\sigma_m\| = 1$ , Fig. 3.1. For a remoulded clay, the soil initially moves down the virgin consolidation line. When unloaded at a certain level of mean effective stress, e.g.  $\bar{p}_c^0$ , it moves up the so called swelling line. When reloaded, it moves along the same line until it rejoins the normal consolidation line and when stressed even further, it follows this line again.

Both lines are assumed to be straight in  $e - \ln(-\sigma_m)$  space. Introducing the so called compression and swelling moduli  $\lambda, \kappa$ , respectively renders the following equations defining

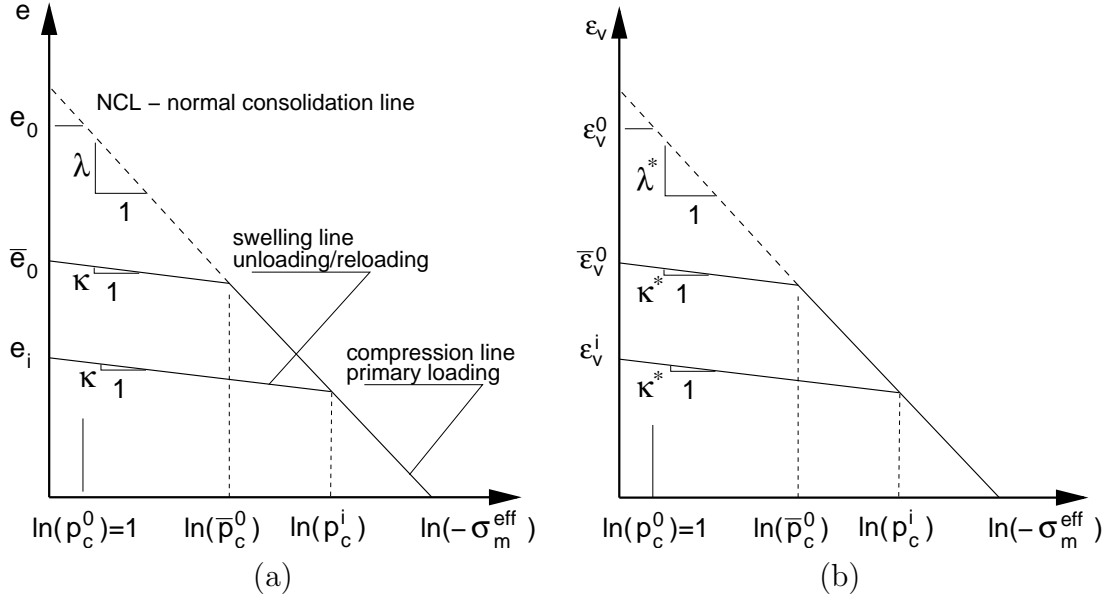


Figure 3.1: Behavior under isotropic compression

the two lines

$$e = e_0 - \lambda \ln(-\sigma_m) \quad \text{-- virgin consolidation line,} \quad (3.1)$$

$$e = \bar{e}_0 - \kappa \ln(-\sigma_m) \quad \text{-- swelling line.} \quad (3.2)$$

Note that minimum void ratio  $e_0$  is generally not known a priori. What is usually known is the current or initial void ratio  $\bar{e}_0$  that can be determined experimentally. As suggested in [16] the value of  $\bar{e}_0$  together with associated pressure  $\bar{p}_c^0$  and moduli  $\lambda, \kappa$  can be found from a simple one-dimensional consolidation test when combined with mathematical formulation of this experiment in the framework of inverse problems. Realizing that  $p_0 = 1$  kPa the determination of  $e_0$  then becomes quite straightforward. Finally, recall that the points of intersection of the two  $\lambda$ - and  $\kappa$ -lines are linked to a certain stress level termed the preconsolidation pressure  $p_c^0, \bar{p}_c^0, p_c^i, \dots$ , the maximum stress level the soil has experienced ever before. From a mathematical formulation it appears more convenient (assuming incompressibility of individual grains) to re-plot Fig. 3.1(a) in  $\varepsilon_v - \ln(-\sigma_m)$  space,  $\varepsilon_v$  being the total volumetric strain, see Fig. 3.1(b). Writing the elastic part of total volumetric strain increment as  $\Delta\varepsilon_v^{\text{el}}$  the rate forms of Eqs. (3.1) and (3.2) then become

$$\dot{\sigma}_m = -\frac{\sigma_m}{\lambda^*} \dot{\varepsilon}_v \quad \text{-- primary loading,} \quad (3.3)$$

$$\dot{\sigma}_m = -\frac{\sigma_m}{\kappa^*} \dot{\varepsilon}_v^{\text{el}} \quad \text{-- unloading-reloading,} \quad (3.4)$$

$$\lambda^* = \frac{\lambda}{1+e}, \quad \kappa^* = \frac{\kappa}{1+e}. \quad (3.5)$$

When moving along the  $\lambda$ -line the material point experiences plastic loading while elastic response is assumed inside the domain. During plastic loading the total volumetric

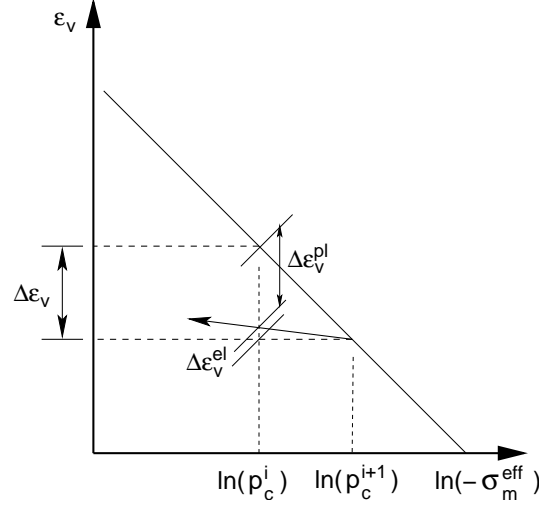


Figure 3.2: Elastic and plastic part of total strain increment

strain increment  $\Delta\varepsilon_v$  can be split into elastic and plastic parts. With reference to Fig. 3.2 we get

$$\Delta\varepsilon_v = -\lambda^* [\ln(p_c^{i+1}) - \ln(p_c^i)], \quad (3.6)$$

$$\Delta\varepsilon_v^{el} = -\kappa^* [\ln(p_c^{i+1}) - \ln(p_c^i)], \quad (3.7)$$

$$\Delta\varepsilon_v^{pl} = -(\lambda^* - \kappa^*) [\ln(p_c^{i+1}) - \ln(p_c^i)], \quad (3.8)$$

or in the rate form

$$\dot{\varepsilon}_v^{pl} = -(\lambda^* - \kappa^*) \frac{\dot{p}_c}{p_c}. \quad (3.9)$$

Integrating Eq. (3.9) then provides the evolution law for preconsolidation pressure  $p_c$  during primary loading in the form

$$p_c^{i+1} = p_c^i \exp \left[ \frac{-\Delta\varepsilon_v^{pl}}{\lambda^* - \kappa^*} \right]. \quad (3.10)$$

Eq. (3.10) thus gives a form of isotropic hardening/softening law for primary loading. During elastic unloading or reloading the preconsolidation pressure  $p_c$  remains constant. In analogy with Eq. (3.10) the evolution of mean effective stress  $\sigma_m$  is provided by

$$\sigma_m^{i+1} = \sigma_m^i \exp \left[ \frac{-\Delta\varepsilon_v^{el}}{\kappa^*} \right]. \quad (3.11)$$

*Yield surface in  $J - \sigma_m$  space*

Assuming a constant value of the void ratio  $e$  and following the work of Roscoe and Burland [31] the projection of the state boundary surface in  $J - \sigma_m$  space is plotted as an ellipse given by

$$F(\boldsymbol{\sigma}, \boldsymbol{\kappa}) = \frac{J^2}{M_{cs}^2} + \sigma_m^2 + \sigma_m p_c = 0, \quad (3.12)$$

where  $p_c$  is the current value of the preconsolidation pressure and  $M_{cs}$  is the slope of critical state line, see Fig. 3.3. Note that Eq. (3.12) represents a yield surface of the modified Cam clay model proposed in [31]. Its main advantage, apart from the ability to describe (at least qualitatively) the real response of clays (particularly those found in lightly overconsolidated state), is the simplicity in numerical implementation. In its original format the full surface is a surface of revolution about the  $J$ -axis thus giving a circular yield surface in the deviatoric plane. The allowable region for the material point to undergo only an elastic response depends solely on the value of  $M_{cs}$ , which is assumed to be constant depending on the value of critical state angle  $\varphi_{cs}$ . As for the Drucker-Prager model it ranges between the values

$$M_{cs}^{+30^\circ}(\varphi_{cv}) = \frac{2\sqrt{3} \sin \varphi_{cv}}{3 - \sin \varphi_{cv}} \quad \text{for triaxial compression,} \quad (3.13)$$

$$M_{cs}^{-30^\circ}(\varphi_{cv}) = \frac{2\sqrt{3} \sin \varphi_{cv}}{3 + \sin \varphi_{cv}} \quad \text{for triaxial extension.} \quad (3.14)$$

With reference to Eq. (3.10) the size of the ellipse changes depending on the current

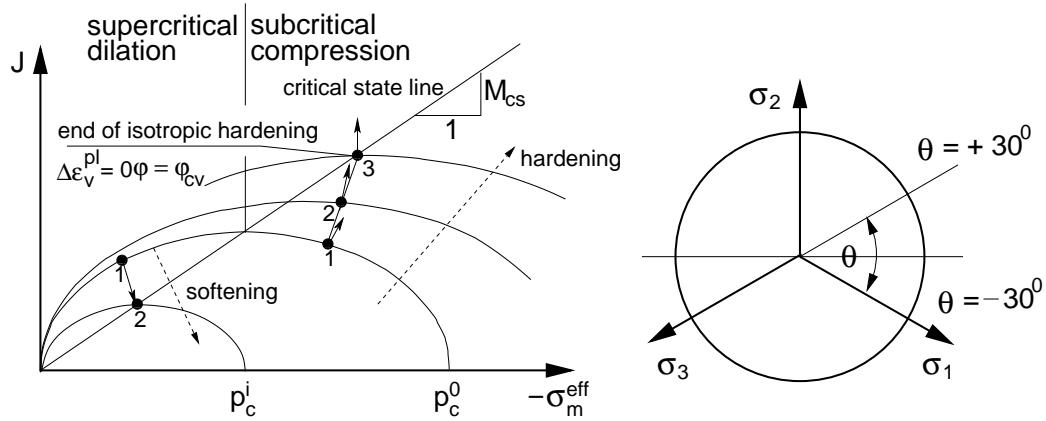


Figure 3.3: Cam clay model – yield function

value of the preconsolidation pressure  $p_c$ . For the material found on the subcritical side the yield surface expands with the direction of plastic strain normal to the yield surface (associated plasticity is assumed) until the point of intersection with the critical state line is reached. At this point (point 3 in Fig. 3.3), the normal to the yield surface is vertical thus no plastic volumetric strain is predicted at this point. Hence, all the plastic strain is distortional. When further sheared under constant volume, the material point behaves as rigid plastic with no change in stress. Such a response is consistent with what is observed in reality. When on the supercritical side, the constitutive model predicts softening. The amount of softening, however, is too excessive when compared to real soil behavior. In addition, for highly overconsolidated soils the model significantly overestimates the failure stresses. These drawbacks observed by many investigators led to the development of series of cam clay formulations in an attempt to modify the prediction of the clay response on the supercritical side. Mostly, combined yield surfaces were proposed. An overview of

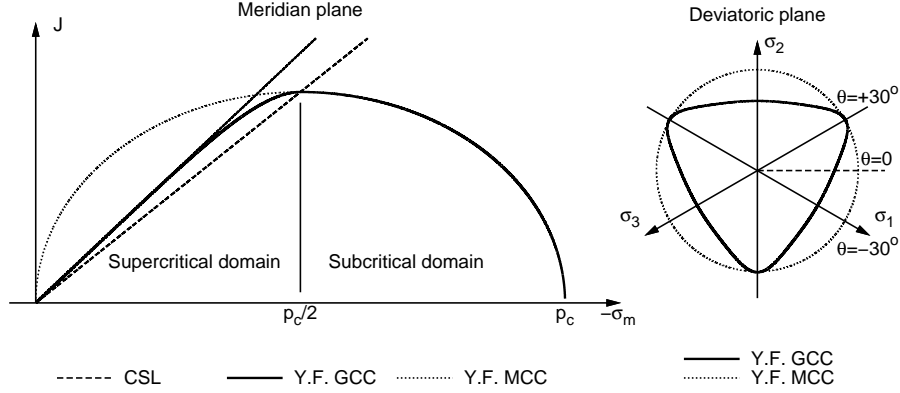


Figure 3.4: Generalized Cam clay model – yield function

several such models is presented in [29]. Another possible modification is suggested in the next section.

## 3.2 Generalized Cam clay model

In this section a modification to the original formulation of the modified Cam clay model is examined. In particular, to overcome several drawbacks of the original model a new model here termed the generalized Cam clay model is proposed. Similar to existing formulations the yield function is composed of two smoothed functions continuously connected at the point of intersection with the critical state line. Graphical representation is displayed in Fig. 3.4. Mathematically, the two functions assume the form

$$F(\boldsymbol{\sigma}, \boldsymbol{\kappa}) = \begin{cases} F_c, & \text{pro } \sigma_m \leq -p_c/2 \quad (\text{subcritical side}), \\ F_d, & \text{pro } \sigma_m > -p_c/2 \quad (\text{supercritical side}), \end{cases} \quad (3.15)$$

$$F_c = \frac{J^2}{g^2(\theta, \varphi_{cv})} + \sigma_m^2 + \sigma_m p_c, \quad (3.16)$$

$$F_d = \frac{J^2}{g^2(\theta, \varphi_{cv})} - \beta \left[ \sigma_m^2 - \left( -\frac{\sigma_m}{\gamma p_c} \right)^{1+\alpha} (\gamma p_c)^2 \right], \quad (3.17)$$

where parameters  $\alpha, \beta, \gamma$  are defined such as to give a vertical normal to the yield surface at the joint point of the two functions on the one hand and to maintain compatibility of both yield functions for any value of Lode's angle  $\theta$ . At zero deviatoric stress  $J$  they suggest a common tangent of the function  $F_d$  with the Modified Mohr-Coulomb model, see Fig. 3.4 where the values of  $\tilde{g}(\theta, \varphi_{cv}, \varphi)$  and  $\tilde{p}_c(\varphi, \varphi_{cv})$  are given by

$$\tilde{g}(\theta, \varphi_{cv}, \varphi) = g(\theta, \varphi_{cv}) \sqrt{\beta(\varphi, \varphi_{cv})}, \quad (3.18)$$

$$\tilde{p}_c(\varphi, \varphi_{cv}) = \gamma(\varphi, \varphi_{cv}) p_c. \quad (3.19)$$



These are

$$\alpha = \frac{\beta + 1}{\beta - 1}, \quad (3.20)$$

$$\beta = \left( \frac{\sin \varphi}{\sin \varphi_{cv}} \frac{3 - \sin \varphi_{cv}}{3 - \sin \varphi} \right)^2, \quad (3.21)$$

$$\gamma = \left( \frac{2^\alpha}{1 + \alpha} \right)^{\frac{1}{1-\alpha}}, \quad (3.22)$$

where  $\varphi$  is the peak value of the angle of internal friction also being the only new parameter in the proposed model. Note that no changes are introduced on the subcritical side. The smooth transition from one surface to the other not only considerably simplifies the numerical implementation, but also ensures fulfilling the critical state condition already predicted by the modified Cam clay model. Furthermore, the model also predicts a unique state boundary surface and the consolidation/swelling behavior. Unlike for the modified Cam clay model, the swelling behavior and the failure stresses, in particular, are considerably suppressed. Such a behavior is in better accordance with reported experimental results.

Further modification arises when introducing a non-circular yield surface in the deviatoric plane. Such a step has been put forward in [29] owing to the fact that a circle does not represent well the failure conditions for soils. With reference to works of Lade and Kim&Lade [20, 18, 21], Matsuoka&Nakai [26], Van Eekelen [9], to cite a few, a smoothed triangle for a yield surface in the deviatoric plane is adopted. On the subcritical side the constant value of  $M_{cs}$  is replaced by the function  $g$  already introduced for the modified Mohr-Coulomb plasticity model in Section 2.3.5

$$g(\theta, \varphi_{cv}) = X(Y_1 + Y_2 \sin 3\theta)^{-Z}, \quad (3.23)$$

$$X = 2^{(Z+1)} \sqrt{3} \sin \varphi_{cv}, \quad (3.24)$$

$$Y_1 = (3 - \sin \varphi_{cv})^{\frac{1}{Z}} + (3 + \sin \varphi_{cv})^{\frac{1}{Z}}, \quad (3.25)$$

$$Y_2 = (3 - \sin \varphi_{cv})^{\frac{1}{Z}} - (3 + \sin \varphi_{cv})^{\frac{1}{Z}}. \quad (3.26)$$

To reduce complexity on the implementation part a non-associated plasticity is assumed with a circular shape of the plastic potential in the deviatoric plane, see also discussion in Section 2.3.5 on the choice of the shape of yield surface and plastic potential in the deviatoric plane. In summary, the proposed model requires specification of six independent parameters. The bilinear diagram of isotropic consolidation is determined through material constants  $\kappa, \lambda, e_0$  and the current value of preconsolidation pressure  $p_c$ . The yield surface and plastic potential are fully described by parameters  $\varphi, \varphi_{cv}$  and  $p_c$ .

### 3.3 Numerical integration - stress update procedure

A fully implicit Euler backward integration scheme for integration of the resulting system of rate equations as proposed, e.g. by Borja [3] and further developed by Groen [11] is

adopted. A specific form of implicit integration scheme, also implemented in the program GEO FEM, is presented in subsequent sections for both the modified and generalized Cam clay model.

### 3.3.1 Modified Cam clay model

With the help of Eq. (2.2) the yield function given by Eq. (3.12) attains the following form

$$F = \frac{1}{2} \frac{\boldsymbol{\sigma}^T \mathbf{P} \boldsymbol{\sigma}}{M_{cs}^2} + (\mathbf{m}^T \boldsymbol{\sigma})^2 + \mathbf{m}^T \boldsymbol{\sigma} p_c. \quad (3.27)$$

Next, assuming the associated flow rule the increments of plastic volumetric  $\varepsilon_v^{pl}$  and deviatoric  $\mathbf{e}^{pl}$  strains follow from

$$\Delta \varepsilon_v^{pl} = \Delta \lambda \frac{\partial F}{\partial \sigma_m} = \Delta \lambda (2\sigma_m + p_c), \quad (3.28)$$

$$\Delta \mathbf{e}^{pl} = \Delta \lambda \frac{\partial F}{\partial \mathbf{s}} = \Delta \lambda \frac{\mathbf{P} \boldsymbol{\sigma}}{M_{cs}^2} = \Delta \lambda \frac{\mathbf{Q}^{-1} \mathbf{s}}{M_{cs}^2}, \quad (3.29)$$

which gives the increment of total plastic strain vector in the form

$$\Delta \boldsymbol{\varepsilon}^{pl} = \Delta \lambda \left[ \frac{\mathbf{P} \boldsymbol{\sigma}}{M_{cs}^2} + (2\sigma_m + p_c) \mathbf{m} \right], \quad (3.30)$$

where  $\Delta \lambda$  represents an increment of plastic multiplier and  $\mathbf{s}$  is the deviatoric stress vector. Next, recall Eq. (3.11) and write the increment of effective mean stress as

$$\Delta \sigma_m = \sigma_m^{i+1} - \sigma_m^i = \sigma_m^i \left( \exp \left[ \frac{-\Delta \varepsilon_v^{el}}{\kappa^*} \right] - 1 \right) = K_s \Delta \varepsilon_v^{el}. \quad (3.31)$$

Noting that

$$\Delta \varepsilon_v^{el} = \Delta \varepsilon_v - \Delta \lambda (2\sigma_m^{i+1} + p_c^{i+1}), \quad (3.32)$$

provides the secant bulk modulus  $K_s$  as a function of the current stress state in the form

$$K_s^{i+1} = \sigma_m^i \frac{\exp \left( -\frac{\Delta \varepsilon_v - \Delta \lambda (2\sigma_m^{i+1} + p_c^{i+1})}{\kappa^*} \right) - 1}{\Delta \varepsilon_v - \Delta \lambda (2\sigma_m^{i+1} + p_c^{i+1})}. \quad (3.33)$$

Using a standard predictor corrector procedure together with Eq. (3.29), the deviatoric stress at the end of the current load increment is provided by

$$\mathbf{s}^{i+1} = \frac{\mathbf{s}^i + 2G_s^{i+1} \mathbf{Q} \Delta \mathbf{e}}{1 + \frac{2G_s^{i+1} \Delta \lambda}{M_{cs}^2}}, \quad (3.34)$$

where the secant shear modulus  $G_s$  is usually written assuming a constant Poisson ratio  $\nu$  as

$$G_s = \frac{3(1-2\nu)}{2(1+\nu)} K_s. \quad (3.35)$$

The analysis that properly accounts for the variation of elastic moduli, Eqs. (3.33) and (3.35), is often called *variable elasticity* return mapping, while an analysis that keeps the elastic moduli constant over the current strain increment is referred to as *constant elasticity* return mapping [29]. In the latter case Eq. (3.11) simplifies to

$$\sigma_m^{i+1} = \frac{\sigma_m^i + K(\Delta\varepsilon_v - \Delta\lambda p_c^{i+1})}{1 + 2K\Delta\lambda}, \quad (3.36)$$

where the bulk modulus  $K$  is no longer stress dependent. Finally, the variable hardening/softening modulus follows from the consistency condition given by Eq. (2.18). Since preconsolidation pressure  $p_c(\kappa = \varepsilon_v^{pl})$  is the only hardening parameter we get, when employing Eq. (2.19),

$$\frac{\partial F}{\partial \kappa} = \frac{\partial F}{\partial \varepsilon_v^{pl}} = \frac{\partial F}{\partial p_c} \frac{\partial p_c}{\partial \varepsilon_v^{pl}} = -\frac{\sigma_m p_c}{\lambda^* - \kappa^*}, \quad (3.37)$$

so that the plastic modulus  $H$  reads

$$H = (2\sigma_m + p_c) \frac{\sigma_m p_c}{\lambda^* - \kappa^*}. \quad (3.38)$$

*Implicit integration scheme for variable elasticity return mapping*

Assuming variable elasticity return mapping driven by Eqs. (3.10), (3.11) and (3.33)-(3.34) gives the following set of residuals  $\{\mathbf{r}\}^\top = \{\mathcal{S}, \mathcal{P}, \mathcal{F}\}$  to be minimized simultaneously

$$\left\{ \begin{array}{c} \mathcal{S} \\ \mathcal{P} \\ \mathcal{F} \end{array} \right\} = \left\{ \begin{array}{c} \sigma_m^{i+1} - \sigma_m^i \exp \left[ -\frac{1}{\kappa^*} \{ \Delta\varepsilon_v - \Delta\lambda (2\sigma_m^{i+1} + p_c^{i+1}) \} \right] \\ p_c^{i+1} - p_c^i \exp \left[ -\frac{\Delta\lambda}{\lambda^* - \kappa^*} (2\sigma_m^{i+1} + p_c^{i+1}) \right] \\ \frac{(J^{i+1})^2}{M_{cs}^2} + (\sigma_m^{i+1})^2 + \sigma_m^{i+1} p_c^{i+1} \end{array} \right\}, \quad (3.39)$$

for the vector of unknown primary variables  $\{\mathbf{a}\}^\top = \{\sigma_m^{i+1}(\Delta\lambda, p_c^{i+1}), p_c^{i+1}(\Delta\lambda, \sigma_m^{i+1}), \Delta\lambda\}$ . See also [11] for further details. Usually, the Newton-Raphson (N-R) method is called to minimize the set of residuals (3.39). At each local N-R iteration step the instantaneous values of  $J^{i+1} = \sqrt{\frac{1}{2} \mathbf{s}^{i+1 \top} \mathbf{Q}^{-1} \mathbf{s}^{i+1}}$  and  $G^{i+1}$  follow from Eqs. (3.34) and (3.35). Note that during the N-R iteration the condition  $\Delta\boldsymbol{\varepsilon} = \text{const}$  is adopted. Thus for the system of nonlinear algebraic equations the  $k$ th iteration of the N-R scheme assumes the form

$$\{\mathbf{a}^{i+1}\}_{k+1} = \{\mathbf{a}^{i+1}\}_k - [\mathbf{H}]^{-1} \{\mathbf{r}\}_k. \quad (3.40)$$

The  $3 \times 3$  Jacobian matrix  $[\mathbf{H}]$  reads

$$[\mathbf{H}] = \left[ \frac{\partial \mathbf{r}}{\partial \mathbf{a}} \right]^\top + \left\{ \frac{\partial \mathbf{r}}{\partial J} \right\} \left\{ \frac{\partial J(\Delta\lambda, G_s(\sigma_m, p_c, \Delta\lambda))}{\partial \mathbf{a}} \right\}^\top, \quad (3.41)$$

$$= \left[ \begin{array}{ccc} \frac{\partial S}{\partial \sigma_m} & \frac{\partial S}{\partial p_c} & \frac{\partial S}{\partial \Delta\lambda} \\ \frac{\partial P}{\partial \sigma_m} & \frac{\partial P}{\partial p_c} & \frac{\partial P}{\partial \Delta\lambda} \\ \frac{\partial F}{\partial \sigma_m} + \frac{\partial F}{\partial J} \frac{\partial J}{\partial G_s} \frac{\partial G_s}{\partial \sigma_m} & \frac{\partial F}{\partial p_c} + \frac{\partial F}{\partial J} \frac{\partial J}{\partial G_s} \frac{\partial G_s}{\partial p_c} & \frac{\partial F}{\partial J} \left( \frac{\partial J}{\partial \Delta\lambda} + \frac{\partial J}{\partial G_s} \frac{\partial G_s}{\partial \Delta\lambda} \right) \end{array} \right].$$

To complete the return mapping, it is assumed that the initial conditions for the solution of Eq. (3.40) are defined by the elastic trial stress so that

$$\{\mathbf{a}_0\}^\top = \{\sigma_m^{\text{tr}}, p_c^i, 0\}, \quad (3.42)$$

$$\{\mathbf{r}_0\}^\top = \left\{0, 0, \frac{(J^{\text{tr}})^2}{M_{cs}^2} + (\sigma_m^{\text{tr}})^2 + \sigma_m^{i+1} p_c^{\text{tr}}\right\}. \quad (3.43)$$

where the trial stresses  $\sigma_m^{\text{tr}}, \mathbf{s}^{\text{tr}}$  are provided by

$$\sigma_m^{\text{tr}} = \sigma_m^i + K_s^i \Delta \varepsilon_v. \quad (3.44)$$

$$\mathbf{s}^{\text{tr}} = \mathbf{s}^i + 2\mathbf{Q}G_s^i \Delta \mathbf{e}. \quad (3.45)$$

*Implicit integration scheme for constant elasticity return mapping*

The solution of the nonlinear system of equations considerably simplifies when *constant elasticity* return mapping is adopted. In such a case the stress variables required at the end of a given load increment are

$$\sigma_m^{i+1} = \frac{\sigma_m^{\text{tr}} - K^i \Delta \lambda p_c^{i+1}}{1 + 2K^i \Delta \lambda}, \quad (3.46)$$

$$\mathbf{s}^{i+1} = \frac{\mathbf{s}^{\text{tr}}}{1 + \frac{2G^i \Delta \lambda}{M_{cs}^2}}, \quad (3.47)$$

$$J^{i+1} = \frac{J^{\text{tr}}}{1 + \frac{2G^i \Delta \lambda}{M_{cs}^2}}, \quad (3.48)$$

where the *trial* stress components follow from Eqs. (3.44)-(3.45) and the elastic moduli  $K^i, G^i$  are taken at the beginning of integration step. They can be determined from Eqs. (3.4), (3.31) and (3.35)

$$K^i = -\frac{\sigma_m^i}{\kappa^*}, \quad (3.49)$$

$$G^i = \frac{3(1-2\nu)}{2(1+\nu)} K^i. \quad (3.50)$$

The resulting system of implicit nonlinear algebraic equations then reduces to

$$\mathcal{P} = p_c^{i+1} - p_c^i \exp \left[ -\frac{\Delta \lambda}{\lambda^* - \kappa^*} \frac{2\sigma_m^{\text{tr}} + p_c^{i+1}}{1 + 2K^i \Delta \lambda} \right] = 0, \quad (3.51)$$

$$\mathcal{F} = \frac{(J^{i+1})^2}{M_{cs}^2} + (\sigma_m^{i+1})^2 + \sigma_m^{i+1} p_c^{i+1} = 0. \quad (3.52)$$

This set of equations can be solved applying the same procedure as discussed for the *variable elastic* return mapping. Clearly, adopting the described implicit integration algorithm directly accounts for the yield strength dependent evolution of plastic flow direction as typical for both the modified and generalized Cam clay models.

### 3.3.2 Generalized Cam clay model

To keep formal similarity with the previous section we start by writing the yield functions in the form of Eq. (3.27) to get

$$F_c = \frac{1}{2} \frac{\boldsymbol{\sigma}^T \mathbf{P} \boldsymbol{\sigma}}{g^2(\theta, \varphi_{cv})} + (\mathbf{m}^T \boldsymbol{\sigma})^2 + \mathbf{m}^T \boldsymbol{\sigma} p_c, \quad (3.53)$$

$$F_d = \frac{1}{2} \frac{\boldsymbol{\sigma}^T \mathbf{P} \boldsymbol{\sigma}}{g^2(\theta, \varphi_{cv})} - \beta \left[ (\mathbf{m}^T \boldsymbol{\sigma})^2 - \left( -\frac{\mathbf{m}^T \boldsymbol{\sigma}}{\gamma p_c} \right)^{1+\alpha} (\gamma p_c)^2 \right]. \quad (3.54)$$

As already suggested in Section 3.2 a non-associated plastic flow is assumed with the circular shape of plastic potential in the deviatoric plane. Such functions are obtained by replacing Lode's angle dependent function  $g(\theta, \varphi_{cv})$  in Eq. (3.23) with a new function  $g_G(\theta_c, \varphi_{cv})$ , where  $\theta_c$  represents Lode's angle at the point in stress space at which the gradients of the plastic potential are required [29], see also Section 2.3.4 and Fig. 2.5 for the definition of plastic potential. Recall that the current stress point has to reside not only on the yield, but also on the plastic potential surface. Therefore

$$G_c = \frac{1}{2} \frac{\boldsymbol{\sigma}^T \mathbf{P} \boldsymbol{\sigma}}{g_G^2(\theta_c, \varphi_{cv})} + (\mathbf{m}^T \boldsymbol{\sigma})^2 + \mathbf{m}^T \boldsymbol{\sigma} p_c, \quad (3.55)$$

$$G_d = \frac{1}{2} \frac{\boldsymbol{\sigma}^T \mathbf{P} \boldsymbol{\sigma}}{g_G^2(\theta_c, \varphi_{cv})} - \beta \left[ (\mathbf{m}^T \boldsymbol{\sigma})^2 + \left( -\frac{\mathbf{m}^T \boldsymbol{\sigma}}{\gamma p_c} \right)^{1+\alpha} (\gamma p_c)^2 \right]. \quad (3.56)$$

To derive the elasto-plastic tangent stiffness matrix from Eq. (2.48) the differentials defining the normals to the yield and plastic potential surfaces together with the hardening modulus  $H$  are needed. Employing Eqs. (2.34) provides

$$\mathbf{n}_c = \frac{\partial F_c}{\partial \boldsymbol{\sigma}} = \frac{1}{g^2} \mathbf{P} \boldsymbol{\sigma} + 2 \mathbf{m}^T \boldsymbol{\sigma} \mathbf{m} + p_c \mathbf{m} - \frac{2J}{g^3} \frac{\partial g}{\partial \boldsymbol{\sigma}}, \quad (3.57)$$

$$\mathbf{n}_d = \frac{\partial F_d}{\partial \boldsymbol{\sigma}} = \frac{1}{g^2} \mathbf{P} \boldsymbol{\sigma} - \beta \left[ 2 \mathbf{m}^T \boldsymbol{\sigma} \mathbf{m} + (1 + \alpha) \left( -\frac{\mathbf{m}^T \boldsymbol{\sigma}}{\gamma p_c} \right)^\alpha \gamma p_c \mathbf{m} \right] - \frac{2J}{g^3} \frac{\partial g}{\partial \boldsymbol{\sigma}}, \quad (3.58)$$

$$\mathbf{n}_{Gc} = \frac{\partial G_c}{\partial \boldsymbol{\sigma}} = \frac{1}{g_G^2} \mathbf{P} \boldsymbol{\sigma} + 2 \mathbf{m}^T \boldsymbol{\sigma} \mathbf{m} + p_c \mathbf{m}, \quad (3.59)$$

$$\mathbf{n}_{Gd} = \frac{\partial G_d}{\partial \boldsymbol{\sigma}} = \frac{1}{g_G^2} \mathbf{P} \boldsymbol{\sigma} - \beta \left[ 2 \mathbf{m}^T \boldsymbol{\sigma} \mathbf{m} + (1 + \alpha) \left( -\frac{\mathbf{m}^T \boldsymbol{\sigma}}{\gamma p_c} \right)^\alpha \gamma p_c \mathbf{m} \right]. \quad (3.60)$$

where, e.g. the term  $\frac{\partial g}{\partial \boldsymbol{\sigma}} = \frac{\partial g}{\partial \theta} \frac{\partial \theta}{\partial \boldsymbol{\sigma}}$  can be obtained from Eqs. (2.86)-(2.87). To derive the desired variable plastic hardening/softening modulus  $H$  we follow the steps described in the previous section starting again from the consistency condition (2.18) to get

$$H_d = -\frac{dF_d}{d\varepsilon_{vd}^{pl}} \frac{d\varepsilon_{vd}^{pl}}{d\Delta\lambda}, \quad (3.61)$$

where

$$\begin{aligned}\frac{d\varepsilon_{vd}^{pl}}{d\Delta\lambda} &= \frac{\partial F_d}{\partial\sigma_m} = -2\beta\sigma_m - \beta(1+\alpha) \left(-\frac{\sigma_m}{\gamma p_c}\right)^\alpha \gamma p_c, \\ \frac{dF_d}{d\varepsilon_{vd}^{pl}} &= \frac{\partial F}{\partial p_c} \frac{\partial p_c}{\partial \varepsilon_v^{pl}} = -\beta\gamma(1-\alpha) \left(-\frac{\sigma_m}{\gamma p_c}\right)^{1+\alpha} \gamma p_c \times \frac{p_c}{\lambda^* - \kappa^*}.\end{aligned}$$

When the stress point is found on the compaction (subcritical) side the modulus  $H_c$  attains the form given by Eq. (3.38).

As for the plastic strain increments it is worth to note that no multi-surface plasticity concept is needed. This is attributed to the fact that only a single plastic flow either on dilation or compaction side can be active and at their joint point both flows predict the same critical state with no volume change. Therefore, owing to the assumed non-associated plasticity the respective plastic strain increments are given in the form

$$\Delta\varepsilon_{vc}^{pl} = \Delta\lambda \frac{\partial G_c}{\partial\sigma_m} = \Delta\lambda (2\sigma_m + p_c), \quad (3.62)$$

$$\Delta\varepsilon_{vd}^{pl} = \Delta\lambda \frac{\partial G_d}{\partial\sigma_m} = \Delta\lambda\beta \left[ -2\sigma_m - (1+\alpha) \left(-\frac{\sigma_m}{\gamma p_c}\right)^\alpha \gamma p_c \right], \quad (3.63)$$

$$\Delta\mathbf{e}_c^{pl} = \Delta\lambda \frac{\partial G_c}{\partial\mathbf{s}} = \Delta\lambda \frac{\mathbf{P}\boldsymbol{\sigma}}{g_G^2}, \quad (3.64)$$

$$\Delta\mathbf{e}_d^{pl} = \Delta\lambda \frac{\partial G_d}{\partial\mathbf{s}} = \Delta\lambda \frac{\mathbf{P}\boldsymbol{\sigma}}{g_G^2}. \quad (3.65)$$

The current stresses and instantaneous secant bulk modulus  $K$  then follow from equations listed in Section 3.3.1 when applying specific forms of Eqs. (3.62)-(3.65).

#### *Implicit integration scheme for variable elasticity return mapping*

The general scheme of the stress update procedure was already presented in Section 3.3.1. Hereafter, we thus limit our attention only to specific differences that arise from the definition of the functions  $F_c, F_d$ . In particular, inspecting Eqs. (3.39)-(3.45) suggests

that the only difference appears in certain entries of the Jacobian matrix  $H$ , which are

$$H_{31} = \frac{\partial F}{\partial \sigma_m} + \frac{\partial F}{\partial J} \frac{\partial J}{\partial G_s} \frac{\partial G_s}{\partial \sigma_m} + \frac{\partial F}{\partial g} \frac{\partial g}{\partial \sin 3\theta} \left( \frac{\partial \sin 3\theta}{\partial J} \frac{\partial J}{\partial G_s} \frac{\partial G_s}{\partial \sigma_m} + \frac{\partial \sin 3\theta}{\partial I_{3s}} \left\{ \frac{\partial I_{3s}}{\partial \mathbf{s}} \right\}^T \left\{ \frac{\partial \mathbf{s}}{\partial G_s} \right\} \frac{\partial G_s}{\partial \sigma_m} \right), \quad (3.66)$$

$$H_{32} = \frac{\partial F}{\partial p_c} + \frac{\partial F}{\partial J} \frac{\partial J}{\partial G_s} \frac{\partial G_s}{\partial p_c} + \frac{\partial F}{\partial g} \frac{\partial g}{\partial \sin 3\theta} \left( \frac{\partial \sin 3\theta}{\partial J} \frac{\partial J}{\partial G_s} \frac{\partial G_s}{\partial p_c} + \frac{\partial \sin 3\theta}{\partial I_{3s}} \left\{ \frac{\partial I_{3s}}{\partial \mathbf{s}} \right\}^T \left\{ \frac{\partial \mathbf{s}}{\partial G_s} \right\} \frac{\partial G_s}{\partial p_c} \right), \quad (3.67)$$

$$H_{33} = \frac{\partial F}{\partial J} \left( \frac{\partial J}{\partial \Delta\lambda} + \frac{\partial J}{\partial G_s} \frac{\partial G_s}{\partial \Delta\lambda} \right) + \frac{\partial F}{\partial g} \frac{\partial g}{\partial \sin 3\theta} \left( \frac{\partial \sin 3\theta}{\partial J} \left[ \frac{\partial J}{\partial \Delta\lambda} + \frac{\partial J}{\partial G_s} \frac{\partial G_s}{\partial \Delta\lambda} \right] + \frac{\partial \sin 3\theta}{\partial I_{3s}} \left\{ \frac{\partial I_{3s}}{\partial \mathbf{s}} \right\}^T \left[ \left\{ \frac{\partial \mathbf{s}}{\partial \Delta\lambda} \right\} + \left\{ \frac{\partial \mathbf{s}}{\partial G_s} \right\} \frac{\partial G_s}{\partial \Delta\lambda} \right] \right), \quad (3.68)$$

where  $F = F_c(\varphi_{cv})$  when referring to subcritical side, while  $F = F_d(\varphi, \varphi_{cv})$  when the flow controlled by function  $F_d$  is active. Recall that  $G_s$  is the instantaneous secant shear modulus.

### 3.3.3 Note on numerical implementation

An important issue which requires our attention is the determination of initial preconsolidation pressure  $p_c^{in}$  and associated initial bulk modulus  $K^{in}$ . Recall that these two parameters are not included in the standard material setting of the modified or generalized Cam clay model in the program GEO FEM. Instead, their distributions are derived on the basis of the assumed geostatic stress profile.

The distribution of initial geostatic stress in GEO FEM is always calculated in the first construction stage. The user may choose from the following three options:

- $K_o$  procedure

The  $K_o$  procedure is described in detail in the second part of this manuscript suggesting the initial mean stress in the form

$$\sigma_m = \frac{1}{3} \gamma h (1 + 2K_o), \quad (3.69)$$

where  $K_o$  is the coefficient of lateral earth pressure at rest,  $\gamma$  is the bulk unit weight,  $\nu$  is the Poisson ratio and  $h$  is the actual depth of a stress point in the soil profile. If we assume that the clay did not experience greater vertical stresses in the past (normally consolidated clay) then the value of initial preconsolidation pressure is determined for the current stress to sit on the yield surface. This gives for the modified Cam clay model

$$p_c^{in} = -\frac{J^2}{M_{cs}^2 \sigma_m} - \sigma_m. \quad (3.70)$$

For overconsolidated clays the value of  $p_c^{in}$  is further adjusted to get

$$p_c^{in} = p_c^{in} OCR, \quad (3.71)$$

where  $OCR$  is the overconsolidation ratio. The initial bulk modulus then follows directly from Eq. (3.49)

$$K^{in} = -\frac{1+e}{\kappa} \sigma_m, \quad (3.72)$$

where the current void ratio  $e$  reads

$$e = e_0 - \lambda \ln(p_c^{in}) + \kappa \ln\left(-\frac{p_c^{in}}{\sigma_m}\right). \quad (3.73)$$

Recall that  $e_0$  represents the minimum void ratio on virgin consolidation line at  $p_c = 1$ . For small stresses  $|\sigma_m| < 1$  the following initial conditions are considered

$$p_c^{in} = 1, \quad K^{in} = -\frac{1+e_0}{\kappa}. \quad (3.74)$$

- Elastic analysis

Note that the program GEO FEM allows us to switch from one material model to another between two construction stages. This option can therefore be exploited in



cases where  $K_o$  procedure is not applicable. In particular, the soil to be represented by one of the two Cam clay models is assumed to follow a linear Hooke's law in the first construction stage. The corresponding initial stress conditions are then used in Eqs. (3.70) - (3.74) in place of Eq. (3.69) to derive the desired distributions of  $p_c^{in}$  and  $K^{in}$ . From the second construction stage the linear elastic model is substituted by an appropriate plastic one to obtain more realistic predictions of the soil behavior.

- Plastic analysis

The plastic analysis involves plastic material models for clayey soils already in the first constructions stage. During calculation, the soil is thus assumed to move down the virgin consolidation line with the initial values of  $p_c^{in}$  and  $K^{in}$  given by Eq. (3.74). Subsequently, overconsolidated soils are adjusted using Eq. (3.71). All plastic deformations that arise during the first calculation stage are set equal to zero before resuming any further calculations.

### 3.3.4 Note on determination of parameters $\kappa$ and $\lambda$

Our experience indicates that unlike Young's modulus or Poisson's ratio the swelling modulus  $\kappa$  and the compression modulus  $\lambda$  in particular are, however, unknown to majority of practical users. This is also why the critical state models still receive much less attention in comparison with rather classical Mohr-Coulomb like models.

As suggested in [16] a simple one-dimensional consolidation test can be used to derive most of the required parameters through the solution of a certain inverse problem. Although relatively straightforward, this approach will nevertheless prove viable only if handled by another commercial software, which to our knowledge is currently not available.

Consequently, standard oedometer tests still appear as the most appropriate investigation at least from the practical users point of view. To establish a link between the  $\kappa$  and  $\lambda$  moduli and the corresponding parameters derived from oedometer tests is therefore the main issue of this section.

It is well known that the complete stress state of a sample in the oedometer apparatus is not known. Unlike the triaxial apparatus the oedometer apparatus provides only the axial stress  $\sigma_y$  (see Fig. 1.1 for the selected coordinate system) and the total volumetric strain  $\varepsilon_v$  equal to the axial strain  $\varepsilon_y$ . Assuming undrained conditions the results from oedometer tests are often plotted in terms of  $e - \log(-\sigma_y)$  diagram, see Fig. 3.5(a). This graph is very similar to  $e - \ln(-\sigma_m)$  diagram plotted in Fig. 3.1. Owing to the geometrical constraints imposed by a standard oedometer apparatus the slope of the virgin consolidation line is called the one-dimensional compression index written as

$$C_c = \frac{\Delta e}{\Delta \log(-\sigma_y)} = \frac{\Delta e}{\log \frac{\sigma_y^{i+1}}{\sigma_y^i}}. \quad (3.75)$$

To bring the compression modulus  $\lambda$  and the one-dimensional compression index  $C_c$  to the same footing we introduce the coefficient of lateral earth pressure at rest for normally

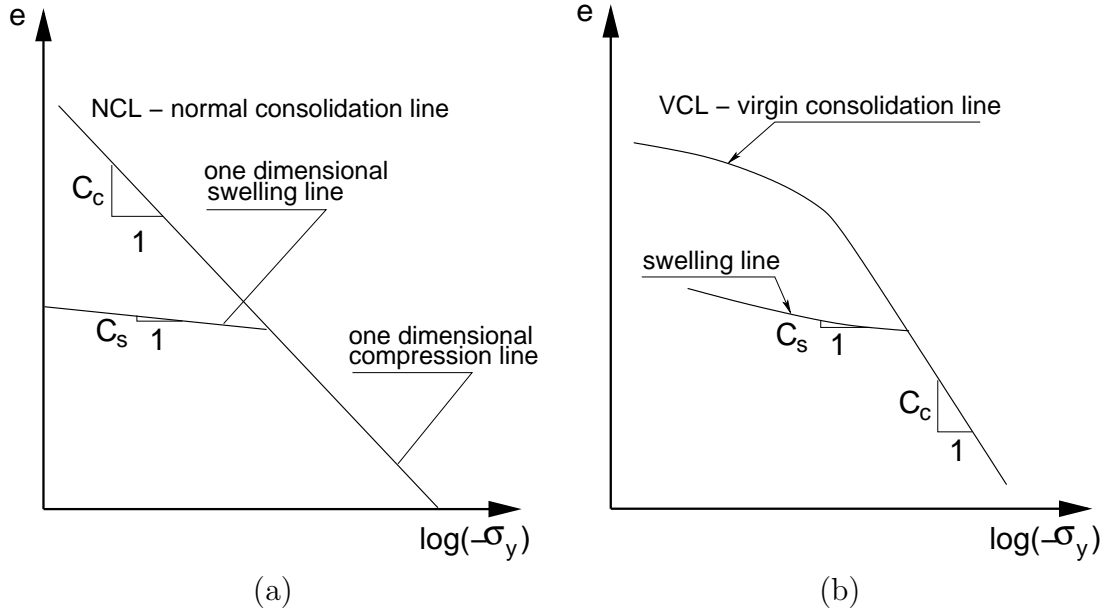


Figure 3.5: Behavior under one dimensional compression: a) idealization, b) typical result of an oedometric test

consolidated soils  $K_o^{NC}$  and write the effective mean stress as

$$\sigma_m = \frac{1}{3}(1 + 2K_o^{NC})\sigma_y. \quad (3.76)$$

Note that  $K_o^{NC}$  is often estimated from Jaky's formula  $K_o^{NC} = 1 - \sin \varphi$ , where  $\varphi$  is the effective angle of internal friction. Since  $K_o^{NC}$  is approximately constant along the virgin compression line [30, Chapter 1] we get, recall Eq. (3.1),

$$\lambda = \frac{\Delta e}{\Delta \ln(-\sigma_m)} = \frac{\Delta e}{\ln \frac{\sigma_m^{i+1}}{\sigma_m^i}} = \frac{\Delta e}{\ln \frac{\sigma_y^{i+1}}{\sigma_y^i}}. \quad (3.77)$$

Since  $\ln x = 2.3 \log x$  we get after comparing Eqs. (3.75) and (3.77)

$$\lambda = \frac{C_c}{2.3}. \quad (3.78)$$

Assuming that the swelling lines also plot as straight lines in both  $e - \ln(-\sigma_m)$  and  $e - \log(-\sigma_y)$  diagrams as shown in Figs. 3.1(a) and 3.5(a) gives similar approximation of the swelling modulus  $\kappa$  in terms of the swelling index  $C_s$  as

$$\kappa \approx \frac{C_s}{2.3}. \quad (3.79)$$

However, such an assumption is not valid in general. In fact,  $K_o$  is not constant along the swelling line but rather increases during unloading as schematically demonstrated in

Fig. 3.5(b). A modification to Eq. (3.79) is given in [24, Material model manual, Chapter 6]

$$\kappa \approx 3 \frac{1 - \nu_{ur}}{1 + \nu_{ur}} \frac{C_s}{2.3}, \quad (3.80)$$

where  $\nu_{ur}$  represents Poisson's ratio derived from the ratio of differences in the horizontal and vertical stress developed in oedometer during unloading and reloading

$$\Delta\sigma_x = \frac{\nu_{ur}}{1 - \nu_{ur}} \Delta\sigma_y = K_o \Delta\sigma_y. \quad (3.81)$$

With this definition it is easy to show that

$$3 \frac{1 - \nu_{ur}}{1 + \nu_{ur}} = \frac{3}{1 + 2K_o}. \quad (3.82)$$

However, neither of the two approximate relations for the swelling modulus  $\kappa$  are universally accepted and should therefore be used with considerable caution. Finally note that Eq. (3.80) reduces to Eq. (3.79) under incompressibility condition since for  $\nu_{ur} = 0.5$  the term  $3 \frac{1 - \nu_{ur}}{1 + \nu_{ur}} = 1$ .

# Chapter 4

## Constitutive models for structural elements

An important topic which needs to be addressed is concerned with the methods of supporting walls (props, ties, anchors) or reinforcing the soil body (geo-reinforcements). A two-node rod element with an axial stiffness but with no bending stiffness can be used to model horizontal struts, raking struts, geotextiles or node-to-node anchors. In general the element is used to model ties between two points in space. In the current implementation, such an element is considered to be a free element not necessarily connected to the underlying finite element mesh. Its deformation is realized by tying the free element nodes to the active nodes in the element mesh. This step is done automatically. This element can be subjected to both tensile forces (anchors, geo-reinforcements) and compressive forces (props). Allowable limits on the tensile as well as compressive force can be set to simulate element failure, e.g., anchor tensile failure or compressive failure of props due to buckling.

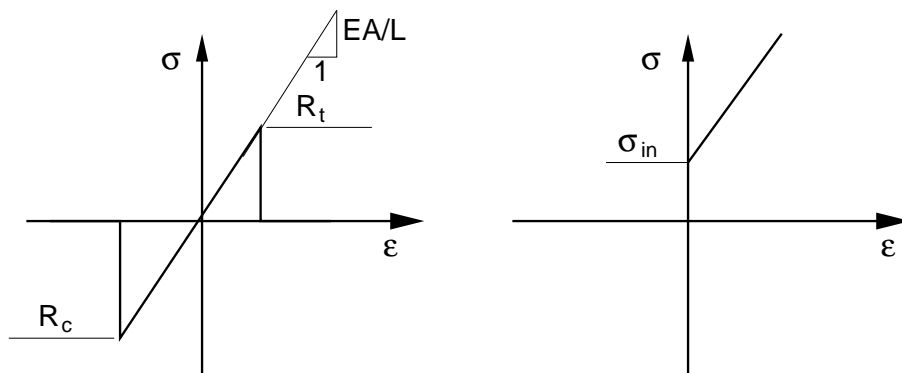


Figure 4.1: Constitutive model for anchors

The material behavior is limited to linear elasticity up to failure as shown in Fig. 4.1. The corresponding incremental stress-strain relationship assumes the form

$$\Delta\sigma = \frac{EA}{L}\Delta\epsilon + \Delta\sigma_{in}, \quad (4.1)$$

where  $E$  is Young's modulus,  $A$  represents the element cross-sectional area and  $L$  is the element length;  $\Delta\sigma_{in}$  stands for the initial stress increment associated with the initial anchor pre-stress given by

$$\Delta\sigma_{in} = \frac{\Delta F_{pre}}{A}, \quad (4.2)$$

where  $F_{pre}$  is the applied pre-stress force. Values  $R_t$  and  $R_c$  in Fig 4.1 correspond to allowable tensile and compressive strengths, respectively. Note that care must be taken when computing the axial element stiffness  $EA/L$  in plane strain applications as it should represent an equivalent axial stiffness per unit length that takes into account the element spacing in the out of plane direction.

As a default setting the element is assumed to sustain zero compressive stress. Thus, it is deactivated when in compression. But it can be reactivated again when subjected to tension. However, when the allowable strength limits are exceeded the element is automatically removed from the analysis. A few examples are now presented to simulate the application of individual structural elements.

## 4.1 Grout anchors

Structural applications often require modeling grout anchors that are in contact with a soil body along its entire length. Although geo-reinforcements discussed further in this section can be used in this regard, there is another, perhaps more appealing option allowing for gradual mobilization of the normal force in an anchor. This effect can be achieved by introducing, instead of one, a system of point-to-point anchors of different lengths. Such an approach gives further the possibility of representing gradual pull-out of an anchor when exceeding the limit shear strength by removing those anchors from the system, in which the maximum tensile strength is reached.

As an example, we consider a grout anchor represented by a system of four point-to-point (ground) anchors as shown in Fig. 4.2(d). The material stiffness of each anchor follows from a simple idea. To that end, consider a uniform distribution of interface shear stress along the anchor length, Fig. 4.2(a). Such an assumption then provides a linear distribution of normal force in the anchor, Fig. 4.2(b)

$$\begin{aligned} N(x) &= \tau_{pl}(l - x), \\ N_0 &= \tau_{pl}l, \end{aligned}$$

where  $N_0$  is the maximum normal force developed at the anchor starting point. In the program GEO FEM such a state can be approximated by introducing, e.g., four ground anchors to get the distribution plotted in Fig. 4.2(c). An augmented Young's modulus  $E^*$  of each anchor arrives from the condition of the same elongation of a real anchor and a substitute anchor tow

$$\begin{aligned} \Delta l &= \frac{1}{4} N'_0 \frac{l}{E^* A'} \quad - \text{model}, \\ \Delta l &= \frac{1}{2} N'_0 \frac{l}{EA'} \quad - \text{reality}, \end{aligned}$$

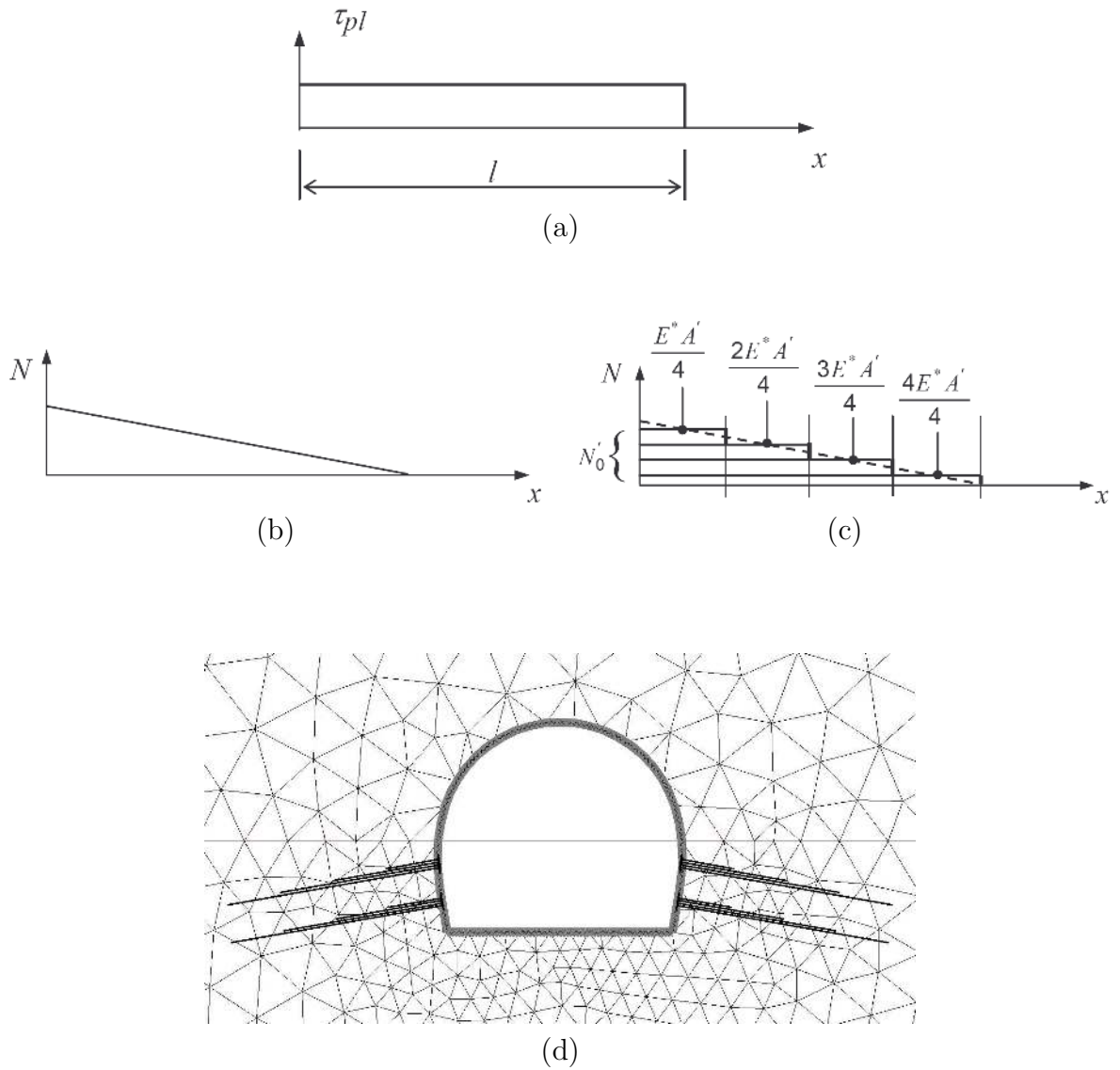


Figure 4.2: Modeling of anchors: (a) assumed constant shear, (b) linear normal force, (c) piecewise linear approximation, (d) application

so that

$$E^* = \frac{E}{2}.$$

The resulting maximum normal force is the given by

$$N'_0 = 4E^* A' \frac{\Delta l}{l}.$$

## 4.2 Geo-reinforcements

Geo-reinforcements are tensile reinforcing elements (geotextiles, geogrids) represented again by elastic bar elements and specified by their end points and axial stiffness. Unlike anchors, a geo-reinforcement is linked to an underlying finite element mesh along its entire length. However, similar to anchors the program introduces the geo-reinforcement end points into the finite element mesh automatically so it can be specified anywhere within the mesh.

The program allows for compressive forces to be transmitted in geo-reinforcement, Fig. 4.3(b). This option, however, should be used with caution. More appropriate models disable the part of geo-reinforcement found in compression for the analysis. Such a state is simulated in Fig. 4.3(c) showing the distribution of normal tensile forces over active parts of individual geo-reinforcements. The compressive part of a geo-reinforcement is excluded from the analysis. Similar to anchors, however, it can be automatically activated once loaded again in tension.

When introducing a geo-reinforcement into a soil body it is necessary to keep in mind a sufficient anchorage, since the program does not check the geo-reinforcement against shear failure. A sudden increase of the normal force as shown in Fig. 4.4(b) suggests singularity in contact stresses and probable shear failure of the geo-reinforcement. From that point of view the distribution displayed in Fig. 4.4(b) is misleading and essentially unrealistic. In such a case, the reinforcement should be either removed from the analysis or ensure its sufficient anchorage beyond the developed slip surface as plotted in Fig. 4.4(c).

## 4.3 Props

Props are supporting elements represented by an elastic bar element with constant normal stiffness. The props can sustain only compressive loading. When put into tension they are removed from the analysis. This is illustrated in Fig. 4.5. Similarly to anchors, the props are tied to the finite element mesh in only two points. If the prop is positioned into the soil, then no interaction between the soil and prop along the prop length is considered.

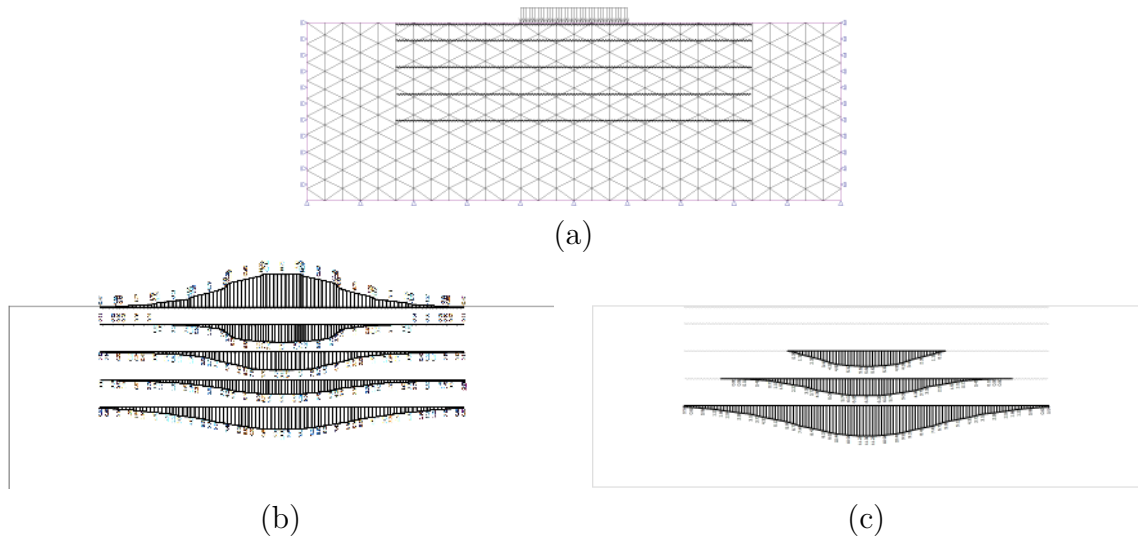


Figure 4.3: Modeling of geo-reinforcements: (a) structural setup, (b) compression allowed, (c) compression excluded

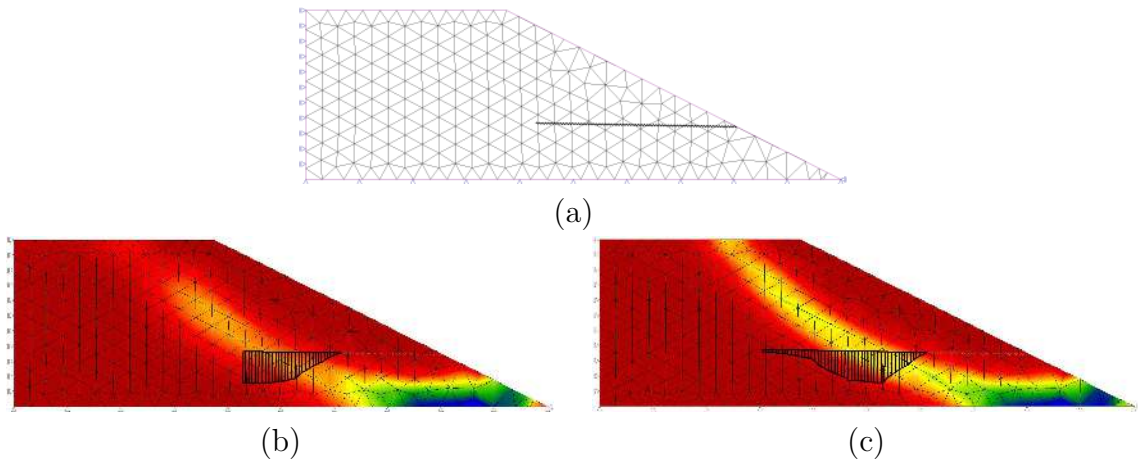


Figure 4.4: Modeling of geo-reinforcements in slope stability analysis - effect of anchorage: (a) structural setup, (b) insufficient anchorage, (c) correct anchorage

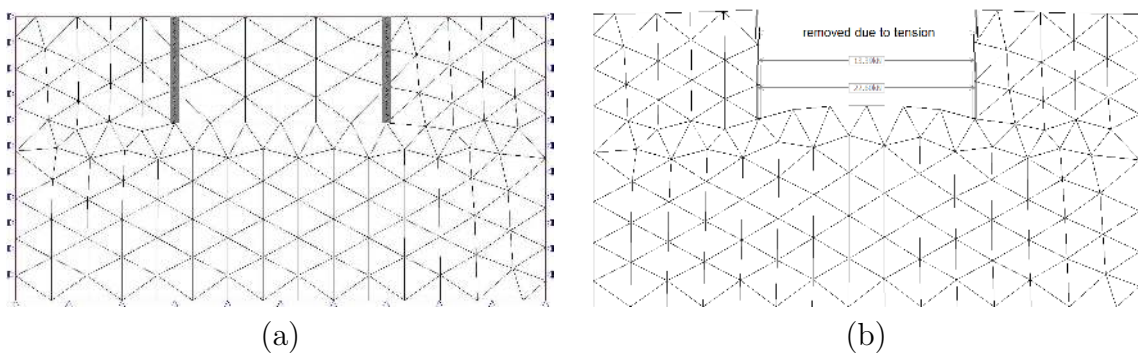


Figure 4.5: Modeling of props - only compressive forces are transmitted



# Chapter 5

## Modeling of ground water flow

So far, when addressing the ground water flow, we have limited our attention to fully drained soil behavior assuming the pore water pressure distribution is known and does not change with the deformation of the soil body. Its influence then appears directly as a contribution to the right hand side vector of the governing finite element equations already discussed in Chapter 1, recall Eqs. (1.50) and (1.69). Such steady state water flow conditions can be identified with the state of a time dependent consolidation process at a time instant approaching infinity. Another extreme soil condition assuming fully undrained soil behavior then corresponds to the onset of consolidation at a time equal to zero. Since many engineering problems can be solved adopting either of the two, or a combination of both extreme conditions, it appears useful to address the pore water contribution in more detail. In particular, it will be shown, how these two extreme soil conditions can be obtained from general consolidation equations governing the pore water flow and the deformation of the soil due to loading in a coupled manner.

Formulation of a set of fundamental equations for a saturated-unsaturated flow in a deforming porous medium with a restriction to a one-phase flow will therefore open this chapter. Their application for the solution of the two, time independent, extreme conditions will be considered next. First we present the theory for the solution of soil deformation under fully undrained conditions ( $t = 0$ ) assuming fully saturated soil and a zero flux boundary condition (no flow across the entire boundary of the analyzed domain). The second extreme soil condition assumes pore water flow through the soil skeleton being again independent of time but at  $t \rightarrow \infty$  (fully drained soil condition). The two governing equations then decouple resulting in the solution of a steady state seepage problem. This will be examined in the context of two different types of pore water flow: an unconfined flow that requires tracking the free surface separating saturated and unsaturated zones (phreatic surface), see e.g. seepage analysis of earth dams [23], or a confined flow which does not involve the phreatic surface. The chapter then continues by addressing the problem of flow through a thin layer using interface elements which allow for a direct simulation of various flow conditions including fully permeable or impermeable walls. A special treatment of so called precipitation boundary conditions is discussed next. These are essentially dual boundary conditions [29] assigned to a portion of the boundary where both a hydraulic head or a flux boundary condition might be imposed

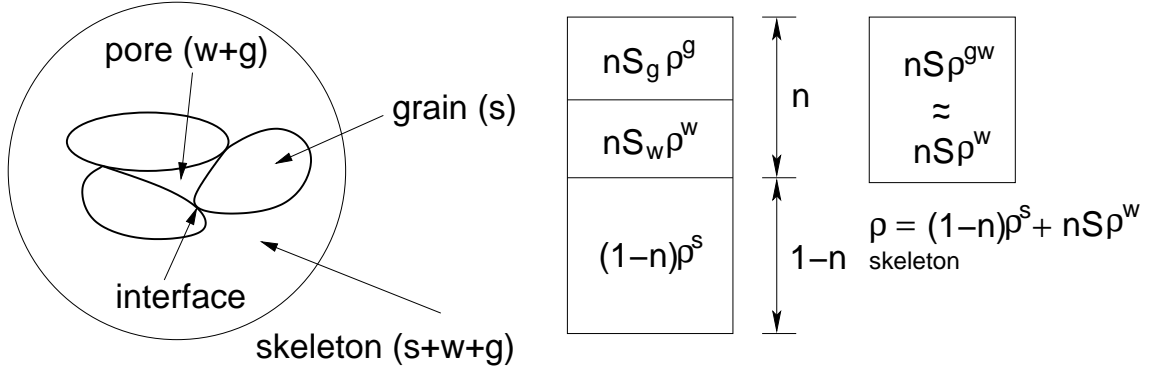


Figure 5.1: Simplified definition of a two-phase medium

depending on the hydraulic state inside and outside of the domain along this boundary. A particular interface element based on the penalty method was developed in [1] to handle these conditions. A similar yet more simple approach is developed here in Section 5.4.2. Instead of using interface elements the seepage boundary conditions are dealt with by drawing a parallel with a nonlinear spring like support. The chapter concludes by solving a one-dimensional consolidation problem, which is exploited here to extract the material parameters using the modified and generalized Cam clay models.

## 5.1 One-phase flow in a partially saturated deforming medium

Soils are often regarded as a three-phase porous medium (skeleton) consisting of grains (a solid phase  $s$ ) and pores filled with liquid water ( $w$ ) and moist air ( $g$ ) as sketched in Fig. 5.1. Suppose that a sufficiently large (representative) volume of a three-phase medium  $\Omega$  can be selected to define a volume average of the mass density  $\rho_r$  of a given phase  $r$  as

$$\rho_r = \frac{1}{\Omega} \int_{\Omega} \rho(\mathbf{x}) \chi^r d\Omega = c_r \rho^r, \quad (5.1)$$

where  $\chi^r$  is a characteristic function equal to one if the point  $\mathbf{x}$  is found in the phase  $r$  and equal to zero otherwise,  $c_r = \Omega_r/\Omega$  represents the volume fraction of a given phase and  $\rho^r$  is the intrinsic mass density written as

$$\rho_r = \frac{1}{\Omega_r} \int_{\Omega} \rho(\mathbf{x}) \chi^r d\Omega. \quad (5.2)$$

The overall mass density in a certain macroscopic point is then provided by

$$\rho = \rho_s + \rho_w + \rho_g = (1-n)\rho^s + nS_w\rho^w + nS_g\rho^g, \quad (5.3)$$

suggesting that

$$c_s = 1 - n \quad c_w = nS_w \quad c_g = nS_g, \quad S_w + S_g = 1,$$

where  $S_w$  and  $S_g$  represent the degree of saturation associated with liquid water and moist air, respectively, and  $n$  is the porosity typically written in terms of the void ratio  $e$  as

$$n = \frac{e}{1 + e}, \quad e = \frac{\Omega_w + \Omega_g}{\Omega_s}. \quad (5.4)$$

The pore pressure  $p^s$  acting on a solid phase can be then expressed as

$$p^s = S_w p^w + S_g p^g. \quad (5.5)$$

To simplify the model it will be further assumed that during the flow the moist air will remain at atmospheric pressure. Next, taking the atmospheric pressure as the reference pressure gives  $p^g = 0$  so that, see also [19],

$$p^s = S_w p^w = S p. \quad (5.6)$$

Eq. (5.3) then reduces to

$$\rho = (1 - n)\rho^s + n S \rho^w. \quad (5.7)$$

Note that  $\rho = \rho_{dry}$  or  $\rho = \rho_{sat}$  depending on whether the macroscopic point is found above or below the ground water table. Such a simplified two-phase model, which essentially treats the liquid and gaseous phases as the mixture of a one-phase compressible fluid moving throughout the porous skeleton (Fig. 5.1), will be adopted henceforth. Readers interested in a more general description of moisture and heat transfer in porous media are referred to [22, 19].

### 5.1.1 Constitutive equations

A standard volume averaging already employed in Eqs. (5.3) and (5.7) to define an effective mass density of the porous skeleton allows us to write the total stress  $\boldsymbol{\sigma}$  in terms of the stress  $\boldsymbol{\sigma}^s$  developed in the solid phase and the stress  $S p$  transmitted by the pores as

$$\boldsymbol{\sigma} = (1 - n)\boldsymbol{\sigma}^s - 3\mathbf{m}(n S p) = \underbrace{(1 - n)(\boldsymbol{\sigma}^s + 3\mathbf{m} S p)}_{\boldsymbol{\sigma}^{eff}} - 3\mathbf{m} S p, \quad (5.8)$$

which reduces to Eq. (1.48) assuming fully saturated soil consisting of rigid grains. Recall that  $\boldsymbol{\sigma}^{eff}$  then represents the effective stresses between the grains. Taking on the other hand the strains in the bulk material due to changes of the pore pressure  $S p$  into account yields Eq. (1.48) in a slightly modified format

$$\boldsymbol{\sigma}^{eff} = \mathbf{D}^{el}(\boldsymbol{\varepsilon} - \mathbf{m}\boldsymbol{\varepsilon}_v^p), \quad (5.9)$$

where  $\mathbf{D}^{el}$  is the elastic stiffness matrix of the skeleton and

$$\boldsymbol{\varepsilon}_v^p = -\frac{S p}{K_s}, \quad (5.10)$$

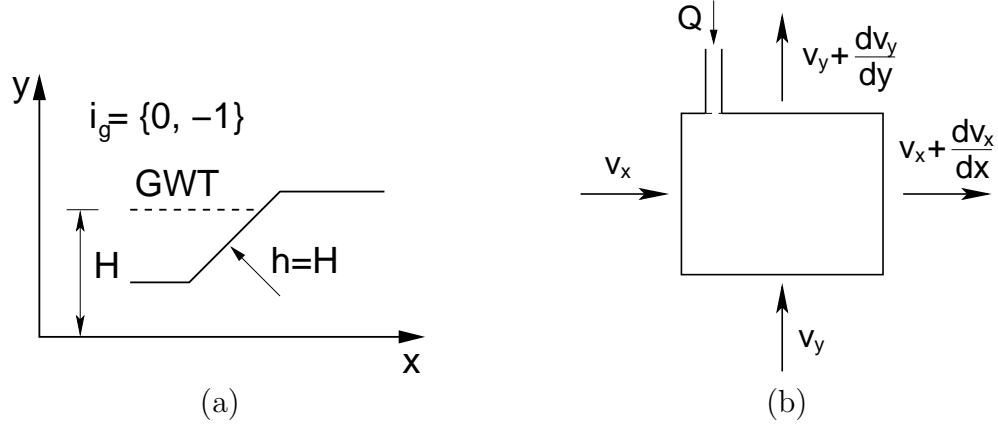


Figure 5.2: a) Coordinate system, b) Continuity conditions

represents the volumetric strain of the solid phase due to changes of the pore pressure  $Sp$  with  $K_s$  being the bulk modulus of the solid phase. Following [2, 22, 19] allows us to rewrite Eq. (5.8) as

$$\boldsymbol{\sigma} = \mathbf{D}^{el} \boldsymbol{\varepsilon} - \alpha 3\mathbf{m}Sp, \quad (5.11)$$

where the Biot constant  $\alpha$  reads

$$\alpha = \mathbf{m}^\top \left( \mathbf{I} - \frac{\mathbf{D}^{el}}{3K_s} \right) 3\mathbf{m} = 1 - \frac{K_{sk}}{K_s} < 1, \quad (5.12)$$

where  $K_{sk}$  is the bulk modulus of the porous skeleton. For a material without any pores,  $K_{sk} = K_s$ . For cohesive soils we typically have  $K_{sk} \ll K_s$  and  $\alpha = 1$ .

In view of future developments it becomes more convenient to rewrite Eq. (5.11) in the rate form

$$\dot{\boldsymbol{\sigma}} = \mathbf{D}^{ep} \dot{\boldsymbol{\varepsilon}} - \alpha 3\mathbf{m}(\dot{S}p + S\dot{p}) \quad (5.13)$$

where  $(\dot{\quad})$  stands for the derivative with respect to time and  $\mathbf{D}^{el}$  now represents the instantaneous tangent stiffness matrix of the skeleton. Combining Eqs. (5.9), (5.13) and (5.10) then renders the rate of mean effective stress to the form

$$\dot{\sigma}_m^{eff} = K_{sk} \left( \dot{\varepsilon}_v + \frac{\dot{S}p + S\dot{p}}{K_s} \right) = K_{sk} \dot{\varepsilon}_v + (1 - \alpha)(\dot{S}p + S\dot{p}). \quad (5.14)$$

### 5.1.2 Transport equation - Darcy's law

Consider a coordinate system in Fig. 5.2(a) and define the hydraulic head  $h$  as (recall that the pore pressure  $p$  is positive when in compression)

$$h = \frac{p}{\gamma_w} + y, \quad \gamma_w = \rho^w g \approx 10[\text{kNm}^{-3}]. \quad (5.15)$$

The generalized form of Darcy's law describing the flow in a porous medium then reads [29, 22, 19]

$$\begin{aligned} nS\mathbf{v}^{ws} &= -K_r \mathbf{K}_{sat} \nabla h, & \mathbf{v}^{ws} &= \mathbf{v}^w - \mathbf{v}^s, \\ nS\mathbf{v}^{ws} &= -K_r \mathbf{K}_{sat} (\nabla p - \gamma_w \mathbf{i}_g), \end{aligned} \quad (5.16)$$

where  $\mathbf{i}_g$  is the unit vector parallel to gravity, Fig. 5.2(a),  $\mathbf{v}^r$  stores the components of the velocity vector of a given phase  $r = w, s$  and  $\mathbf{K}_{sat}$  [ $\text{ms}^{-1}$ ] is the permeability matrix for  $S = 1$  (fully saturated soil). Several relationships are available in the literature to define the dimensionless relative permeability  $K_r \in \langle 0, 1 \rangle$ , for the modeling of unsaturated flow.

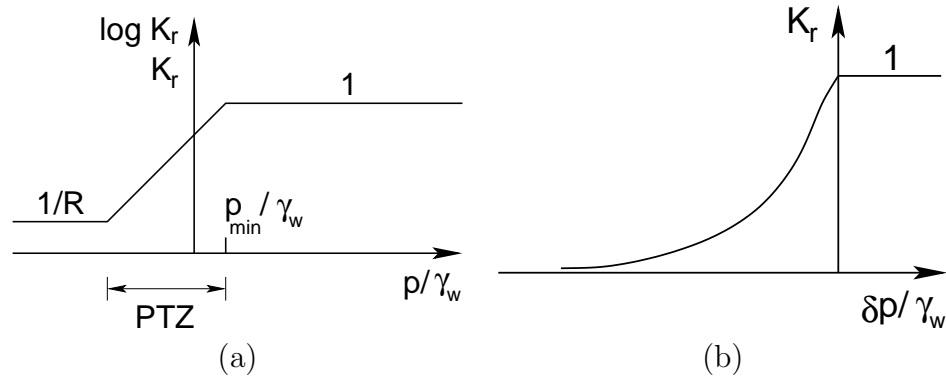


Figure 5.3: Variation of permeability with pore fluid pressure: a) [23, 29] , b) [10, 36]

A relatively simple linear variation of permeability with a pore fluid pressure in Fig. 5.3(a) was used by Li and Desai [23] to model the transition between saturated and unsaturated zones in the seepage analysis of earth dams. A more accurate relationship assuming a log-linear variation can be found, e.g. in [29]. Both models allow for reducing the permeability when the soil above the phreatic line sustains a tensile pore pressure. When the soil is assumed to be above the phreatic line the permeability is reduced by a large factor  $R \approx 100 - 1000$ . A transition zone between the fully ( $S = 1$ ) saturated ( $S = K_r = 1$ ) and fully unsaturated ( $S, K_r \rightarrow 0$ ) is then represented by the parameter PTZ. Introducing the permeability transition zone not only supports the laboratory observations but also stabilizes the required iterative algorithm typically based on the modified Newton-Raphson scheme with the permeability matrix being kept constant during iterations. Note that the log-linear variation essentially corresponds to the linearized form of the original Van Genuchten model [36] implemented, e.g. in PLAXIS [24].

The Van Genuchten model Fig. 5.3(b) suggests the variation between the relative permeability and the pore fluid pressure in the form

$$K_r = \frac{\left\{ 1 - \left( \frac{\delta p}{\gamma_w} \right)^{n-1} \left[ 1 + \left( \frac{\delta p}{\gamma_w} \right)^n \right]^{-m} \right\}^2}{\left[ 1 + \left( \frac{\delta p}{\gamma_w} \right)^n \right]^{m/2}}, \quad (5.17)$$

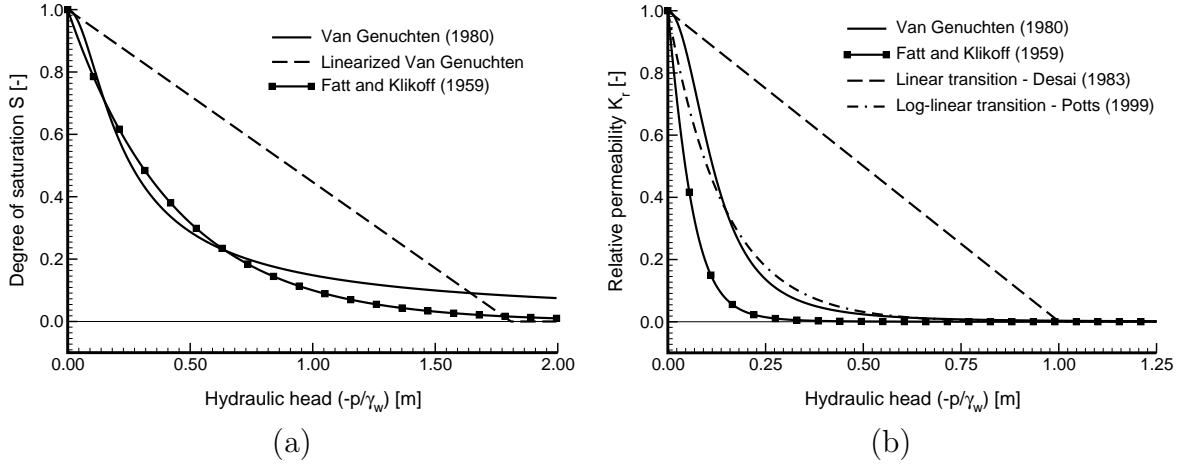


Figure 5.4: Comparison of various models: a) saturation degree, b) relative permeability

where  $\delta, n, m = 1 - 1/n$  are model parameters to be estimated from observed soil water retention data well described by the following equation

$$S = S_{irr} + \frac{(S_{sat} - S_{irr})}{\left[1 + \left(\frac{\delta p}{\gamma_w}\right)^n\right]^m}, \quad (5.18)$$

where  $S_{sat} \rightarrow 1$  and  $S_{irr}$  represents an irreducible limit of saturation, which can also be deduced from the soil water retention curve [36]. Eq. (5.18) is also implemented in the program ZSOIL [25] with default value of  $n = 2$ . Another relationship which offers the relative permeability as a function of the degree of saturation was proposed in [10] in the form

$$K_r = \frac{(S - S_{irr})^3}{(S_{sat} - S_{irr})^3}, \quad (5.19)$$

which leads with the help of Eq. (5.18) and  $S_{sat} = 1, n = 2$  to [25]

$$K_r = \frac{1}{\left[1 + \left(\frac{\delta p}{\gamma_w}\right)^2\right]^{3/2}}. \quad (5.20)$$

Individual models are compared in Fig. 5.4. While the linearized Van Genuchten model gives a relatively poor prediction of the degree of saturation as a function of the pore fluid pressure it compares well with the Van Genuchten model when evaluating the relative permeability. Both the Van Genuchten model and the log-linear transition model are implemented in the program GEO FEM.

### 5.1.3 Set of governing equations

Apart from the linear momentum balance equations (equations of equilibrium) presented in Section 1.2, Eq. (1.7), the coupled analysis of pore fluid transport throughout a de-

forming porous medium requires the introduction of the continuity equation for the liquid phase.

To do so we start from the mass balance equation for the solid

$$\frac{d[(1-n)\rho^s]}{dt} + \text{div}[(1-n)\rho^s \mathbf{v}^s] = 0, \quad (5.21)$$

where  $\mathbf{v}^s$  represents the mass average velocity of the solid phase [22]. Taking the time derivative of the first term in Eq. (5.21) gives

$$\frac{d[(1-n)\rho^s]}{dt} = \frac{\partial[(1-n)\rho^s]}{\partial t} + (\mathbf{v}^s)^\top \nabla[(1-n)\rho^s]. \quad (5.22)$$

The second term in Eq. (5.21) can be expanded as follows

$$\text{div}[(1-n)\rho^s \mathbf{v}^s] = \rho^s(1-n)\text{div}(\mathbf{v}^s) + (\mathbf{v}^s)^\top \nabla[(1-n)\rho^s]. \quad (5.23)$$

Neglecting the gradient terms in Eqs. (5.22) and (5.23) then yields

$$\frac{1-n}{\rho^s} \frac{\partial \rho^s}{\partial t} - \frac{\partial n}{\partial t} + (1-n)\text{div}(\mathbf{v}^s) = 0. \quad (5.24)$$

Similarly for the liquid phase we get

$$\frac{d(nS\rho^w)}{dt} + \text{div}[nS\rho^w \mathbf{v}^w] = Q, \quad (5.25)$$

where  $Q$  represents any sources and/or sinks (injection or pumping rate [ $\text{m}^3/\text{s}$ ] in 3D or [ $\text{m}^3/\text{s}/\text{m}$ ] in 2D plane strain), see Fig. 5.2(b). Following the same steps as applied to the solid phase then leads to

$$\frac{n}{\rho^w} \frac{\partial \rho^w}{\partial t} + \frac{\partial n}{\partial t} + \frac{n}{S} \frac{\partial S}{\partial t} + \frac{1}{S} \text{div}(nS\mathbf{v}^w) + n\text{div}(\mathbf{v}^s) = Q. \quad (5.26)$$

After combining Eqs. (5.24) and (5.26) we finally arrive at the continuity equation for the liquid phase

$$\frac{1-n}{\rho^s} \dot{\rho}^s + \frac{n}{\rho^w} \dot{\rho}^w + n \frac{\dot{S}}{S} + \frac{1}{S} \text{div}(nS\mathbf{v}^w) + \text{div}(\mathbf{v}^s) = Q. \quad (5.27)$$

To eliminate the mass density of the solid phase from Eq. (5.27) we first recall the mass conservation equation in the form [19]

$$\frac{\dot{\rho}^s}{\rho^s} = -\frac{\dot{V}^s}{V^s}, \quad (5.28)$$

and then using Eq. (5.14) express the rate of the volume change of the solid phase as

$$-\frac{\dot{V}^s}{V^s} = \frac{\dot{S}p + S\dot{p}}{K_s} - \frac{\dot{\sigma}^{eff}}{(1-n)K_s} = \frac{1}{1-n} \left[ \frac{\alpha-n}{K_s} (\dot{S}p + S\dot{p}) + (\alpha-1)\text{div}(\mathbf{v}^s) \right]. \quad (5.29)$$

Similarly, employing the mass conservation equation of the liquid phase gives

$$\frac{\dot{\rho}^w}{\rho^s} = \frac{\dot{p}}{K_w}, \quad (5.30)$$

where  $K_w$  is the bulk modulus of the pore fluid. Then after substituting Eqs. (5.29) and (5.30) together with Eq. (5.16)<sub>1</sub> (Darcy's law) back into Eq. (5.27) we finally get

$$\frac{\alpha - n}{K_s}(\dot{S}p + S\dot{p}) + \frac{n\dot{p}}{K_w} + \alpha \operatorname{div}(\mathbf{v}^s) + n\frac{\dot{S}}{S} + \frac{1}{S} \operatorname{div}(-K_r \mathbf{K}_{sat} \nabla h) = Q. \quad (5.31)$$

Assuming incompressibility of grains ( $\alpha = 1$ ) and fully saturated soil ( $S = 1$ ) renders a relatively simple form of Eq. (5.31)

$$\left( \frac{1-n}{K_s} + \frac{n}{K_w} \right) \dot{p} + \operatorname{div}(\mathbf{v}^s) + \operatorname{div}(-K_r \mathbf{K}_{sat} \nabla h) = Q. \quad (5.32)$$

Eqs. (1.7) and (5.31) or (5.32) accompanied by the relevant boundary conditions now allow for the solution of general time dependent consolidation problem. This step, however, goes beyond the scope of the present text so the interested reader is referred, e.g. to [2, 22, 29, 19].

## 5.2 Fully undrained behavior of saturated soil

To begin we first rewrite Eq. (5.32) in the incremental form (no internal sources are admitted  $Q = 0$ )

$$\left( \frac{1-n}{K_s} + \frac{n}{K_w} \right) \Delta p + \alpha 3\mathbf{m}^\top \Delta \boldsymbol{\varepsilon} + \Delta t \operatorname{div}(-K_r \mathbf{K}_{sat} \nabla h) = 0, \quad (5.33)$$

noting that

$$\dot{p} = \frac{\Delta p}{\Delta t}, \quad \operatorname{div}(\mathbf{v}^s) = 3\mathbf{m}^\top \left( \frac{\Delta \boldsymbol{\varepsilon}}{\Delta t} \right).$$

Next, suppose that an instantaneous loading under zero flux boundary conditions (no flow across the domain boundary) is prescribed, thus letting  $\Delta t \rightarrow 0$ , and solve for  $\Delta p$  from Eq. (5.33) to get

$$\Delta p = \frac{-\alpha 3\mathbf{m}^\top}{\frac{\alpha - n}{K_s} + \frac{n}{K_w}} \Delta \boldsymbol{\varepsilon}. \quad (5.34)$$

The equilibrium equation (1.7) in the context of the principle of virtual work (1.13) now becomes, recall Eq. (5.13),

$$\int_{\Omega} \delta \Delta \boldsymbol{\varepsilon}^\top (\mathbf{D}^{ep} \Delta \boldsymbol{\varepsilon} - \alpha 3\mathbf{m} \Delta p) \, d\Omega = \Delta f. \quad (5.35)$$



Substituting for  $\Delta p$  from Eq. (5.34) into Eq. (5.35) then provides

$$\int_{\Omega} \delta \Delta \boldsymbol{\epsilon}^T \left[ \mathbf{D}^{ep} + \frac{\alpha^2}{\frac{\alpha - n}{K_s} + \frac{n}{K_w}} \mathbf{I} \right] \Delta \boldsymbol{\epsilon} \, d\Omega = \Delta f, \quad (5.36)$$

where  $\mathbf{I}$  is the identity matrix. Once  $\Delta \boldsymbol{\epsilon}$  is known from the solution of Eq. (5.36) the unknown increment of pore pressure  $\Delta p$  then readily follows from Eq. (5.34).

As suggested in [29] a certain simplification of the new (effective) stiffness matrix  $\mathbf{D}_{eff}$

$$\mathbf{D}_{eff} = \mathbf{D}^{ep} + \frac{\alpha^2}{\frac{\alpha - n}{K_s} + \frac{n}{K_w}} \mathbf{I}, \quad (5.37)$$

is available. To proceed, first denote

$$K_{eff} = \frac{1}{\frac{\alpha - n}{K_s} + \frac{n}{K_w}}, \quad (5.38)$$

where  $K_{eff}$  represents an effective bulk modulus. Providing  $K_w \ll K_s$  (incompressibility of grains is adopted,  $\alpha = 1$ ) we get

$$\frac{1}{K_{eff}} = \frac{n}{K_w}.$$

Since  $K_w \gg K_{sk}$  it is possible to set  $K_{eff} = K_w$ . A sufficiently large number can then be assigned to  $K_{eff}$ , typically

$$K_{eff} = (100 - 1000)K_{sk}.$$

This simplified formulation of the effective stiffness matrix also implemented in the program GEO FEM was used to simulate an undrained triaxial test of a clayey soil. The soil behavior was assumed to be well represented by the modified and generalized Cam clay models. Both models were already discussed in detail in Chapter 3 and tested over a number of examples. All calculations were, however, performed under drained boundary conditions. The present set of numerical experiments thus serves as an additional source of information for assessing the performance of both models.

Table 5.1: Material parameters of the selected clayey soil

Model	$\nu$ [-]	$\kappa$ [-]	$\lambda$ [-]	$e_0$ [-]	$M_{cs}$ [-]	$\varphi_{cv}$ [°]	$\varphi_{in}$ [°]
Modified Cam clay	0.25	0.025	0.181	1.67	0.797	–	–
Generalized Cam clay	0.25	0.025	0.181	1.67	–	34.13	40.0

The material data used in this study is listed in Table 5.1. Fig. 5.5 shows the results derived for a normally consolidated soil loaded in the triaxial extension. Similar results

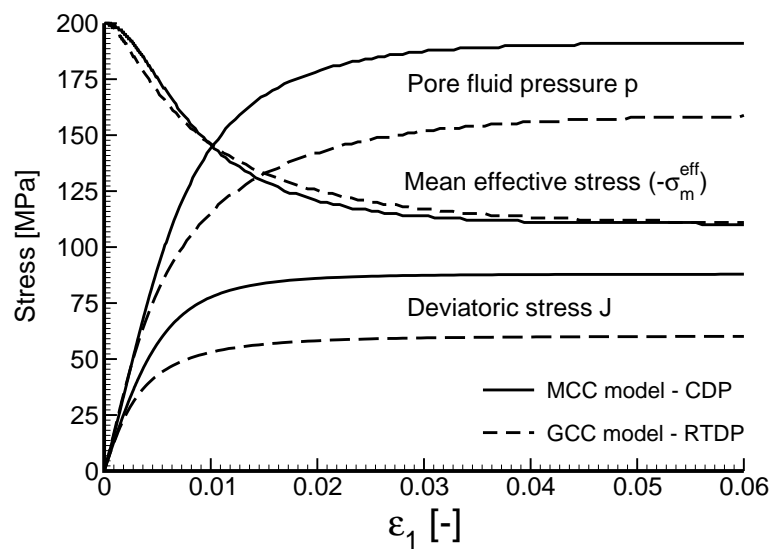
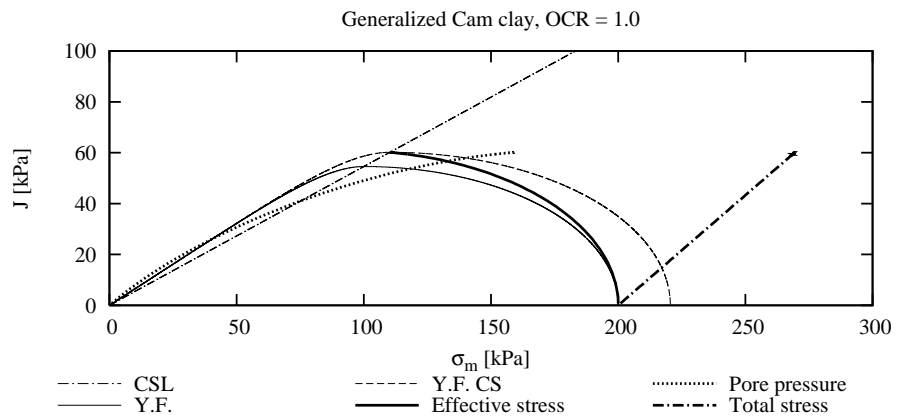
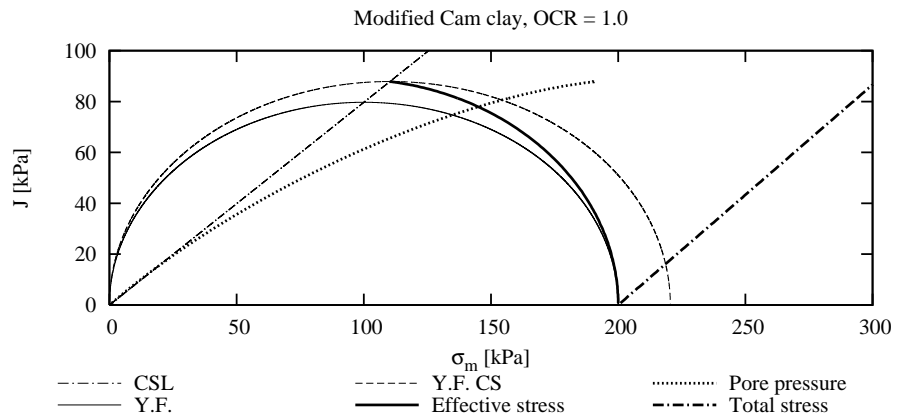
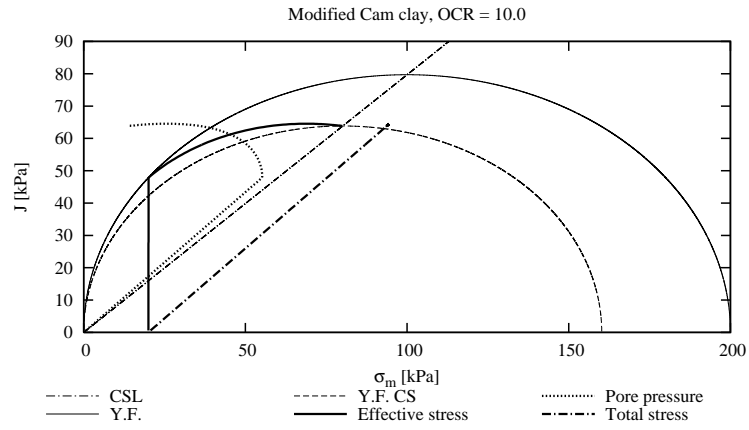
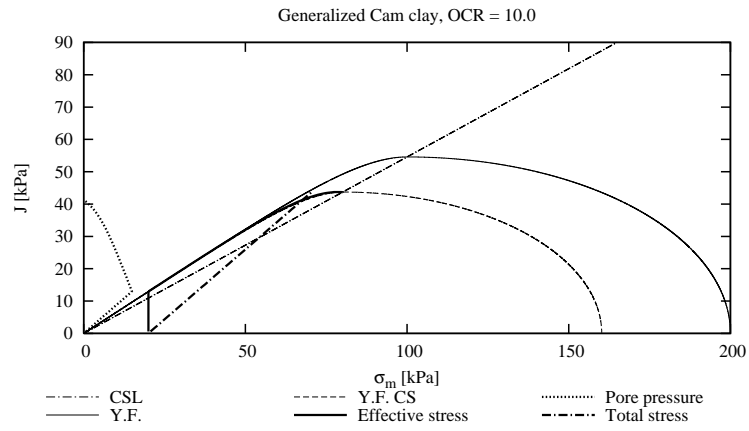


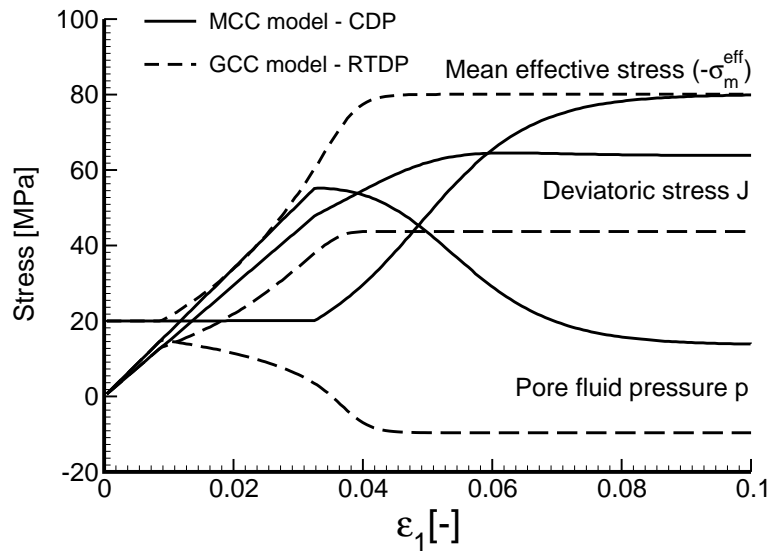
Figure 5.5: Triaxial extension test of normally consolidated soils: a) and b) evolution of yield surfaces for MCC and GCC models, c) stress distributions



(a)



(b)



(c)

Figure 5.6: Triaxial extension test of overconsolidated soils: a) and b) evolution of yield surfaces for MCC and GCC models, c) stress distributions

obtained for an overconsolidated soil are plotted in Fig. 5.6. As for the normally consolidated soil the soil sample was stressed initially by the prescribed isotropic stress  $\sigma_x = \sigma_y = \sigma_z = \sigma_m = -200$  kPa. Then the transverse (radial) stress component was increased to load the sample until failure. As evident from Figs. 5.5(a)(b) the yield function expands during shearing and the material hardens. A substantial increase of the pore pressure reduces the mean effective stress as seen in Fig. 5.6(c) and the effective stress path bends to the left resting eventually on the critical state line.

To demonstrate the effect of overconsolidation the sample was first unloaded from the original isotropic stress state  $\sigma_m = -200$  kPa to  $\sigma_m = -20$  kPa before shearing. This stress state corresponds to the overconsolidation ratio  $OCR = -\sigma_m/p_c = 10$ . When shearing, the loading path at an early stage of loading generates only elastic strains thus having negligible effect on the effective mean stress, while pore pressure increases. When the yield surface is reached, the pore pressure starts to decrease due to dilatation, which in turn increases the mean effective stress, Fig. 5.6(c). The effective stress path bends to the right until reaching again the critical state line, Figs. 5.6(a)(b). Similar behavior was observed experimentally, see [29, 5] for further details on this subject.

We finally point out a considerable difference in the predictions of the collapse load evident from the stress-strain curves in Figs. 5.5(c) and 5.6(c). This is attributed to the fact that the Lode angle dependent yield surface of the generalized Cam clay model turns on the plastic deformations at much early stages of loading since being essentially inscribed into the circular surface of the modified Cam clay model.

### 5.3 Steady state seepage

When soil deformation no longer influences the flow of pore fluid through the skeleton (no excess pore pressure is generated during loading), the flow becomes essentially time independent ( $\dot{p} = 0, \dot{S} = 0, \text{div} \mathbf{v}^s = 0$ ) and the continuity equation (5.32) reduces to

$$\text{div} (-K_r \mathbf{K}_{sat} \nabla h) = Q. \quad (5.39)$$

Solving Eq. (5.39) calls for the introduction of hydraulic boundary conditions. These are either imposed fluxes (natural boundary conditions) or prescribed changes in pore fluid pressure (essential boundary conditions). They are essentially analogous to prescribed traction and displacement boundary conditions discussed in Chapter 1, Eqs. (1.9) and (1.10). In particular, see Fig. 5.7(a), we have (the seepage boundary conditions on  $\Gamma_s$  are treated separately in Section 5.4.2)

- Imposed fluxes  $\bar{q}_n$  normal to the boundary  $\Gamma_q$  -  $\mathbf{n}$  is the outward unit normal,  $\bar{q}_n$  is assumed positive when in the direction opposite to  $\mathbf{n}$  (inflow, see Fig. 5.7)

$$\mathbf{n}^\top (n \mathbf{v}^{ws}) = -\mathbf{n}^\top (K_r \mathbf{K}_{sat} \nabla h) = -\bar{q}_n \quad \text{on } \Gamma_q, \quad (5.40)$$

- Prescribed pore pressure values  $\bar{p}$  or hydraulic heads  $\bar{h}$  on the boundary  $\Gamma_p$

$$p = \bar{p} \quad \text{or} \quad h = \bar{h} \quad \text{on } \Gamma_p, \quad (5.41)$$

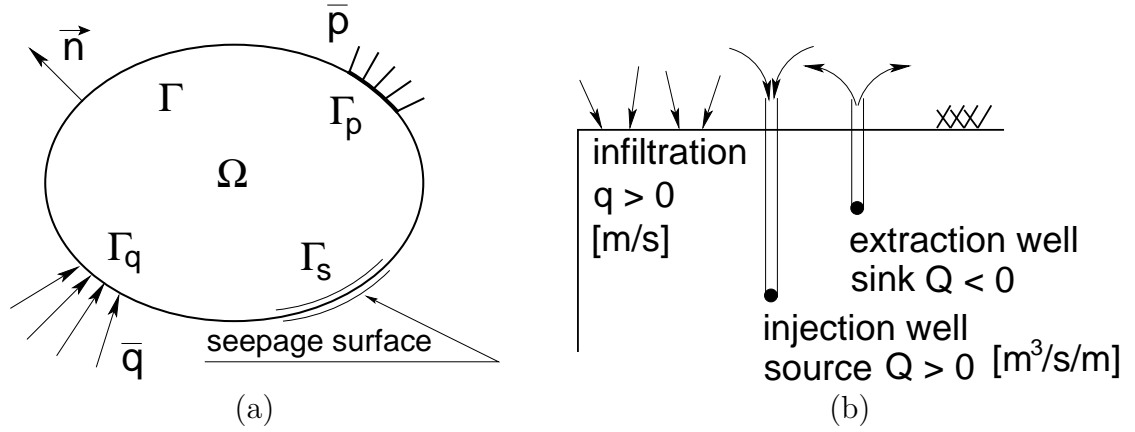


Figure 5.7: a) Hydraulic boundary conditions, b) Infiltration, sources and sinks

Note that a closed form solution of the system of equations Eqs. (5.39) - (5.41) is not generally available. A natural step is therefore to rewrite the continuity equation (5.39) in the context of the principle of virtual work. To do so, recall Eq. (1.11) and write

$$\int_{\Omega} \delta h (-\nabla^T K_r \mathbf{K}_{sat} \nabla h) d\Omega + \int_{\Gamma_q} \delta h (\mathbf{n}^T K_r \mathbf{K}_{sat} \nabla h - \bar{q}_n) d\Gamma = \sum_{i=1}^{M_Q} \delta h_i Q_i, \quad (5.42)$$

where  $M_Q$  represents the number of pointwise applied sources  $Q_i$ . Applying integration by parts and taking into account the fact that  $\delta h = 0$  on  $\Gamma_p$  gives

$$\int_{\Omega} (\nabla h)^T K_r \mathbf{K}_{sat} \nabla h d\Omega = \int_{\Gamma_q} \delta h \bar{q}_n d\Gamma + \sum_{i=1}^{M_Q} \delta h_i Q_i. \quad (5.43)$$

This equation can be now easily solved using the finite element method. In such a case the distribution of the hydraulic head can be approximated using standard element shape functions from Section 1.3.3 as

$$h = \sum_{i=1}^n N_i r_i, \quad (5.44)$$

where  $r_i$  represent the nodal hydraulic heads. The finite element equations derived by substituting for  $h$  from Eq. (5.44) into Eq. (5.43) now become

$$\mathbf{H} \mathbf{r} = \mathbf{f}_h, \quad (5.45)$$

where  $\mathbf{r}$  stands for the vector of nodal hydraulic heads and

$$\mathbf{H} = \int_{\Omega} \mathbf{B}^T K_r \mathbf{K}_{sat} \mathbf{B} (= \nabla \mathbf{N}) d\Omega, \quad (5.46)$$

$$\mathbf{f}_h = \int_{\Gamma_p} \mathbf{N}^T \mathbf{N} \bar{q}_n d\Gamma + \sum_{i=1}^{M_Q} \delta h_i Q_i, \quad (5.47)$$

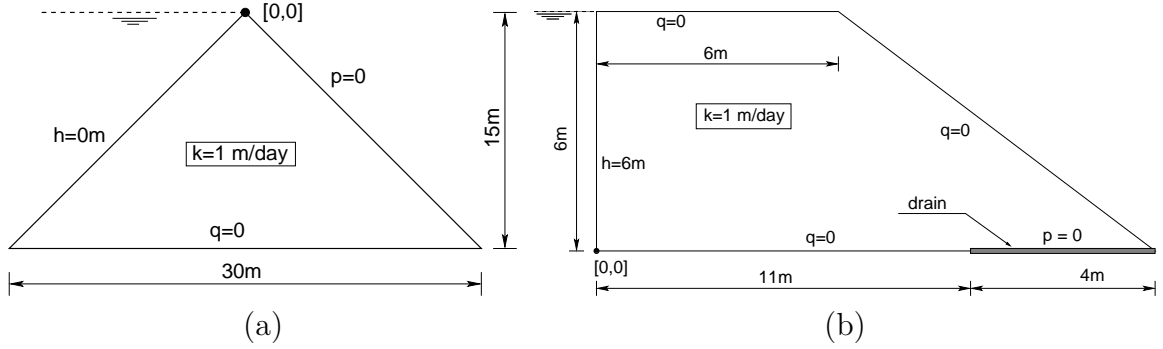


Figure 5.8: Examples: a) confined flow, b) unconfined flow

where  $Q_i$  are the nodal values of prescribed sources and/or sinks, which may correspond to injection or pumping rates representing for example the effect of injection or extraction wells as shown schematically in Fig. 5.7(b). Similarly, prescribing  $\bar{q}_n$  allows for simulating pore fluid flows across a boundary of the finite element mesh, e.g. infiltration rate Fig. 5.7(b). In the simplest case, in which no fluid is transferred across the boundary  $\Gamma_q$  the imposed flux  $\bar{q}_n = 0$ . In comparison with the solution of pure deformation of a soil body these boundary conditions correspond to prescribed surface tractions. Finally, prescribed values of the incremental nodal hydraulic heads Eq. (5.41) can be dealt with in the same fashion as when prescribing the nodal displacements.

When the permeability matrix  $K_r \mathbf{K}_{sat}$  is constant and the flow is confined (the phreatic line is known), the solution of Eq. (5.45) reduces to a single inversion of the matrix  $\mathbf{H}$ . If, on the other hand, the flow is unconfined (the phreatic line unknown), an iterative scheme must be employed to solve Eq. (5.45). Typically, the modified Newton-Raphson scheme or rather the initial stress method is employed. The solution then proceeds as follows. Define a vector of unbalanced forces at the beginning of the  $i^{th}$  iteration

$$\Delta \mathbf{f}_i = \mathbf{f}_h - \mathbf{R}_i, \quad (5.48)$$

where

$$\mathbf{R}_i = \mathbf{H} \mathbf{r}_i, \quad \mathbf{r}_i = \mathbf{r}_{i-1} + \Delta \mathbf{r}, \quad \Delta \mathbf{r} = \mathbf{H}_{sat}^{-1} \Delta \mathbf{f}_{i-1}, \quad (5.49)$$

$$\mathbf{H}_{sat} = \int_{\Omega} \mathbf{B}^T \mathbf{K}_{sat} \mathbf{B} d\Omega. \quad (5.50)$$

Therefore, at each iteration the increments of hydraulic heads are calculated for a given increment of the unbalanced forces found from Eq. (5.48) and added to the total heads. This procedure is repeated until a certain convergence criterion is reached. Further details can be found in [15].

A typical example of a confined flow is a triangular dam with the water level reaching the crest of the dam. The geometry and relevant boundary conditions appear in Fig. 5.8(a). The corresponding nodal values of the hydraulic head follows directly from Eq. (5.49)<sub>3</sub>. No iterations are needed in this particular case since the permeability matrix is assumed constant and the analysis does not involve the phreatic line.

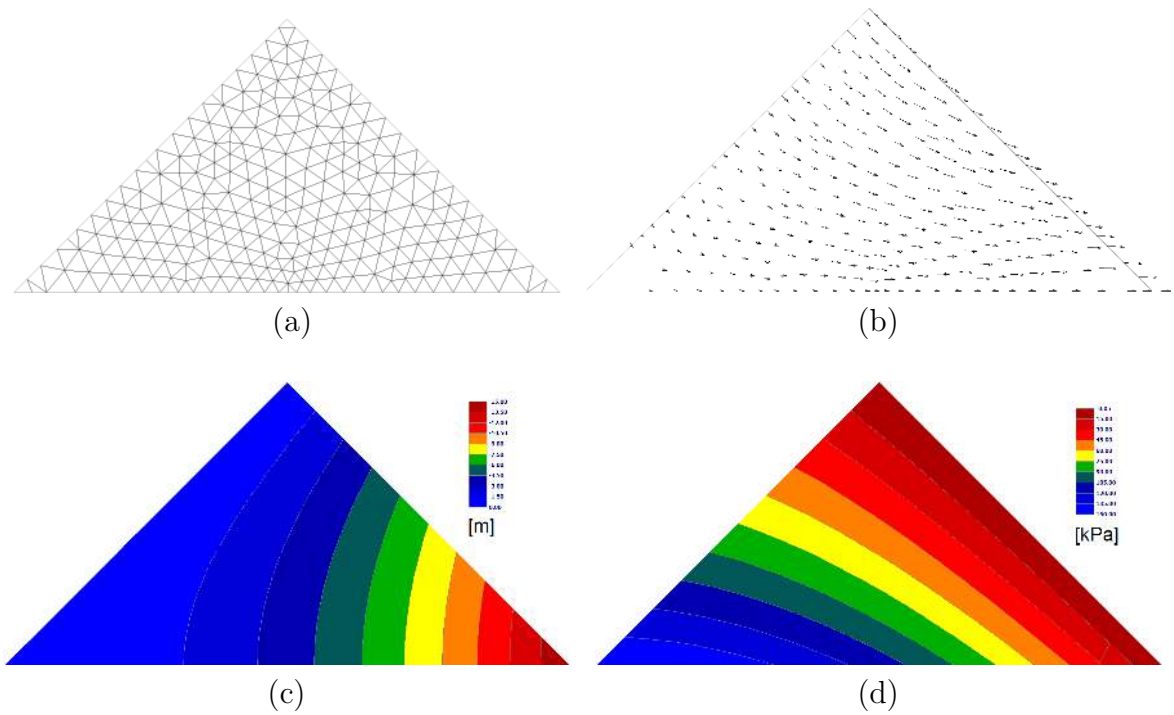


Figure 5.9: Example of a confined flow - triangular dam: a) FE mesh, b) distribution of flux, c) distribution of hydraulic head, d) distribution of pore pressure

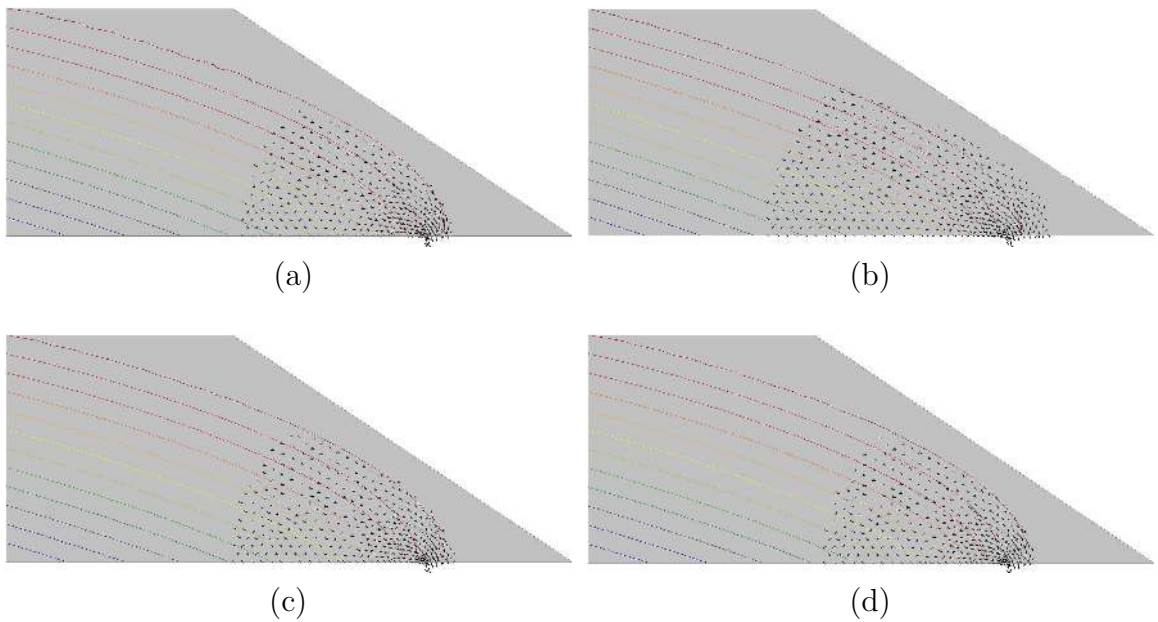


Figure 5.10: Example of unconfined flow - influence of transition law: a) Linear law with PTZ=0.5m and  $p_{min} = 0$ , b) Linear law with PTZ=1m and  $p_{min} = 0$ , c) Log-linear law with PTZ=1m and  $p_{min} = 0$ , d) Van Genuchten model with  $S_{irr} = 0$ ,  $S_{sat} = 1$ ,  $n = 2$ ,  $\delta = 0.15\text{m}^{-1}$

On the contrary, Fig. 5.8(b) illustrates a typical example of unconfined flow which clearly requires free-surface (phreatic line) tracking since its location is not known a priori. Owing to the prescribed boundary conditions (assumed drain at the bottom of the dam) there is no seepage surface to be considered along the downstream boundary. Also, no drawdown is expected along the boundary on the left hand side of the dam. While still relatively simple, the solution of this problem can only be handled with the iterative scheme represented by Eqs. (5.48) and (5.49). The results are plotted in Fig. 5.10. Contours of the pore fluid pressure distribution including the zero-pressure line (phreatic line) were found from Eq. (5.18) using the parameter setting for the Van Genuchten model (see caption in Fig. 5.10). All three pore pressure transition zone models discussed previously in Section 5.1.2 were considered. It is evident that all models can deliver the same results providing the model parameters are suitably chosen. Nevertheless, the Van Genuchten model for the evaluation of  $K_r$  is set as default in GEO FEM since it is directly related to Eq. (5.18) and its parameters, as already mentioned, can be estimated with relative simplicity from soil water retention data [36].

No convergence difficulties were encountered in this particular example for any of the three models. However, replacing the assumed homogeneous body with a layered soil having considerable differences in permeabilities between various layers may lead to ill conditioning of the flow matrix  $\mathbf{H}$  in Eq. (5.45) causing numerical instabilities and consequently the loss of convergence of the system of equations (5.49). Care therefore must be taken when expecting too large differences, typically exceeding  $10^5$ , between the highest and lowest permeability value.

## 5.4 Flow through a thin zone - modeling of interfaces

In many real situations we often need to deal with flow across or along an interface of two layers having marginally different permeabilities. Although two nodes, one for each layer, are generated by default along the common boundary a fully permeable boundary condition is assumed by tying the corresponding hydraulic head degrees of freedom of the adjacent nodes. Treating impermeable or partially permeable boundaries requires on the other hand the introduction of interface elements into the finite element model. Interface elements can also be used to either block the flow across an impermeable sheeting wall or to represent a drain by easing flow along the longitudinal direction of the interface. Special attention is required when seepage interface elements are used when the seepage surface (a part of the finite element mesh boundary where the applicable hydraulic conditions are not known a priori) is encountered. Formulation and implementation of both types of interface element will be now discussed in greater detail.

### 5.4.1 Thin zone interface element

Fig. 5.11 shows three particular conditions which may occur when simulating flow through a thin interfacial zone. Example A represents a fully impermeable boundary. This is the most simple case when interface elements do not essentially contribute to the governing



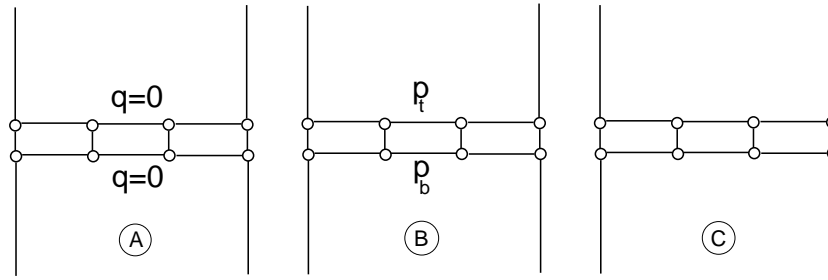


Figure 5.11: Hydraulic boundary conditions on interface

system of equations which in turn results into a discontinuous pore pressure field. To enforce pore pressure continuity ( $p_t = p_b$ ) in the case of a fully permeable boundary, example B, it is sufficient to tie the corresponding hydraulic head (pore pressure) degrees of freedom along the interface without actually formulating interface elements to account for flow. The intermediate boundary conditions (example C), which may include both the above two extremes, must however be handled by interface elements.

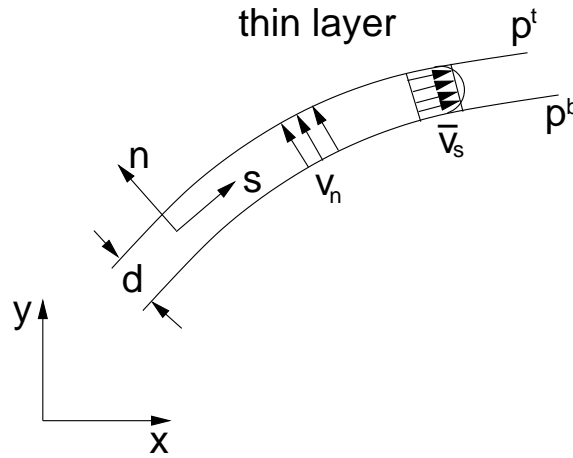


Figure 5.12: Flow through a thin zone

Fig. 5.12 shows a simplified representation of flow both in the longitudinal ( $s$ ) and normal ( $n$ ) direction of a thin interfacial zone with  $s, n$  representing the local coordinate system. Since interface elements have zero thickness we get (for the local coordinate system)

$$h = \frac{p}{\gamma_w}. \quad (5.51)$$

Darcy's law then assumes the following form

$$n\mathbf{v}^{ws} = -\mathbf{K}_{sat} \nabla h = -\frac{\mathbf{K}_{sat}}{\gamma_w} \nabla p, \quad (5.52)$$

and the continuity condition (5.32) reduces to

$$\frac{n}{K_w} \dot{p} + \mathbf{m}^\top \operatorname{div}(\mathbf{v}^s) + \operatorname{div}(-\mathbf{K}_{sat} \nabla h) = 0. \quad (5.53)$$

In 2D the vector  $\mathbf{m}$  now has the components  $(0, 1)$  and the permeability matrix reads

$$\mathbf{K}_{sat} = \begin{bmatrix} k_s & 0 \\ 0 & k_n \end{bmatrix}, \quad (5.54)$$

where  $k_s, k_n$  are the permeabilities in the longitudinal and normal direction, respectively. The corresponding fluxes are given by, see Fig. 5.12,

$$q_s = -k_s \frac{1}{2} \frac{\partial(h^t + h^b)}{\partial s}, \quad (5.55)$$

$$q_n = -k_n \frac{h^t - h^b}{d}, \quad (5.56)$$

where  $d$  is a virtual thickness of the interface. Similarly we define the velocity components of the solid phase so that

$$\operatorname{div}(\mathbf{v}^s) = v_s^s + v_n^s = \frac{1}{2} \frac{\partial((\dot{u}_s^s)^t + (\dot{u}_s^s)^b)}{\partial s} + \frac{(\dot{u}_n^s)^t - (\dot{u}_n^s)^b}{d}. \quad (5.57)$$

Providing we are interested only in steady state conditions Eq. (5.53) considerably simplifies (note the similarity with Eq. (5.39))

$$\operatorname{div}(-\mathbf{K}_{sat} \nabla h) = 0. \quad (5.58)$$

A weak form of Eq. (5.58) leads again, after finite element discretization, to Eq. (5.45) where the  $\mathbf{B}$  matrix in Eq. (5.46) is now provided by

- 4-node interface element

$$\mathbf{B} = \begin{bmatrix} \frac{1}{2J} \frac{\partial N_1}{\partial \xi} & \frac{1}{2J} \frac{\partial N_2}{\partial \xi} & \frac{1}{2J} \frac{\partial N_1}{\partial \xi} & \frac{1}{2J} \frac{\partial N_2}{\partial \xi} \\ -\frac{N_1}{d} & -\frac{N_2}{d} & \frac{N_1}{d} & \frac{N_2}{d} \end{bmatrix}, \quad (5.59)$$

- 6-node interface element

$$\mathbf{B} = \begin{bmatrix} \frac{1}{2J} \frac{\partial N_1}{\partial \xi} & \frac{1}{2J} \frac{\partial N_2}{\partial \xi} & \frac{1}{2J} \frac{\partial N_3}{\partial \xi} & \frac{1}{2J} \frac{\partial N_1}{\partial \xi} & \frac{1}{2J} \frac{\partial N_2}{\partial \xi} & \frac{1}{2J} \frac{\partial N_3}{\partial \xi} \\ -\frac{N_1}{d} & -\frac{N_2}{d} & -\frac{N_3}{d} & \frac{N_1}{d} & \frac{N_2}{d} & \frac{N_3}{d} \end{bmatrix}, \quad (5.60)$$

where  $N_i$  are the element shape functions for either 2-node or 3-node rod element discussed already in Section 1.3.4, Table 1.7, and  $J = L/2$  is the Jacobian with  $L$  being the element length.

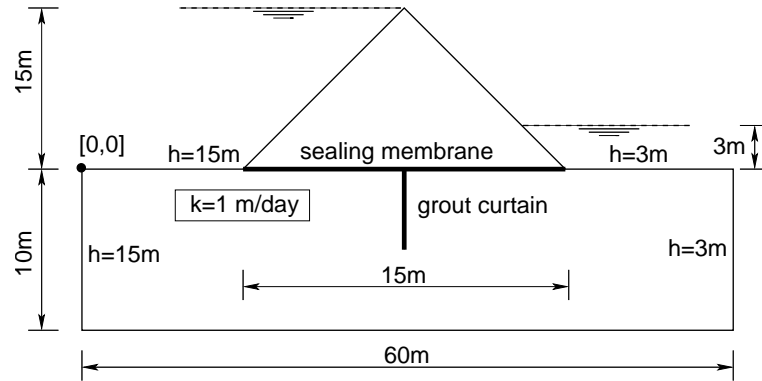


Figure 5.13: Modeling of confined interfacial flow: geometry and boundary conditions

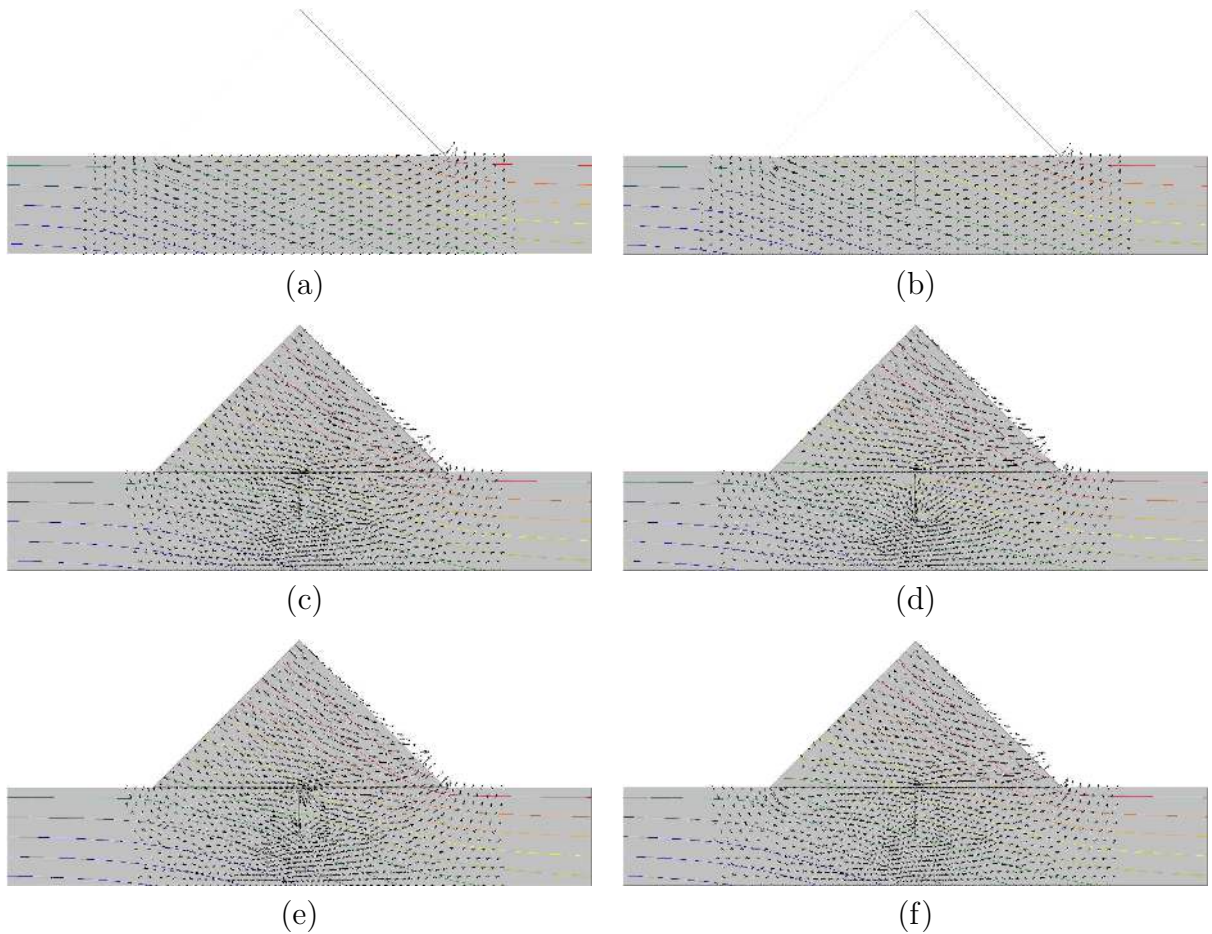


Figure 5.14: Modeling of interfacial flow - results: a) impermeable dam, permeable curtain, no interface elements, b) impermeable dam, permeable curtain - interface elements, c) membrane and curtain fully permeable, d) drain and impermeable curtain, e) permeable membrane and impermeable curtain, f) drain and permeable curtain

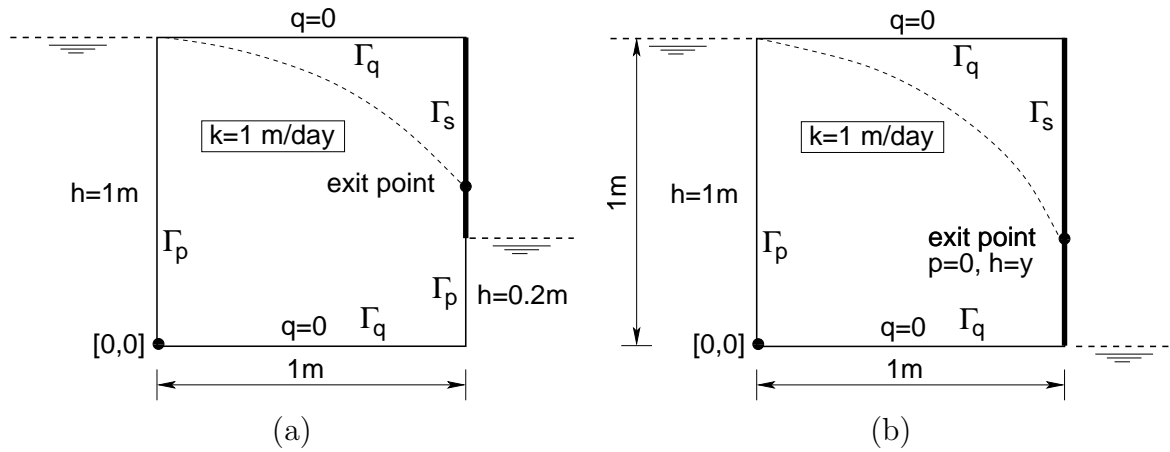


Figure 5.15: Example of unconfined flow: modeling of flow through a seepage surface: a)  $h=0.2\text{m}$ , b)  $h=0$

An example illustrating the use of interface elements is shown in Fig. 5.13. For simplicity a confined flow through a triangular dam was considered again. A sealing membrane at the bottom of the dam and an impervious curtain were introduced to simulate drain and flow around an impermeable wall. Both a membrane and a grout curtain are modeled by interface elements. Their contribution to the finite element equations then depends on the values assigned to interfacial permeabilities  $k_s, k_n$ .

When no restriction to flow through interface elements is assumed then these are either excluded from the finite element mesh or their permeabilities are assigned very high values (1000 times the permeability of the soil was used in this example) resulting, in both cases, in a continuous pore pressure distribution. This option is examined in Figs. 5.14(a)(b) considering the dam to represent a fully impermeable concrete block. The part of the boundary on the bottom of the dam is then assigned a zero flux boundary condition  $\bar{q}_n = 0$  by default. When on the other hand the interface elements are used to block the flow (impermeable wall) then the values of both  $k_s$  and  $k_n$  are set to zero producing a discontinuous distribution of pore pressures. This is evident from Figs. 5.14(d)-(f). Compare then with Fig. 5.14(c) where no restrictions to flow were imposed. Intermediate conditions can also be specified to simulate specific drain conditions by allowing for fluid to flow freely in the longitudinal direction while blocking the flow in the perpendicular direction. Such conditions were assigned to a sealing membrane by setting  $k_s = 1000 \times$  the soil permeability and  $k_n = 0$ . The corresponding results are plotted in Figs. 5.14(d)(e). Notice again the discontinuity in the pore pressure isolines.

### 5.4.2 Seepage surface

To introduce the subject consider two examples of a rectangular dam in Fig. 5.15. It is a relatively complex problem as it involves both a phreatic surface separating saturated and unsaturated zones inside the dam and a seepage surface on the right hand side of the dam where the characteristic hydraulic conditions are not known a priori. While  $\bar{q}_n = 0$

is a correct boundary condition above the point where the phreatic surface touches the seepage surface ( $S < 0, h < 0$  inside the domain), below this point along the seepage surface the pore fluid pressure becomes zero (it should rather be in equilibrium with the atmospheric pressure, but that is taken as a reference pressure) since water is free to flow across the boundary ( $S = 1, h = y$ ). This problem was studied, e.g. in [15] by changing the boundary conditions during an iterative solution (either prescribed flux or prescribed hydraulic heads) whenever necessary owing to the fact that the exit point is not known in advance.

Switching from one type of boundary condition to the other may cause substantial difficulty in coding the finite element program. While the flux boundary condition Eq. (5.40) is automatically satisfied by the weak formulation the imposed hydraulic head boundary condition, Eq. (5.41) reduces the number of active degrees of freedom. An elegant way to deal with these seepage boundary conditions was suggested in [1] by formulating special seepage interface elements in the framework of the penalty method. The main advantage of these elements is the possibility of distinguishing between internal and external hydraulic conditions. When introduced along a boundary inside the domain it further allows us to simulate a constant pore pressure jump across the interface. A similar approach was adopted in [35] when solving the coupled heat and moisture transport in masonry structures.

The use of these special interface elements can be avoided providing the Newton-Cotes integration scheme is assumed. The seepage boundary conditions apply directly to the boundary nodes and can be introduced through a nonlinear spring model by defining a flux through the surface in the form

$$\bar{q}_n = k_v(h - h_{ext}), \quad (5.61)$$

where  $k_v$  is a fictitious permeability (a spring constant) that must be sufficiently large to ensure that  $h = h_{ext}$  at the boundary nodes where a nonzero external pressure is prescribed. Imposing external pressures through Eq. (5.61) appears useful when the location of zero external pressure changes with time, which may occur not only on the downstream face of the dam but also on the upstream face during filling or drawdown. Since only steady state flow is considered herein the external pressure does not change with time and can be imposed directly on the respective degrees of freedom. The seepage surface then becomes adequate only for that part of the boundary where  $p_{ext} = 0$  (flow at atmospheric pressure). The seepage boundary conditions on  $\Gamma_s$  can then be written as

$$\bar{q}_n = k_v(h - y), \quad \text{if } h > 0 \text{ (} S = 1 \text{) in the domain and } p_{ext} = 0, \quad (5.62)$$

$$\bar{q}_n = 0, \quad \text{if } h < 0 \text{ (} S < 1 \text{) in the domain and } p_{ext} = 0, \quad (5.63)$$

where the zero flux boundary condition Eq. (5.63) is generated by setting  $k_v = 0$ . Note that this is exactly the same approach as used with tension excluded spring supports in purely mechanical analyses. Incorporating Eq. (5.62) into the finite element analysis requires the weak form, Eq. (5.43), to be modified as

$$F_{int} + \sum_{i=1}^{M_s} \delta h_i k_v h_i |_{\Gamma_s} = F_{ext} + \sum_{i=1}^{M_s} \delta h_i k_v y_i |_{\Gamma_s}, \quad (5.64)$$

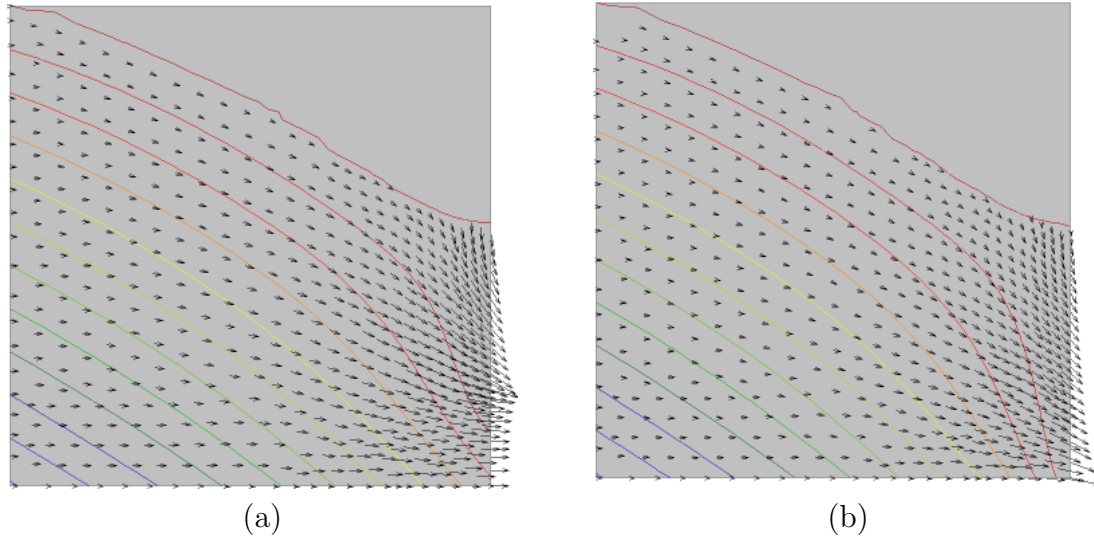


Figure 5.16: Modeling of seepage surface (Van Genuchten model with  $S_{irr} = 0, S_{sat} = 1, n = 2, \delta = 0.01\text{m}^{-1}$ ): a)  $h=0.2\text{m}$ , b)  $h=0$

where  $M_s$  is the number of nodes on the seepage surface and  $y_i$  is the respective  $y$ -coordinate of the node.

This particular approach was employed to solve the two problems in Fig 5.15. Note that for boundaries well above the phreatic line where no seepage is expected (the top boundary in Fig. 5.15 or the downstream boundary in Fig. 5.8(b)) it may be more appropriate to directly prescribe the no flow conditions  $\bar{q}_n = 0$  rather than let this condition be generated through the seepage surface Eq. (5.63). The results are plotted in Fig. 5.16. The variation of nodal fluxes clearly show the difference between the two example problems. It is worth noting that the solution is not as much dependent on the penalty stiffness  $k_v$  as it is on the parameters of the Van Genuchten model. While the algorithm succeeded in finding the exit point on the seepage surface, it failed to provide a sufficiently accurate distribution of pore pressure profile in the vicinity of that point.

# Bibliography

- [1] D. Aubry and O. Ozanam, *Free-surface tracking through non-saturated models*, International Conference on Numerical Methods in Geomechanics, Innsbruck (Swoboda, ed.), Balkema, Rotterdam, 1988, pp. 757–763.
- [2] Z. Bittnar and Šejnoha J., *Numerical methods in structural engineering*, ASCE Press, 1996.
- [3] R. I. Borja, *Cam-clay plasticity, part ii, implicit integration of constitutive equations based on a nonlinear elastic stress predictor*, Computer Methods in Applied Mechanics and Engineering **88** (1991), 225–240.
- [4] R. I. Borja, S. R. Lee, and R. B. Seed, *Numerical simulation of excavation in elasto-plastic soils*, International journal for numerical methods in geomechanics **13** (1989), 231–249.
- [5] T. M. M. Connolly, *The geological and geotechnical properties of a glacial lacustrine clayey silt*, Ph.D. thesis, Imperial College, University of London, 1999.
- [6] R. A. Day and D. M. Potts, *Curved mindlin beam and axi-symmetric shell elements - a new approach*, International Journal for Numerical Methods in Engineering **30** (1990), 1263–1274.
- [7] ———, *Zero thickness interface elements - numerical stability and applications*, International journal for numerical and analytical methods in geomechanics **18** (1994), 689–708.
- [8] J. M. Dłuzewski, *Nonlinear consolidation in finite element modeling*, IX International conference on computer methods and advances in geomechanics (China Wuhan, ed.), 1997, pp. 1089–1094.
- [9] H. A. M. van Eekelen, *Isotropic yield surfaces in three dimensions for use in soil mechanics*, Int. Jnl. Num. Anal. Mech. Geomech. **4** (1980), 89–101.
- [10] I. Fatt and W.A. Klikoff, *Effect of fractional wettability on multiphase flow through porous media*, AIME Trans. **216** (1959), 246, Note No. 2043.
- [11] A. E. Groen, *Three-dimensional elasto-plastic analysis of soils*, Ph.D. thesis, Technical University Delft, 1997.

- [12] M. Hija, J. Fortin, and G. de Saxce, *A complete stress update algorithm for the non-associated drucker-prager model including treatment of apex*, International Journal of Engineering Science **41** (2004), 1109–1143.
- [13] J. M. Hohberg, *A note on spurious oscillations in fem joint elements*, Earthq. Engineering Struc. Dynamic. **18** (1990), 0.
- [14] M. J. Hvorslev, *On the physical properties of disturbed cohesive soils*, Ingeniorvidenskabelige Skrifter. A (1958), no. 45, 159.
- [15] Bakker. K. J., *Analysis of groundwater flow through revetments*, 3rd International Symposium on Numerical Methods in Geomechanics, Niagara Falls, Canada, 1989, pp. 367–734.
- [16] T. Janda, P. Kuklík, and M. Šejnoha, *Mixed experimental numerical approach to evaluation of material parameters of clayey soils*, International Journal of Geomechanics **4** (2004), no. 3, 199–206.
- [17] M. Jirásek and Z.P. Bažant, *Inelastic analysis of structures*, John Wiley & Sons, Ltd., Baffins Lane, Chichester, England, 2002.
- [18] M. K. Kim and P. V. Lade, *Single hardening constitutive model for frictional materials i. plastic potential function*, Computers and Geotechnics **5** (1988), 307–324.
- [19] T. Krejčí, T. Nový, L. Sehnoutek, and J. Šejnoha, *Structure - subsoil interaction in view of transport processes in porous media*, CTU Reports, vol. 5, CTU in Prague, 2001, 81 pp.
- [20] P. V. Lade, *Elasto-plastic stress-strain theory for cohesionless soils with curved yield surfaces*, International Journal for Solids and Structures **13** (1977), 1019–1035.
- [21] P. V. Lade and M. K. Kim, *Single hardening constitutive model for frictional materials ii. yield criterion and plastic work contours*, Computers and Geotechnics **6** (1988), 13–29.
- [22] R. W. Lewis and B. A. Schrefler, *The finite element method in the static and dynamic deformation and consolidation of porous media*, John Wiley&Sons, Chichester, England, 2nd edition, 1999.
- [23] G. C. Li and C. S. Desai, *Stress and seepage analysis of earth dams*, Journal of Geotechnical Engineering **109** (1983), no. 7, 946–960.
- [24] PLAXIS Ltd., *Plaxis 07 - user manual*, <http://www.fine.cz>, 2005.
- [25] ZSOIL Ltd., *Zsoil - theoretical manual*, <http://www.fine.cz>, 2005.
- [26] H. Matsuoka and T. Nakai, *Stress-deformation and strength characteristics of soil under three different principal stresses*, Proc. Jap. Soc. Civ. Eng., 1968, pp. 59–70.



- [27] J. Pamin, *Gradient-dependent plasticity in numerical simulation of localization phenomena*, Ph.D. thesis, Technical University Delft, 1994.
- [28] Pankaj and N. Bičanič, *Detection of multiple active yield conditions for mohr-coulomb elasto-plasticity*, *Computers and Structures* **62** (1997), 51–61.
- [29] D. M. Potts and L. Zdravković, *Finite element analysis in geotechnical engineering – theory*, Thomas Telford, London, 1999.
- [30] ———, *Finite element analysis in geotechnical engineering – application*, Thomas Telford, London, 2001.
- [31] K. H. Roscoe and J. B. Burland, *On the generalised behaviour of 'wet' clay*, *Engineering plasticity* (J. Heyman and F. A. Lechie, eds.), Cambridge University Press, 1968, pp. 535–609.
- [32] K. H. Roscoe, A. N. Schofield, and C. P. Worth, *On the yielding of soils*, *Geotechnique* **8** (1958), 22–55.
- [33] J. C. Simo and R. L. Taylor, *Consistent tangent stiffness operators for rate-independent elastoplasticity*, *Computer Method in Applied Mechanics and Engineering* **48** (1985), 101–118.
- [34] D. K. H. Smith, I. M. Abd Ho, *Influence of construction technique on the performance of a braced excavation in marine clay*, *International journal for numerical methods in geomechanics* **16** (1992), 845–867.
- [35] J. Sýkora, J. Vorel, J. Šejnoha, and J. Šejnoha, *Analysis of coupled heat and moisture transfer in masonry structures*, *Materials and Structures* **0** (2007), 0–0, Submitted.
- [36] M. Th. Van Genuchten, *A closed equation for predicting the hydraulic conductivity of unsaturated soils*, *Journal Soil Science Society of America* **44** (1980), 892–898.
- [37] J. Červenka, *Discrete crack modeling in concrete structures*, Ph.D. thesis, University of Colorado, Boulder, 1994.
- [38] M. Šejnoha and K. Matouš, *Nonlinear analysis of initially prestressed laminates*, *Contributions to Computational Mechanics in Civil Engineering* (Z. Bittnar, ed.), vol. 3, CTU Reports, no. 4, CTU in Prague, 1999, pp. 55–68.
- [39] W.T.Koiter, *Stress-strain relations, uniqueness and variational theorems for elasto-plastic materials with a singular yield surface*, *Q. appl. Math* **11** (1953), 350–354.